DEPARTAMENTO DE ASTROFISICA

Universidad de La Laguna

MILLIMETRIC GROUND-BASED OBSERVATIONS OF CMB ANISOTROPY

Memoria que presenta
D. Bruno Femenía Castellá
para optar al grado de
Doctor en Astrofísica.

INSTITUTO Ð ASTROFISICA Ð CANARIAS
Febrero de 1998

A mi tía E.S.C.
que vela por mi allá donde las estrellas están

Agradecimientos

En primer lugar quiero agradecer al IAC y a su director D. Francisco Sánchez, como su más alto representante, por haberme dado la oportunidad de realizar esta tesis. En este sentido quiero expresar mi agradecimiento a mi director de tesis D. Rafael Rebolo López.

Quiero también agradecer a todas aquellas personas que a lo largo de esta tesis me han brindado su amistad. Mis compañeros de despacho, tanto a los *de siempre* como a las nuevas adquisiciones, con quienes he compartido innumerables carcajadas y bromas, haciendo más llevaderas los momentos en los que las cosas parecen resistirse a salir. A las personas con las que he colaborado; a los de aquí: Carlos con quien las discusiones literario-ético-políticas hicieron más agradables los momentos de análisis de los datos, Rafael por su supervisión, a Bob, Julio y Roger por su eterna disponibilidad a ayudar en lo que haga falta; y a los de allá: Michele, ricordati che troppe..., Lucio el perfecto anfitrión y cocinero, Giuseppe maestro en el arte de la paciencia y próximo papá (un beso para Paola), Shafinaz con quien compartí casa en Madison. Quiero agradecer la enorme hospitalidad con que P. T. Timbie me acogió tanto en su casa como en su grupo allá en Madison así como a todos los miembros de su grupo que me aceptaron como uno más: Joshua, Sean, Brian, Chris, Slade y Karen.

A mis amigos de fuera del IAC; Víctor que me acogió y me dio el calor de su familia cuando llegué por primera vez a Tenerife, haciendo más llevadero el inmenso dolor que supuso estar lejos de casa, de Valencia. A Carlos Flores, con quien uno puede siempre contar para todo excepto para ir a navegar. A Jose *el argentino*, quien ya hace años que no veo pero de quien me resulta imposible olvidarme por la cantidad de kilómetros que me hizo correr. A Esteban con quien he compartido tantos y tantos momentos desde el primer día en que pisé esta maravillosa isla. A Rubén, mi compañero de piso en Herradores. A todos con quienes compartí residencia en La Cordera...

A Santi, Dani y Joaquinet, cuya amistad perdura en el tiempo y en la distancia. Sé que siempre podré contar con ellos.

Las penúltimas líneas van destinadas a aquéllos cuya presencia llevo siempre en el corazón, mis padres, mi hermana y mi abuelo. Siempre ahí, apoyando y luchando conmigo, sufriendo cuando yo lo hacía y alegres al verme sonreir. Pese a todos mis enfados por teléfono, no os quepa duda que os quiero y que sé que todo lo haceís por amor.

Y para finalizar, mi agradecimiento por el amor de Laura. Su amor es la luz que nos guía a ambos en el camino de la vida. Hemos superado muchímos problemas juntos y tenemos toda una vida por delante. Tu amor y tu presencia son lo más valioso que esta tesis me han reportado y sólo ellos ya justifican todos estos años de lucha sin cuartel.

Resumen

En este trabajo se presenta un experimento fruto de la colaboración entre el Intituto de Astrofísica de Canarias y el Bartol Research Institute destinado a la medida de anisotropía en el Fondo Cósmico de Microondas y que realizó dos campañas de observación desde el Observatorio del Teide en los años 1994 y 1996. En esta tesis se discute la toma y análisis de los datos correspondientes a la campaña de observación realizada entre Junio y Agosto de 1994 y en la que se tomaron unas 550 horas de datos.

La región de cielo observada estuvo centrada en declinación 40° fijando el telescopio al suelo en azimut y elevación y dejando que el cielo cruzase el haz instrumental al rotar la Tierra. Mediante una demodulación de los datos originales es posible extraer los dos primeros armónicos de la señal correspondientes a observaciones en las bandas multipolares $\ell = 33^{+24}_{-13}$ y $\ell = 53^{+22}_{-15}$ del espectro angular de fluctuaciones del Fondo Cósmico de Microondas (FCM).

El instrumento, con un temaño de haz de FWHM$\simeq 2.1^\circ$ y un ángulo de chopeo $\beta \simeq 2.9^\circ$, realizó medidas en cuatro bandas milimétricas centradas a las longitudes de onda en 3.3, 2.1, 1.3 y 1.1 mm. Durante esta tesis se ha desarrollado una técnica de reducción del ruido atmosférico cuya aplicación a los datos ha permitido la eliminación de gran parte del ruido atmosférico en noches individuales de observación. En esta tesis se presentan los resultados de varios tests para determinar la eficiencia de dicha técnica, concluyéndose que usando como monitor atmosférico el canal a más alta frecuencia es posible eliminar gran parte del ruido atmosférico en los otros tres canales.

La región final analizada estadísticamente depende del canal y demodulacion considerada, siendo la mayor para el canal 1 en la banda a $\ell = 53$ y que comprende la zonas de cielo entre $[206^\circ, 285^\circ]$ y $[331^\circ, 381^\circ]$ en ascensión recta, mientras que la menor zona de cielo corresponde al canal 2 en la banda $\ell = 33$ que comprende la zona $[331^\circ, 361^\circ]$ en ascensión recta. Las estimaciones de los distintos contaminantes Galácticos predicen señales debidas a éstos muy por debajo del rudio atmosférico e incluso de la señal que se espera del FCM. Los resultados de los datos en la banda $\ell = 33$ son poco concluyentes y existen serias dudas de que todavía estén dominados por la presencia de residuos atmosféricos en el barrido final. El análisis de los datos en estas regiones en la banda $\ell = 53$ revela la existencia de una señal con una amplitud $\sqrt{\bar{\ell}(\bar{\ell}+1)C_{\bar{\ell}}/(2\pi)} = 55^{+27}_{-22}\,\mu K$ consistente con otros resultados experimentales a escalas angulares comparables con la nuestra y con lo que se espera de los modelos teóricos de materia fría oscura. A pesar de la barra de error

asociada, este resultado indica una subida del espectro angular de fluctuaciones del FCM, tal y como cabe esperar si en efecto existe el llamado pico Doppler y cuya existencia parece ser indicada por resultados experimentales de otros grupos trabajando a mayor resolución angular.

Summary

In this work it is presented an experiment for the study of Cosmic Microwave Background (CMB) anisotropy resulting from the collaboration between the Intituto de Astrofísica de Canarias and the Bartol Research Institute. This experiment operated in a series of two campaigns at the Observatorio del Teide in 1994 and 1996. In this thesis only the results from the first campaign are presented, corresponding to measurements taken from June until August 1994 with a total amount of data of about 550 hours.

The region of observations concentrated at declination 40° by fixing the telescope in azimuth and elevation relative to the ground and letting the sky drift through the instrumental beam as the Earth rotates. By means of a demodulation of the raw data it is possible two extract the two first harmonics of the data corresponding to the multipole bands $\ell = 33^{+24}_{-13}$ and $\ell = 53^{+22}_{-15}$ in the CMB angular spectrum.

The instrument is charaterized by a beam of FWHM$\simeq 2.1^\circ$ and a chopping angle $\beta \simeq 2.9^\circ$. Measurements were performed at four millimetric bands centred at wavelengths at 3.3, 2.1, 1.3 and 1.1 mm. The development of an atmospheric reduction technique and its application to our data allowed to subtract most of the atmospheric noise on individual nights of observations. Several tests on the performance of this new technique are presented showing that by using the highest frequency channel as an atmospheric monitor, the atmospheric noise can be greatly reduced in the other three remaining channels.

The final region of sky contemplated for the statistical analysis depends on the channel and demodulation and it varies. Thus, the biggest fraction of sky was observed by channel 1 in the band at $\ell = 53$ observing in the RA ranges $[206^\circ, 285^\circ]$ and $[331^\circ, 381^\circ]$, while the smallest fraction of the sky was that observed by channel 2 at the band $\ell = 33$ corresponding to the RA range $[331^\circ, 361^\circ]$ in RA. The estimates of the likely signal due to Galactic foregrounds indicate that they should be much smaller that the atmospheric noise and even that ths expected CMB signal.The results from the data in the band at $\ell = 33$ are are not very conclusive as it seems to still being dominated by atmospheric residuals. However,the statistical analysis in these regions of the sky in the band at $\ell = 53$ reveals the presence of a signal with the expected amplitude $\sqrt{\bar{\ell}(\bar{\ell}+1)C_{\bar{\ell}}/(2\pi)} = 55^{+27}_{-22}\,\mu K$ for CMB anisotropy which is consistent with other measurements at similar angular scales and with the standard cold dark matter model. Despite the large error bar on this result, it indicates that the CMB angular power spectrum steepens, possibly due to the presence of the Doppler peak at

larger values of ℓ as already indicated by other measurements at larger angular resolution.

Contents

List of Tables

List of Figures

Chapter 1

Introduction

One of the most relevant predictions of the Standard Model in Cosmology is the presence of a radiation field filling the whole Universe and which is a remnant of a very hot phase of the Universe.

The effect of the Universe expansion on the evolution of radiation was first studied by Tolman in the 30s. In the 40's Gamow used Tolman's results to first propose an explanation for the synthesis of light elements in the primitive Universe. One of the most relevant consequences of Gamow's pioneering works was the prediction of the existence of a radiation background[1] with an initially estimated temperature of $T_{CMB} \sim 10K$. In posterior works and in collaboration with Alpher and Herman, the CMB temperature was reestimated to $T_{CMB} \sim 5K$. These prediction were somehow forgotten until 1965 when in an attempt to map the Galactic radio emission with an antenna of 6 m, Arno A. Penzias and Robert W. Wilson measured an extremely isotropic field with an equivalent antenna temperature of $T \sim 3K$. Immediately, such a signal was identified by the group at Princeton University, formed by Dicke, Peebles, Roll and Wilkinson, as the CMB predicted by Gamow, Alpher and Herman. This group at Princeton leaded by Dicke was already in a program to design and build a radiometer with the purpose to measure the CMB. In this way, the CMB became one of the most important empirical cornerstones on which the Big Bang model finds support[2]. Since this early measurement, a wealth of experiments have been designed in order to measure the most important parameters of the CMB, namely, its average temperature, deviations from isotropy and polarization:

- Experiments intended to determine T_{CMB} and the CMB spectrum are a direct test to the predictions on the existence of a radiation field with a well defined Planckian spectrum and produced in very early stages of the Universe where much higher densities of energy and radiation than those observed nowadays. Further, it is possible to show from basic principles

---

[1] From now on we will refer to this radiation field as Cosmic Microwave Background and with its acronym CMB

[2] The other two cornerstones are the abundances of light elements and Hubble's law for the expansion of the Universe

that if thermal equilibrium was ever reached, the Planckian character of the radiation is cit is well established that a Planckian field preserves the blackbody spectrum while its temperature evolves according to $T_{CMB} \propto (1+z)$, where z is the redshift. Therefore, studying T_{CMB} versus z allows us to check out the expansion of the Universe. The motivations for studies on the CMB spectrum lie on the fact that deviations from a Planckian spectrum are closely related to possible mechanisms of dissipation energy during the early Universe.

- Studies on the anisotropy of the CMB at very different angular scales will eventually yield what is known as the angular power spectrum of the CMB (see below). From here, it is possible to draw estimations on the most important cosmological parameters. In addition, this kind of analysis can be very effective in discriminating against competing cosmological scenarios and models.

- Studies in CMB polarization also aim to obtain estimates of the same cosmological parameters obtained from studies of angular anisotropies, probably helping in breaking degeneration among these parameters that arise if only CMB anisotropy is employed in the estimates. In addition, finding polarization in the CMB would be an indicator of inhomogeneities in the matter distribution and/or of an anisotropic expansion of the Universe if linear polarization is measured.

It is also interesting to point out that the final goal of the two last points should be the determination of cosmological parameters defining cosmological scenarios and models which, in turn, attempt to explain and understand the formation of structures in the Universe.

A first attempt to build up a cosmological theory starts from the fact that at very large angular scales the Universe is rather homogeneous and isotropic. When keeping attached to such an assumption we are unable to give an answer to the problem of structure formation. This question can be solved by using a more refined theory where we consider an inhomogeneous an anisotropic Universe characterized with a metric g_{ij} and stress-energy-momentum tensor T_{ij} with dependences both on time and spatial position. It is possible to think of two ways to solve the Einstein equations:

i) Use more realistic cosmological models with $T_{ij} = T_{ij}(\vec{x}, t)$ and $g_{ij} = g_{ij}(\vec{x}, t)$ verifying $< g_{ij}(\vec{x}, t) >= \tilde{g}_{ij}(t)$ and $< T_{ij}(\vec{x}, t) >= \tilde{T}_{ij}(t)$, where quantities with tilde represent the quantities in a Friedman-Robertson-Walker Universe, and $<>$ denotes average over large volumes.

ii) Assume that at early enough stages of the Universe, the deviations from a FRW Universe were so mall that it is a good approximation to linearize Einstein's equations.

The first option results currently inaccessible given to the non-linearity of Einstein's equations and our lack of knowledge to obtain inhomogeneous solutions (in addition to our lack of knowledge of $T_{ij}(\vec{x}, t)$). The second option is probably the most popular one and allows to obtain linear equations which can be solved[3]. These linear solutions indicate that while fluctuations are very small, they grow in time and become comparable within a finite time with the observed deviations

---

[3] In fact, limits are being pushed further and some nonlinear terms start being introduced

in the Universe. In summary, the evolution of perturbations are studied in the framework of a linear theory in which very small fluctuations grow and form denser regions. These denser regions decouple from the general expansion of the Universe due to gravity thus giving rise to the big structures we currently observe in the Universe. The initial small inhomogeneities had two crucial effects:

- They may have induced anisotropies on any radiation field present at that time.
- They produced deviations from Hubble's law in the velocities at which galaxies separate from each other thus giving rise to a pattern of peculiar velocities.

Now, there is a fundamental difference in the study of these two phenomena. CMB anisotropies were imprinted in a time when the use of linear theory is completely justified to study at large scale of the universe. On the other hand, galaxies may have formed in much later stages, when linear theories are a poor description and nonlinear effects had a considerable weight.

Finally, it should be noticed that at angular scales larger than the horizon size at the time of decoupling we are observing phenomena whose explanation. falls within the domain of inflationary scenarios. In this line, probably the study of CMB anisotropies and polarization are the only means we have to test inflation.

1.1 Introduction to CMB Theory

The standard Big Bang model explains the presence of the Cosmic Microwave Background as the radiation field left after the recombination period when radiation and matter decoupled. Once this decoupling occurred, light was able to freely propagate and reach us at present[4]. The decoupling process took place when the radiation field was cool enough. This cooling was caused by the Universe expansion and it allowed protons and electrons to "re"combine[5] and form neutral atoms causing a drop of several orders of magnitude in the Thomson scattering which so far had caused the Universe to be opaque. The recombination process was gradual, taking some time with a width in redshift $\Delta z \simeq 80$ centred at $z_m \sim 1100$ ([61]). These values of Δz and z_m are rather insensitive to cosmological parameters like density of the Universe(Ω_0), fraction to the total density due to bayonic matter (Ω_B) and the Hubble constant (H_0), so they can be considered independent of the cosmological model used ([145]).

In the study of of CMB anisotropy at different angular scales it is very convenient to distinguish between different angular scales. Two angular scales are of primordial relevance in the study

---

[4] Accordingly, any observer in the Universe at any position would observe the CMB as light coming from a surface. This surface is known as Last Scattering Surface: LSS.

[5] The name of recombination is an unfortunate and misleading term for this process: it was actually the very first time in the history of the Universe when protrons ,electrons and He nuclei combined to form neutral atoms. Because its use is so common in the literature, we will also use the term recombination.

of angular distribution of CMB anisotropy. The first one is the width of the Last Scattering Surface (LSS): $\theta_d \simeq 3.8'\Omega_0^{1/2}$. The second one is the angular size of the horizon at decoupling time: $\theta_H \sim 2^\circ\Omega_0^{1/2}$. Any anisotropy structure corresponding to an angular scale smaller than θ_d is inevitably erased by the incoherent reionization process occurred during the recombination period. On the other hand, angular scales larger than θ_H are insensitive to reionization processes in the recombination period for any physical mechanism can act on scales larger than the horizon size. The intermediate case corresponding to angular scales in between θ_d and θ_H may have been erased and replaced by new anisotropy generated in later stages. This is of particular concern if after the recombination process there were new fluctuations caused by structure formation at great scales or a late reionization (see below). In view of all of this, it is convenient to distinguish between two kinds of CMB anisotropy. This distinction is motivated according to the time of its generation:

- **Primary Anisotropy:** generated prior or during the recombination process and emerging form the LSS.
- **Secondary Anisotropy:** caused by processes either linear or nonlinear after the recombination process.

In this classification we have not included the dipolar anisotropy due to our peculiar movement with respect to the inertial frame where the CMB is isotropic (except for those primary anisotropies) and homogeneous.

1.1.1 Dipolar Anisotropy

As discussed above, this source of anisotropy is caused by our peculiar movement with respect to the LSS. Then, the Doppler effect causes a dipolar pattern in the radiation we observe. Let θ be the angle between the direction of observation, $\vec{n}$ be the movement direction with a velocity v_0, and T_0 the CMB temperature as observed by an observer at rest with respect to the LSS. The temperature we would observe is given by:

$$T(\theta) = T_0 \frac{(1 - v_0/c\cos\theta)}{1-(v_0/c)^2} \;\approx\; T_0\,(1 - v_0/c\cos\theta) \qquad , v_0 \ll c \tag{1}$$

The measurement of $T(\theta)$ is able to provide us with the direction of movement together with its magnitude. Correcting from Sun's movement in the Galaxy, and Galaxy's movement within the Local Group, the observation of the dipolar anisotropy provides us with the velocity of the Local Group with respect to the LSS: $\vec{v_G}$. Several interpretations are given to this peculiar velocity. To start with, it is almost impossible it was due to random movements during the galaxy formation[6].

---

[6] To see this consider that galaxies were formed at high redshifts. Then taking into account that peculiar velocities decrease with redshift according to $v_G \propto (1+z)^{-1}$ and that today $v_G \sim 620$ Km s^{-1}, we would obtain $v_G > c$ at decoupling time $z = 1000$!

Thus, it is believed that v_G is due to gravitational acceleration caused by a relatively large and close "lump" of matter as a local super cluster of galaxies such as the cluster of Virgo. Assuming spherical symmetry for such cluster of matter and neglecting nonlinear gravitational effects we obtain that this v_G is closely related to the average density ($\overline{\rho}$) of the accumulation of matter and its distance r to it [97]:

$$v_G = \frac{1}{3}\overline{\rho}\,\Omega_0^{0.6}\,H_0\,r$$

The most accurate value of dipolar anisotropy is that reported in [40] who report an amplitude for the dipole anisotropy of $\Delta T_D = 3.372 \pm 0.014$ mK in the direction $(l,b) = (264.14^\circ \pm 0.30^\circ, 48.26^\circ \pm 0.30^\circ)$.

1.1.2 Primary Anisotropy

As already indicated, any anisotropy structure on the LSS with an angular scale smaller than θ_d will have been erased due to the superposition of similar and incoherent contributions of a wealth of layers in the plasma during the recombination process. At angular scales larger than θ_d, the anisotropy in the LSS can be written as [113]:

$$\frac{\Delta T(\vec{n})}{T} \equiv \frac{T(\vec{n}) - \overline{T}}{\overline{T}} = \frac{1}{3}\phi_d - \vec{n}\vec{v_d} + \frac{1}{4}\delta_{\gamma d} \qquad (2)$$

where:

- $\vec{n}$ is the direction of observation.
- $\overline{T}$ is the CMB average temperature .
- the index d refers to quantities evaluated at the decoupling time.

and the different contributions to $\Delta T/T$ are:

1. $1/3\ \phi_d$, corresponding to the anisotropy produced by fluctuations in the gravitational potential on the LSS. This is the so-called **Sachs-Wolfe effect**.
2. $-\vec{n}\vec{v_d}$ is due to the Doppler effect caused by peculiar movements of the matter distribution at the time of decoupling.
3. $1/4\ \delta_{\gamma d}$ is the intrinsic anisotropy of the radiation field present at decoupling time. Here the symbol δ_γ refers to the contrast in the photon density.

The contributions numbered with (1) and (2) result from the effect of light propagating in a Universe with a metric given by:

$$ds^2 = dt^2 - a(t)^2 \left[\delta_{ij} - h_{ij}(t,\vec{x})\right] dx^i\, dx^j$$

where $a(t)$ is the scaling factor and h_{ij} represent fluctuations to the Friedmann-Robertson-Walker metric. The values for $h_{ij}(t,\vec{x})$ are completely specified once we know the distribution of matter in the Universe or, equivalently, its density contrast $\delta(\vec{x},t)$ [94]. In addition, $\delta(\vec{x},t)$ defines a gravitational potential on the LSS which is the responsible for both the Sachs-Wolfe effect and peculiar velocities $\vec{v_d}$ [19]:

$$2\Delta\phi_d \;=\; 3H_0^2(1+z_d)\delta_d, \qquad 3\vec{v_d} \;=\; -2H_0^{-1}(1+z_d)^{-0.5}\delta_d$$

These are the expressions to be used in the case of having an unperturbed metric which corresponds to a flat Universe ($\Omega = 1$). The generalization to open Universes ($\Omega < 1$) is discussed among others in [3, 144, 139, 1]. The main difference with respect to the case $\Omega = 1$ concerns fluctuations in the gravitational potential describing the Sachs-Wolfe effect which now need to be integrated along the geodesic followed by the photons.

The term (3) in equation 2 is due to density fluctuations in the radiation field on the LSS. These fluctuations in the radiation field are closely related to variations in the matter density such that:

$$3\delta_\gamma \;=\; 4\delta_b \;=\; 4\delta_X, \qquad \frac{\Delta T}{T} = \frac{1}{4}\frac{\delta\rho_\gamma}{\rho_\gamma} \;\equiv\; \frac{1}{4}\delta_\gamma$$

where δ_γ, δ_b, δ_X are the density contrasts for radiation, baryonic matter and dark matter respectively. In the linear regime any fluctuation can be decomposed as the sum of two independent modes [145, 36]: adiabatic and isocurvature modes.

Adiabatic fluctuations are perturbations in the energy density such that the specific entropy for each species ($\sigma_i = n_\gamma/n_i$, n_γ is the number density of photons and n_i the equivalent for species i) is constant. In such a case we obtain $\Delta T/T \;\approx\; 1/3\delta_d$, where here the index d refers to the dominant species.

The isocurvature modes correspond to fluctuations in the number density of each kind of particles such that the energy is conserved point by point. Depending on the species where we have isocurvature fluctuations we would write:

- $\Delta T/T \;\approx\; -[\rho_b(4\rho_\gamma)^{-1}\delta_b]$, if in the baryonic component.

- $\Delta T/T \approx -[\rho_X(3\rho_b+4\rho_\gamma)^{-1}\delta_X]$, if these fluctuations show up in the non-baryonic component and the dominant species is denoted by X.

According to the inflationary scenario, only adiabatic fluctuations are expected, although isocurvature modes could have occurred in the case that more than a scalar field is present during inflation.

Each of the contributions in equation (2) dominates at a different angular scale. The Sachs-Wolfe effect is the responsible for large angular scale anisotropy (scales of several degrees with $\theta > \theta_H$). The contributions (2) and (3) are relevant at angular scales in the range delimited by θ_d and θ_H and it depends on the cosmological scenario which dominates over the other.

Finally it should be mentioned another source of anisotropy: a stochastic background of gravitational waves. Certain models predict the existence of such background which would be relevant at very large angular scales. If present, they would imprint fluctuations on the CMB at basically the same angular scales at which the Sachs-Wolfe dominates [145, 117]. Assigning to the Sachs-Wolfe effect all the anisotropy observed at large angular scales would result in an overestimation of such effect affecting the normalization of cosmological models. In principle, both effects could be distinguish from each other thanks to their different behaviors at smaller angular scales.

1.1.3 Secondary Anisotropy

The Rees-Sciama effect are fluctuations on the CMB caused by non-linear and time-dependent fluctuations of the gravitational potential. These fluctuations on the CMB would be imprinted at redshifts $1 \leq z \leq 3$ and are relevant during the late stages of galaxy formation. Then, the gravitational potential is time-dependent and the proper way to act is to consider the integrated effect on the geodesics of the photons crossing those regions of galaxy formation [81]:

$$\frac{\Delta T}{T} = 2\int_e^o \frac{\partial\phi}{\partial\tau}(\tau, \vec{x}(\tau))\, d\tau$$

where:

- o and e refer to the observing and emitting times respectively.
- ϕ is the gravitational potential which now contains explicit dependence on time. This dependence on time is due to non-linear density perturbations.
- $\vec{x}(\tau)$ is the geodesic followed by the photons in their trajectory from the LSS till the observer.

The effects due to the Ress-Sciama effect caused by structures such as the Bootes void [66] or the Great Attractor [80] have been evaluated using the above expression. These estimates depend to a high degree on the model used to represent these structures [81], so that the levels of expected fluctuations are in the range $\Delta T/T \sim 10^{-7}$–10^{-6} as caused by voids and $\Delta T/T \sim 10^{-6} - 10^{-5}$ for Galaxy concentrations. In addition, these anisotropies would not be affected by a possible reionization (see below) of the universe due to the low redshift at which they occur [82].

Another source of secondary anisotropy is the Sunyaev-Zel'dovich effect [131, 132] caused by inverse Compton scattering of photons crossing a medium with large quantities of very hot gas. Typically, these anisotropies are expected to occur in galaxy clusters where the intergalactic gas is extremely hot ($T_e \sim 10^8 K$) and dense ($N_e \sim 10^{-2}$–$10^{-3}\ cm^{-3}$). The study of this effect requires solving the Kompaneets equation which describes the spectral distortions due both to the inverse Compton scattering and free-free emission processes. The net effect on the CMB spectrum is a decrease of the temperature in the Rayleigh-Jeans region and an increase in the Wien range [130] as described by the following equations:

$$(\Delta T/T)_{RJ} \simeq -2y \qquad\qquad (\Delta T/T)_W \simeq 2y(-2 + x/\tanh x) \tag{3}$$

where:

- $x = h\nu/2KT_r$
- $y = \int_{t_{min}}^{t_{max}} K(T_e - T_r)/(m_e c^2)\sigma_T N_e(z) c dt$. y is known as the Compton parameter; T_e and T_r the temperature of electrons and photons respectively; K the Boltzmann constant; m_e the electron mass; σ_T the cross-section for Thomson scattering Thomson and $N_e(z)$ the electronic density.

In addition, to the above effect, know as thermal Sunyaev-Zel'dovich effect, we also have the kinematic Sunyaev-Zel'dovich effect. The latter is due to the peculiar movements with respect to the CMB of clouds of gas within the cluster. These movements can also produce anisotropy due to the Doppler effect so that if the cloud is moving with a peculiar radial velocity v_r and the optical opacity is τ_T then [131, 132]:

$$\frac{\Delta T}{T} = -\frac{v_r}{c}\tau_T \tag{4}$$

Because equation (4) contains no dependence on the frequency, it is possible to distinguish between them by observing at two frequency bands. The Sunyaev-Zel'dovich has been already observed in several clusters of galaxies with detections at 4σ levels and with amplitude $\Delta T/T \sim 10^{-5}$ [15].

Both the SZ effect and the Rees-Sciama effect are relevant at angular scales of arc minutes. Detections of the Sunyaev-Zel'dovich effect are susceptible to provide very useful information about the structures generating anisotropy: N_e, T_e, effective radius of the gas clouds and peculiar velocities as well as an alternative means of obtaining estimates for the value of H_0. On the other side, the upper limits imposed on the Rees-Sciama put constraints on the mass and density contrast of galaxy clusters such as the Great Attractor.

Finally, it is worth telling about possible distortions and angular anisotropy due to lensing caused by accumulations of matter. This effect would be relevant at arc minute angular scales and could result in amplifications of $\Delta T/T$ up to a 10 % depending on the cosmological model used [20].

1.1.4 Reionization

In the framework of the Standard Model, the baryonic matter first combined to form neutral atoms around redshift $z_m \sim 1100$ and in this way it has remained till nowadays, allowing for the light to travel from then till us. However, in several theoretical scenarios there is the possibility of having a reionization and a posterior recombination. This would have serious implications on CMB anisotropy depending on the redshift at which this reionization took place. According to [134], the reionization results unavoidable in most Cold Dark Matter[7]. Setting aside theoretical questions it is plausible thinking of the Universe having undergone a reionization process in view of some observational data [129, 121]:

- It is quite plausible to think of the processes leading to formation of structures not being efficient at 100%. Accordingly it would be expected to have some neutral hydrogen in appreciable abundances in the intergalactic medium. However, observations of sources at large distances do not indicate the presence of such hydrogen. In fact, from the results of the Gunn-Peterson test indicate that the upper limit on the fraction of neutral hydrogen in the Intergalactic medium is less than 10^{-6}.
- Observations of the intracluster gas indicate that there was a considerable injection of metals in the early stages of galaxy formation era. Such conclusion is reached from observations which demonstrate a higher abundance of iron in the intra-cluster medium than the typical iron abundances in the stars belonging to such clusters. This implies that clusters underwent a period of great activity prior to the star formation stage.
- Deep field observations indicate an excess population of faint blue dwarf galaxies if an attempt is to be made to account for the deep galaxy counts. The absence of present day counterparts is explained in terms of these galaxies having ejected large amounts of their initial mass by means of supernova-driven winds.

The first point strongly supports the possibility of a late reionization. In addition, in CDM scenarios it is inevitable to resort to this process if one wants to explain the discrepancies between

---

[7] The standard Cold Dark Matter model assumes that basically all the matter in the Universe is in the form of cold dark matter: heavy weakly interacting particles decoupled long ago when they had already reached non-relativistically velocities models.In this model, initial perturbations were of adiabatic type with a scale-invariant Harrison-Zel'dovich spectrum of the form: $P(k) = Ak^n$ with $n = 1$

theoretical predictions and observational data at arcmin scales. The remaining two points are observational data which suggest there were great releases of energy which could have caused reionization of the intergalactic medium at $z = 80$ [134, 121].

The effect of reionization on CMB anisotropy is of special concern at angular scales of a few arcmin. At these scales CMB primary anisotropy would be completely erased and replaced by secondary anisotropy. In general, all angular scales smaller than the horizon size at the time of reionization would be affected if not completely deleted [129]. Additionally, one should also consider the Vishniac effect which consists in the generation of new anisotropy at arcmin scales due to the coupling of electrons moving with fluctuations in the density of these electrons. The reionization efficiency on the damping of anisotropy is highly dependent on the redshift at which it occurred.

Finally it should be mentioned that because of the feedback processes causing reionization, the anisotropy left over by this process on the CMB can be non-Gaussian even when prior to reionization it was Gaussian [121].

1.1.5 CMB Spectrum

The Standard Big Bang model predicts a Planckian spectrum for the CMB. The origin of this Planckian spectrum dates back to the lepton era when energies were so high that continuous creation of electron-positron pairs occured with enough frequency to ensure thermal equilibrium. Eventually, with the expansion of the Universe and its subsequent cooling, electron-positron pairs annihilate but are not formed any longer, leaving radiation and a hot plasma composed by a very small number of density of electrons (as compared to the previous situation), protons, neutrons and He nuclei to interact with the radiation and a background of neutrinos which would have decoupled much earlier. The interaction matter-radiation becomes more and more scarce and eventually no thermal equilibrium can be sustained with those infrequent interactions. When no equilibrium can be sustained, CMB keeps its Planckian character and its temperature evolves according to the well known behavior:$T_{CMB} \propto (1+z)$. The posterior transition from ionized plasma to neutral atoms (i.e. recombination) has no effect on the spectrum of the CMB given the very low specific entropy of all present species (on average there are 10^9 photons per nucleon).

That would be the whole picture unless different energy injections mechanisms acting at different times show up. Any injection mechanism at $z \geq 10^7$ has no effect on the CMB spectrum as it is thermalized to the plasma and a new thermal equilibrium is reached [130]. The study of deviations of the CMB spectrum from its Planckian nature have the ability to provide information on processes after $z = 10^7$. Such deviations are characterized in terms of the Compton parameter y and the chemical potential μ depending on the time they occurred [131, 149, 85, 126]:

- Very early release of energy at $z \sim 10^5 - 10^7$ may be due to the decay of relic particles or primordial inhomogeneities. Because the interaction matter-radiation is dominated by multiple Compton scattering with the electrons, the radiation field achieves a statistical equilibrium characterized by a Bose-Einstein spectrum with a non-zero chemical potential μ [126]:

$$B_\nu(T;\mu) = \frac{2h\nu^3}{c^2}\frac{1}{e^{x+\mu}-1} \qquad x \equiv \frac{h\nu}{KT}$$

The fractional energy released ($\Delta U/U$) is related to the value of μ according to: $\Delta U/U \simeq 0.71\,\mu$ [149, 126]

- Energy release at $z \lesssim 10^5$ would transfer energy from the electrons to the photons via Compton scattering ($\gamma + e \to \gamma' + e'$). This is the same physical mechanism as the Sunyaev-Zel'dovich effect and it is characterized by a Compton parameter $y < 1$ for most standard models. The distortions in the Rayleigh-Jeans part of the spectrum to the y parameter according to $\Delta T_{RJ} = -2yT_{CMB}$ and the released energy is $\Delta U/U = e^{4y} - 1$. The net effect is a new spectrum which is the mixture of several black body spectra at different temperatures.
- Very late energy releases at $z \ll 10^3$ create spectral distortions via free-free emission. This is of concern in the case of recent reionization or from a warm intergalactic medium [126].

1.2 The Angular Power Spectrum of CMB Fluctuations

In the previous section several different mechanisms responsible for anisotropies of the CMB have been presented in a very qualitative way. This section is aimed to present how their effects can be assesed from measurements of the CMB fluctuations and what information can be extracted from them.

1.2.1 Multipolar Analysis

It is convential in CMB anisotropy studies to meet the anisotropy field decomposed in the so-called multipole moments. The decomposition in terms of a series of spherical harmonics of a scalar field defined on the sphere is the analogous to what we would do if we were working on a Euclidian space, namely, a Fourier decomposition in a series of harmonics. Therefore, it is not surprising that all works on the CMB anisotropy start decomposing the temperature anisotropy field as (e.g. [14, 115]):

$$\frac{\Delta T}{T}(\theta,\phi) \equiv \frac{T(\theta,\phi) - T_b}{T_b} = \sum_{m=-1}^{1} a_{1,m}Y_{1,m}(\theta,\phi) + \sum_{\ell\geq 2}\sum_{m=-\ell}^{\ell} a_{\ell,m}Y_{\ell,m}(\theta,\phi) \qquad (5)$$

where:

- T_b is the monopole term, i.e., the averaged temperature of CMB.

- The first summatory in the expansion would be the cosmological dipolar component, completely masked by the dipolar anisotropy caused by our peculiar movement with respect to the LSS. Becuase the dipolar anisotropy caused by our movement is orders of magnitude larger than the cosmological dipolar anisotropy (i.e, that obtained from the multipolar analysis) no attempt is made to recover it and is completely neglected.

- In the frame of scenerios in which fluctuations are generated by gravitational growth of quantum fluctuations amplified during a possible inflationary period, the coefficients $a_{\ell,m}$ are distributed as Gaussian random variables with 0 mean. On topological defect or string scenarios these coefficients $a_{\ell,m}$ do not follow Gaussian statistics.

When constructing the auto-correlation function of the fluctuations on the sky we obtain:

$$C(\alpha) \equiv \left\langle \frac{\Delta T}{T}(\theta,\phi)\frac{\Delta T}{T}(\theta',\phi') \right\rangle = \frac{1}{4\pi}\sum_{\ell\geq 2}^{\infty}(2\ell+1)C_\ell P_\ell(\cos\theta) \tag{6}$$

where:

- α is the angle between the directions specified by (θ,ϕ) and (θ',ϕ').

- C_ℓ are the coefficients of a Legendre decomposition of the auto-correlation function and are related to the $a_{\ell,m}$'s according to:

  $$\left\langle a^*_{\ell,m}, a_{\ell',m'} \right\rangle = C_\ell \delta_{\ell,\ell'}\delta_{m,m'} \tag{7}$$

  with * denoting complex conjugation.

- P_ℓ are the Legendre polynomials.

Three key points are needed to understand the importance of all this analysis:

1. In equations (6) and (7), $<,>$ denote ensemble averages. It is convinient to remark that in our description of CMB fluctuations we deal with this scalar field as being a realization of a random field. No theoretical model can predict the exact values we would observe in the CMB, but rather they will give predictions on the statistical moments describing such random field. In fact, if CMB fluctuations are indeed a Gaussian random field it will suffice to specify the values of the first moment (i.e., the mean which is known in advance to be zero by definition) and the second moment(the auto-correlation function) or equivalently, they provide the values for C_ℓ. This explains why we are so interested in both obtaining the value of $C(\theta)$ and why we would like so much the CMB be a Gaussian random field, and the most fashionable current cosmological scenario predicts so.

2. The result in equation (7) is a direct consequence from the orthonormality of the $Y_{\ell,m}(\theta,\phi)$ functions over the sphere and that the temperature fluctuations forms an isotropic and homogeneous random field, as required in equation (6). Then, equation (7) can be easily derived using the aforesaid orthonormality and the addition theorem for spherical harmonics.
3. The plot $[\ell(\ell+1)C_\ell/(2\pi)]^{1/2}$ versus ℓ is the so famous angular power spectrum, which is found in all references to CMB anisotropy. In addition to what we have seen in point (1), now we understand why it is so important on CMB studies: it has already been remarked throughout this thesis that the angular power spectrum is sensitive to the most crucial cosmological paramaters. Therefore, once it has been obtained with a good S/N ratio we should be able to obtain estimates of those parameters with unprecedent accuracy.

1.2.2 Theoretical Computations of the C_ℓ's

Theoretical computations of the angular power spectrum of CMB anisotropy require numerical integration of the Boltzmann equation for the coupled matter-radiation fluid. This has been a field of tremendeous development during the last few years, and now there are written programs accesible through the web which do these integrations. At the moment of writing this thesis, the most popular is the CMBFAST code [118] which also provides the polarization of CMB and its cross-correlation with the temperature anisotropy; probably something on which we will have to resort to break down the degeneracy on parameter estimation (also known as cosmic confussion) if only CMB anisotropies are considered. In addition, there are also very good accurate analytic approximations containing the explicit dependence on the cosmological parameters of interest [60] and providing very valuable insight on the physical mechanisms causing CMB fluctuations. In any case, only for anisotropies at very large angular scales (the so-called Sachs-Wolfe *plateau* in the CMB angular power spectrum) it is possible to have an analytical expression which easily relates the values for C_ℓ with two important cosmological parameters, namely, the spectral index of the inital perturbations[8] and the Hubble constant H_0 (see [18] for a very lucid derivation):

$$\begin{aligned} C_\ell &= \frac{(2H_0)^{n+3}}{64\,\pi^{3/2}} \frac{\Gamma(\frac{3-n}{2})\,\Gamma(\frac{2\ell+n-1}{2})}{\Gamma(\frac{4-n}{2})\Gamma(\frac{2\ell+5-n}{2})} \\ &= \frac{4\pi}{5} Q^2_{rms-PS} \frac{\Gamma(\frac{2\ell+n-1}{2})\Gamma(\frac{9-n}{2})}{\Gamma(\frac{2\ell+5-n}{2})\Gamma(\frac{3+n}{2})} \end{aligned} \qquad (8)$$

where $Q^2_{rms-PS} = 5C_2/(4\pi)$ is commonly used to state the normalization of the power spectrum. This is the ensemble average of the squared quadrupole, and because of the bias introduced when squaring a random variable and comparing the squared ensemble-average value with the ensemble-average value of the squared random variable , its root square will slightly differ from the ensemble average of the quadrupole $< Q_{rms-PS} >$ (see again [18] for a discussion on this). This last quantity is what we want to compare with the observed quadrupole.

---

[8] So far we are assuming an initial density perturbation field $\delta(\vec{r}) \equiv (\rho(\vec{r}) - \overline{\rho})/\overline{\rho}$ which is homogeneous and isotropic and characterized by a power-law spectrum of the form: $< \tilde{\delta}_{\mathbf{k}} \tilde{\delta}^\star_{\mathbf{k}'} >= P(k)\delta_D(\mathbf{k}-\mathbf{k}')$ where δ_D is the 3-dimensional Dirac's delta

1.2.3 Introducing Instrumental Effects

When comparing theoretical predictions with observational data we must also take into account the way in which the instrument performs the measurement. Thus , the effects introduced by the finite beam-width and the measurement strategy of a particular instrument are considered within its window function. The auto-correlation function of the fluctuations seen by a particular experiment are the convolution of the intrinsic auto-correlation function of the CMB anisotropies with the window function, and this is easily written resorting to the convolution theorem in spherical coordinates as:

$$C_{obs}(\theta;\sigma) = \frac{1}{4\pi}\sum_{\ell\geq 2}^{\infty}(2\ell+1)C_\ell P_\ell(\cos\theta)W_\ell(\theta) \tag{9}$$

where the σ symbol as an argument of C_{obs} makes explicit reference to the beam width of the experiment.

The window function for a given experiment describes how sensitive to the different ℓ's the experiment is. The window function for the experiment in this thesis is obtained in chapter 2 and can be seen in figure 6.

Until not very long ago, most experimental groups assumed a given auto-correlation function for the underlying signal, namely, a Gaussian Auto-Correlation Function (GACF). This has also been the approach in this work when it is time to analyze our final data sets. A detailed discussion on this choice and its implications can be found in Appendix A, while its application to the data in this thesis is described in chapter 7.

1.2.4 What Can Be Obtained from the CMB Anistropy Studies?

The interest on CMB anisotropy goes beyond of simply obtaining the power spectrum C_ℓ's to obtain its statistical description. Indeed, the computed values for the C_ℓ's depend very sensitively on both the assumed cosmological model as well as on the parameters of such model. Examples on the dependence of the CMB anisotropy spectrum on the variation of several cosmological parameters can be found in chapter 7.

Accordingly, CMB data can provide very useful cosmological information which can be divided into two main categories:

- Parameters of Classical Cosmology which includes H_0, Ω, Ω_b and Λ (e.g. the Hubble constant, the present density of the Universe relative to the critical density, the contribution of baryonic matter to the total matter of the Universe and the analogous due to the cosmological constant). Especially relevant is any estimate of Ω for it translates in what the geometry of the Universe and its ultimate fate are. In definitive, by obtaining estimates of these parameters it is possible to test the conerstones over which the Bing Bang Model is based.

- Parameters describing initial perturbations, which in turn are linked to the problem of structure formation in the Universe. In this category we include the parameters Q_S, n_S, Q_T,... (e.g. the quadrupole component of scalar fluctuations, the spectral index of the power spectrum of scalar perturbations, the the quadrupole component of tensor modes or gravity waves) and other inflationary observables. Given the tight relationships imposed by inflation on these, it turns out that its determination constitutes probably the only test to the Inflationary paradigm.

The problem as it is stated at this moment is a classical example of inverse problem. Detailed works (e.g see [62, 63, 65]) on how well the above parameters can be extracted by fitting the observed CMB angular power spectrum to theoretical predictions. At present the large uncertainties of the available data points leave little room for an analysis as that proposed by the above works. They are mainly intended to apply to the much better data expected from the future space missions MAP and PLANCK. These works also stress the computational difficulties to be met with a traditional fitting process to those data: the parameter space is a 11 dimension space and degenerations are expected to be met. The last difficulty is expected to be overcome with the use of the additional information provided by polarization maps of CMB. According to these authors, estimates for these parameters with a few percent accuracy are potentially attainable by using only CMB data, with the accuracy being increased if additional information is used to constrain the range of parameter variation in the fitting process (e.g., primordial nucleosyntesis results, large-scale results,...).

1.3 Experimental Status

1.3.1 On the CMB Spectrum

The most accurate measurements of T_{CMB} are those provided by the rocket experiment COBRA and the spatial experiments FIRAS and DMR on board COBE satellite. The results of these experiments were reported in [49] for the COBRA experiment and [84, 85, 39, 40, 41] among others for the COBE mission. The first reported measurements from FIRAS instrument reporting $T_{CMB} = 2.735 \pm 0.060$ K [84] at 95% CL and a deviation from a perfect blackbody spectrum of less than 1% at its brightness peak. [85] refined the analysis and recalibration of the instrument gave $T_{CMB} = 2.726 \pm 0.010$ K with a deviation from the blackbody spectrum less than 0.03 % at its brightness peak. Both results are consistent with each other and with the values from COBRA experiment reported by [49]: $T_{CMB} = 2.736 \pm 0.017$ K. The most accurate value to date is obtained from the analysis of the full FIRAS data set in [40] yielding $T_{CMB} = 2.728 \pm 0.004$ K with a deviation of less that 0.005% at the brightness peak.

Table 1: Measurements of T_{CMB}

Reference	T_{CMB} (K)	Frequency (GHz)	Technique
Bennett *et al.* 1996	2.725 ± 0.020	31,53,90	DMR on board COBE
Fixsen *et al.* 1994	2.714 ± 0.022	[60,600]	FIRAS on board COBE
Bersanelli *et al.* 1994	2.55 ± 0.14	2.0	Total power radiometer from South Pole
Kogut *et al.* 1993	2.75 ± 0.05	31,53,90	DMR on board COBE
Roth *et al.* 1993	$2.729^{+0.023}_{-0.031}$	113	Spectroscopy of interstellar CN
Bensadoun *et al.* 1993	2.26 ± 0.19	1.47	Total power radiometer from California and South Pole
Levin *et al.* 1992	2.64 ± 0.06	7.45	Total power radiometer from South Pole
De Amici *et al.* 1991	2.64 ± 0.07	3.8	Total power radiometer from South Pole
Sironi *et al.* 1991	2.7 ± 1.6 2.5 ± 0.34	0.82 2.5	Differential radiometers from South Pole
Kaiser y Wright,1990	2.74 ± 0.04	113	Spectroscopy of interstellar CN
Sironi *et al.* 1990	3.0 ± 1.2	0.6	Total power radiometers from Italian Alps
Kogut *et al.* 1990	2.60 ± 0.07	7.45	Total power radiometers from California
Crane *et al.* 1989	$2.796^{+0.014}_{-0.039}$	113	Spectroscopy of interstellar CN
Crane *et al.* 1986	2.83 ± 0.09	113	Spectroscopy of interstellar CN
Meyer & Jura, 1985	2.70 ± 0.04	113	Spectroscopy of interstellar CN

These values impose very severe limits on the Compton y parameter and on the chemical potential μ: $|y| < 1.5 \times 10^{-5}$ and $|\mu| < 9 \times 10^{-5}$ both at 95% CL. These values put serious constraints on the validity of the Steady State theory[9]. Other measurements on T_{CMB} using several other techniques are briefly described in table 1.

---

[9] According to the Steady State theory, the CMB would be due to the thermalization by dust of the interstellar and intergalactic radiation fields at shorter wavelengths. In order to have a spectrum so close to a blackbody we would need such an optical depth which would avoid any observation of distant galaxies and quasars at millimetric wavelengths

Table 2: Detections of the Dipole Anisotropy.

Reference	ΔT (mK)	Dipole Direction	Frequency
Fixsen *et al.* 1994	3.343 ± 0.016	$(\alpha,\delta) = (168.9° \pm 0.5°, -7.5° \pm 0.5°)$	[60,600]
Bennet *et al.* 1993‡	3.353 ± 0.024	$(l,b) = (264.3° \pm 0.3°, 48.22° \pm 0.13°)$	31,53,90
Kogut *et al.* 1993‡	3.365 ± 0.027	$(l,b) = (264.4° \pm 0.3°, 48.4° \pm 0.5°)$	31,53,90
Klypin *et al.* 1992	3.16 ± 0.12	$(\alpha,\delta) = (11^h 17^m \pm 10^m, -7.5° \pm 2.5°)$	37.5
Smoot *et al.* 1992‡	3.36 ± 0.10	$(l,b) = (264.7° \pm 0.8°, 48.2° \pm 0.5°)$	31,53,90
Smoot *et al.* 1991‡	3.3 ± 0.2	$(\alpha,\delta) = (11.2^h \pm 0.2^h, -7° \pm 2°)$	31,53,90
Halpern *et al.* 1988	3.40 ± 0.42	$(\alpha,\delta) = (12.1^h \pm 0.24^h, -23° \pm 5°)$	176.3
Lubin *et al.* 1985	3.44 ± 0.17	$(\alpha,\delta) = (11.2^h \pm 0.1^h, -6.0° \pm 1.5°)$	99.9

‡ All these values were obtained and differ from each other in the amount of data employed and data analysis. Therefore they can not be taken as independent measurements.

1.3.2 Observational Status on Dipole Anisotropy

This was the only detected component of anisotropy until the detection of quadrupolar anisotropy by COBE in 1992 [125]. The first detection of dipolar anisotropy was made in in 1976 by [24] who initially quoted a value of $\Delta T = 2.9 \pm 0.7 mK$ with a dipole direction$(\alpha,\delta) = (13^h \pm 2^h, -25° \pm 20°)$. To date, the most precise measurement of the dipole anisotropy is that obtained from the analysis of the spectrum of the dipolar anisotropy with the FIRAS instrument on board COBE satellite [40]. These measurements yield a value for the dipole amplitude of $\Delta T = 3.372 \pm 0.014\ mK$ and for the dipole direction $(l,b) = (264.14° \pm 0.30°, 48.26° \pm 0.30°)$.

The most recent measurements of the dipole anisotropy together with its spectrum strongly support the interpretation of being caused by our peculiar movement with respect the CMB rest frame. From the value of dipole anisotropy reported in [69], the peculiar velocity of the Local Group is $v_{LG} = 627 \pm 22\, Km\, s^{-1}$ towards the direction $(l,b) = (276° \pm 3°, 30° \pm 3°)$. The slightly more refined values found in [41] implies a Sun's peculiar velocity of $v_{\odot} = 371 \pm 1\, Km\, s^{-1}$ towards $(l,b) = (264.14° \pm 0.15°, 48.26° \pm 0.15°)$. In table 2 we give a list with other detections of the dipole anisotropy.

1.3.3 Status of Observations of CMB Anisotropy at Several Angular Scales

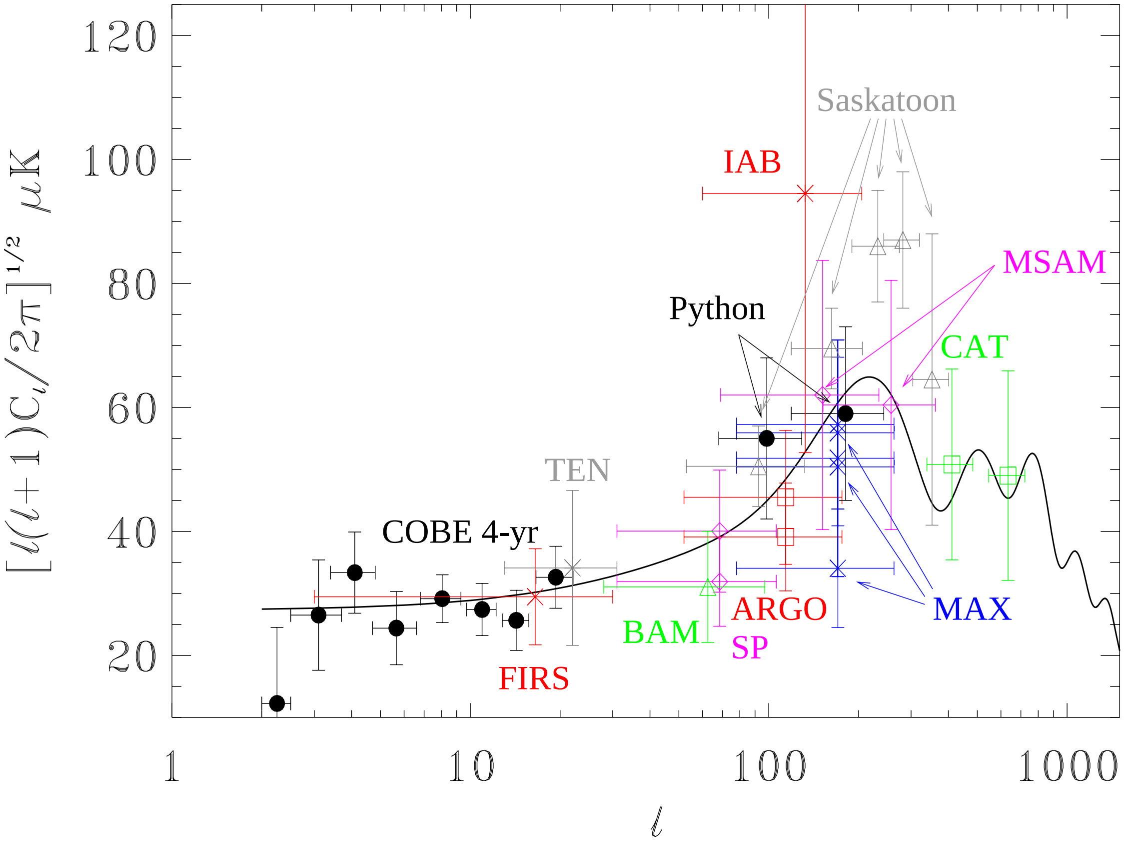

Figure 1: Current Observational Status. The solid line shows the standard CDM model with the parameters described in main text.

Until not very long ago quoting experimental information from several different experiments was something confusing and difficult to compare among them. The main reason for this situation was the way in which data was analyzed and results were presented. Then it was quite common to analyze CMB data in terms of Gaussian Auto-Correlation Function (GACF, see appendix A) so that a particular experiment would report an estimate of $C_0^{1/2}$ at a given angular scale θ_c. This angular scale is known as *coherence angle* and was extremely dependent on both the beam size and measurement. This situation has somehow changed with the introduction of the so-called Flat Band Power Estimate (FBPE,see appendix A) which allows for a very natural comparison between data from different experiments by assuming that within the angular range sampled by a given experiment the CMB angular power spectrum is flat. Further, there are in the literature (See also appendix A) easy prescriptions to convert GACF results to the equivalent FBPE result. To do so, we only need information on the experimental window function. Using this FBPE notation we show in figure 1 the detections for the latest experiments sampling the CMB power spectrum up to $\ell \sim 600$. Beyond this point only upper limits are available. The FBPE results listed inn table 3 have been obtained from the compilation of results done by [136, 119, 78, 109] and available in the web site [136]. The quoted ℓ-ranges are centred in the effective ℓ value and the upper and lower limits indicate where the window functions drop to half of its peak. The dark solid line in figure 1 corresponds to the power spectrum predicted by a standard CDM model normalized to COBE measurements as obtained with CMBFAST [118]for the following combination of cosmological parameters: $H_0 = 50\ Km\,s^{-1}\,Mpc^{-1}$ (Hubble constant), $Y_P = 0.24$ (primordial He abundance), $N_\nu = 3$ (number of families of light neutrinos), $N_{\nu,mass} = 0$ (number of families of massive neutrinos), $\Omega_b = 0.05$ (contribution of baryons to the density parameter), $\Omega_{CDM} = 0.95$ (contribution of Cold Dark matter to the density parameter), $\Omega_\Lambda = \Omega_\nu = 0$ (contribution of the cosmological constant and of massive neutrinos to the density parameter), $r = 0$ (no tensor fluctuations), no reionization and adiabatic (or isentropic) initial conditions with $n = 1$. As shown in figure 1, all measurements except those by COBE which are limited by Cosmic Variance, exhibit very large error bars. Yet, measurements at $\ell \sim 200$ seem to indicate the presence of the so-called Doppler peak and some attempts have already been made in order to extract cosmological information from such data [78, 109, 56].

Table 3: Current Observational Status on CMB Anisotropy.

Reference	Experiment	$\delta T_\ell \equiv \sqrt{\bar\ell(\bar\ell+1)C_{\bar\ell}/(2\pi)}$ (μK)	$\bar\ell$
Tegmark & Hamilton 97	COBE 1	$8.5^{+16.0}_{-8.5}$	$2.1^{+0.4}_{-0.1}$
Tegmark & Hamilton 97	COBE 2	$28.0^{+7.4}_{-10.4}$	$3.1^{+0.6}_{-0.6}$
Tegmark & Hamilton 97	COBE 3	$34.0^{+5.9}_{-7.2}$	$4.1^{+0.7}_{-0.7}$
Tegmark & Hamilton 97	COBE 4	$25.1^{+5.2}_{-6.6}$	$5.6^{+1.0}_{-0.9}$
Tegmark & Hamilton 97	COBE 5	$29.4^{+3.6}_{-4.1}$	$8.0^{+1.3}_{-1.2}$
Tegmark & Hamilton 97	COBE 6	$27.7^{+3.9}_{-4.5}$	$10.9^{+1.3}_{-1.2}$
Tegmark & Hamilton 97	COBE 7	$26.1^{+4.4}_{-5.3}$	$14.3^{+1.4}_{-1.5}$
Tegmark & Hamilton 97	COBE 8	$33.0^{+4.6}_{-5.4}$	$19.4^{+2.7}_{-2.8}$
Ganga *et al.* 1994	FIRS	$29.4^{+7.8}_{-7.7}$	10^{+20}_{-7}
Hancock *et al.* 1997	Tenerife	$34.1^{+12.5}_{-12.5}$	20^{+11}_{-7}
Gundersen *et al.* 1995	SP 91	$30.2^{+8.9}_{-5.5}$	57^{+49}_{-26}
Gundersen *et al.* 1995	SP 94	$36.3^{+13.6}_{-6.1}$	57^{+49}_{-26}
Tucker *et al.* 1996	BAM	$29.5^{+10.5}_{-7.4}$	74^{+23}_{-46}
de Bernardis *et al.* 1994	ARGO 1	$39.1^{+8.7}_{-8.7}$	95^{+81}_{-43}
Masi *et al.* 1996	ARGO 2	$46.8^{+9.5}_{-12.1}$	95^{+81}_{-43}
Tanaka *et al.* 1996	MAX GUM	$54.5^{+16.4}_{-10.9}$	145^{+118}_{-67}
Tanaka *et al.* 1996	MAX ID	$46.3^{+21.8}_{-13.6}$	145^{+118}_{-67}
Tanaka *et al.* 1996	MAX SH	$49.1^{+21.8}_{-16.4}$	145^{+118}_{-67}
Tanaka *et al.* 1996	MAX HR	$32.7^{+10.9}_{-8.2}$	145^{+118}_{-67}
Tanaka *et al.* 1996	MAX PH	$51.8^{+19.1}_{-10.9}$	145^{+118}_{-67}
Platt *et al.* 1996	Python 1	$54.0^{+14.0}_{-12.0}$	92^{+37}_{-24}
Platt *et al.* 1996	Python 2	$58.0^{+15.0}_{-13.0}$	177^{+66}_{-58}
Piccirillio *et al.* 1993	IAB	$94.5^{+41.8}_{-41.8}$	125^{+80}_{-65}
Cheng *et al.* 1996	MSAM 3	$62.0^{+21.7}_{-21.7}$	143^{+91}_{-74}
Cheng *et al.* 1996	MSAM 4	$60.4^{+20.1}_{-20.1}$	249^{+113}_{-97}
Netterfield *et al.* 1996	Saskatoon 1	$49.0^{+8.0}_{-5.0}$	86^{+46}_{-33}
Netterfield *et al.* 1996	Saskatoon 2	$69.0^{+7.0}_{-6.0}$	166^{+40}_{-47}
Netterfield *et al.* 1996	Saskatoon 3	$85.0^{+10.0}_{-8.0}$	236^{+38}_{-46}
Netterfield *et al.* 1996	Saskatoon 4	$86.0^{+12.0}_{-10.0}$	285^{+35}_{-42}
Netterfield *et al.* 1996	Saskatoon 5	$69.0^{+19.0}_{-28.0}$	348^{+53}_{-44}
Scott *et al.* 1996	CAT 1	$50.8^{+15.4}_{-15.4}$	396^{+87}_{-57}
Scott *et al.* 1996	CAT 2	$49.0^{+16.9}_{-16.9}$	608^{+114}_{-62}
Ganga *et al.* 1997	SuZIE	$0.0^{+27.0}_{-0.0}$	2340^{+1330}_{-1010}

Chapter 2

Instrumental Setup & Measurement Technique

The instrument employed to collect the data presented in this work was made from the combination of elements from two earlier experiments. The telescope was used in Antarctica coupled to a bolometric detector operating at 2.2 mm and reported a detection shown in figure 1 with the label IAB. On the other side, the dewar containing the detectors was part of an unsuccessful MIT attempt to measure CMB anisotropy from the South Pole at wavelengths 3.3, 2.1, 1.3 and 1.1 mm. The dewar was lent to Dr. Lucio Piccirillo, then at Bartol Research Institute, who made some changes concerning mainly the optical filter at 3.3 mm and modification of the optical window to avoid the ^{3}He gas storage falling in the field of view of the bolometers. Figure 2 shows the three basic parts on which the instrument can be decomposed: telescope, cryostat with cold optics and acquisition system. Additionally the instrument was surrounded by a radiation shield designed to avoid ground contamination. The radiation shield was made of aluminum panels tilted at an angle of 45° to minimize stray photons entering and remaining in the system.

2.1 Instrumental Setup

2.1.1 Telescope

The optics forms an off-axis Gregorian telescope resulting from the combination of a parabolic primary mirror with a focal length of 1.33 m and diameter of 45 cm coupled to an off axis hyperbolic secondary mirror of 28 cm diameters. The telescope uses an alta-azimuthal mounting with the elevation axis coinciding with the optical axis of elevation. The primary mirror is mounted on a guide rail allowing to set the elevation of the antenna without moving the cryostat. The primary mirror performs a sinusoidal wobbling in order to switch between different positions on the sky. This chopping can be performed either in azimuth or elevation, though in the configuration chosen

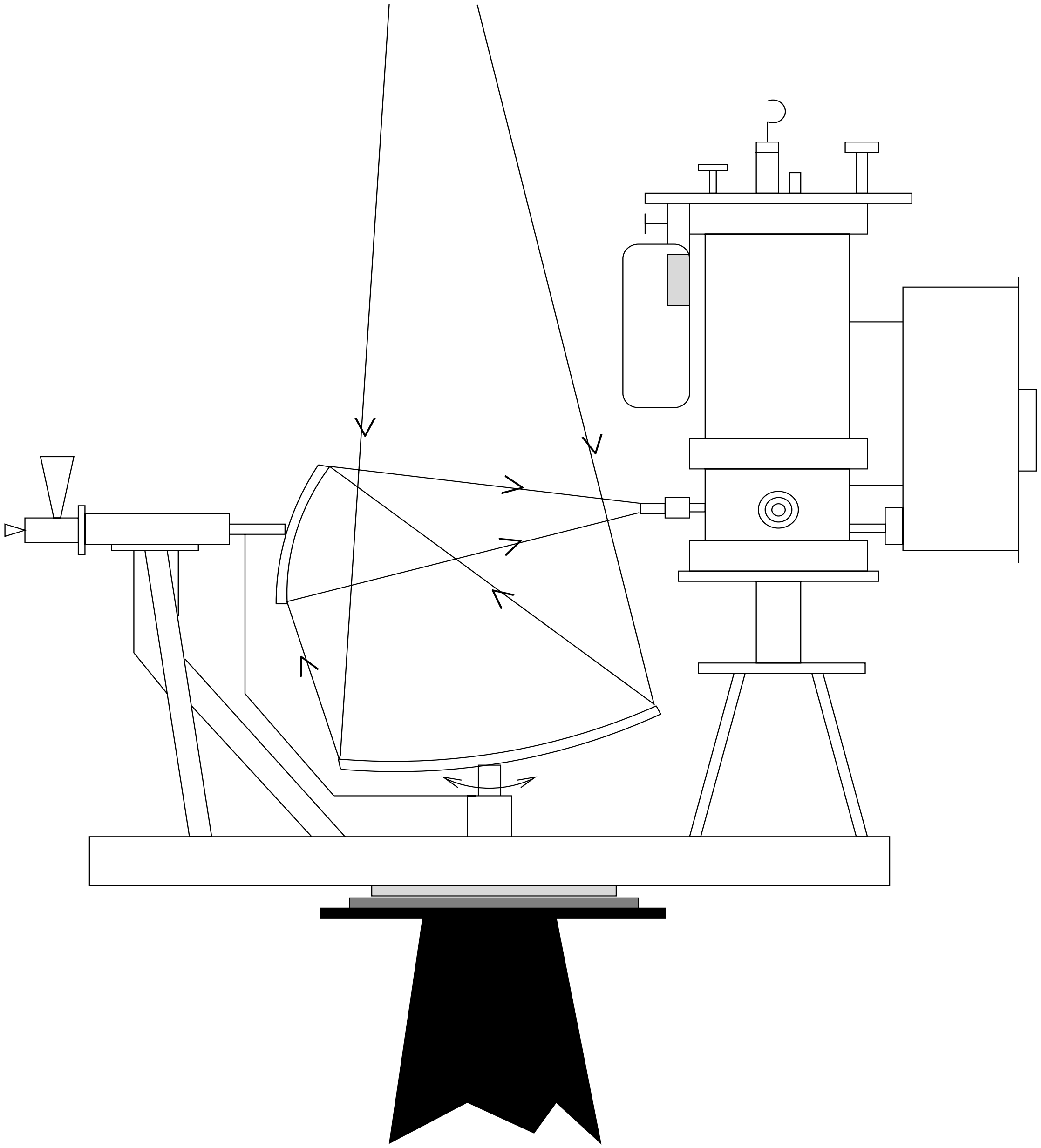

Figure 2: Scheme showing the three components of the experiment: telescope, cryostat and data acquisition system.

in this campaign it only wobbled in azimuth. For systems with a small primary mirror, this is a better choice than an oscillating secondary mirror because of the higher rejection to diffracted signals entering into the system and a higher efficiency in the reduction of the sidelobes. In addition, with a wobbling primary mirror we have a smaller differential illumination than that if we had a chopping secondary mirror [98].

The technical specifications can be obtained from [98]. In the design of the telescope special attention was paid to the use of light materials to make it easy to dismantle in case of strong winds which are likely to occur at Antarctica. To this purpose, the mirrors were made using silver-coated carbon reinforced plastic (CFRP). In order to minimize masses, aluminum and titanium were employed for the moving metallic parts coupled to the mirrors. The fixed structure of the antenna was made on stainless steel to give rigidity to the whole system.

2.1.2 Cryostat

The dewar containing the cold optics and the detectors is depicted in figure 3. It consists of a standard closed cycle ^{3}He refrigerator mounted inside a standard ^{4}He dewar. In order to minimize heat transfer by convection between the different chambers at different temperatures, the cryostat is pumped down. To minimize heat transfer by conduction through the wiring, very thin cables (0.0254 mm) were used (see [91] for a detailed explanation). The interior of the dewar, except for the aperture to insert ^{4}He, is surrounded by a radiation shield thermally coupled to a liquid N_2 bath at 77 K. This radiation shield is intended to absorb any IR photon crossing the outer wall of the cryostat and transferring its heat to the liquid N_2 bath. The ^{4}He bath will reduce further the temperature down to 4.2 K. It is thermally not coupled to the bolometer chamber for this still has to be cooled down to 0.35 K. This is accomplished with the closed ^{3}He refrigerator inside the cryostat. After the temperature in the ^{4}He pot is 4.2 K, the ^{3}He pot is filled and then the inside valve is open, connecting it with the zeolite chamber. This substance absorbs ^{3}He gas particles in the ^{3}He pot,mainly filled with liquid ^{3}He at 4.2 K, generating a high degree of vacuum and decreasing the vapor pressure so the temperature of ^{3}He can be pushed down to 0.35 K.

Cold Optics

Under the generic name of cold optics we refer to those optical parts contained within the cryostat and which are the interface between those optical pieces at ambient temperature (mirrors) and the detectors at 0.35 K.

The first element at 4.2 K composing the cold optics is a collector of photons entering the cryostat after reflexion from the mirrors.The collector employed is a Wiston cone characterized by allowing all photons in the filed of view and rejecting from the system stray photons entering the system. Attached to this we find a reversed Wiston cone so that the photons entering the system through the first concentrator travel parallel to the optic axis. The 4.2 K stage of the cold optics is ended with a filter to block high-frequency leaks. This is achieved with the combination

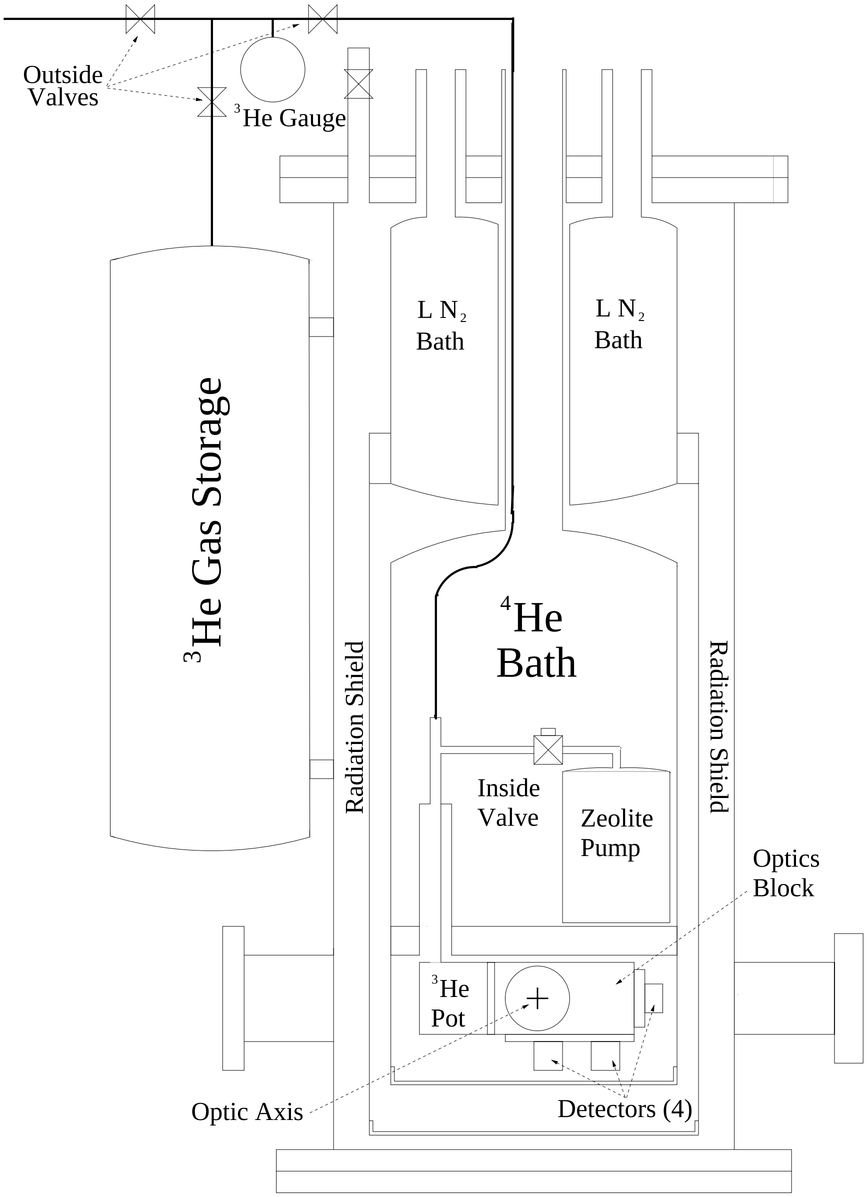

Figure 3: Dewar containing the 4 bolometric detectors.

of fluorogold, black polyethylene and Pyrex glass filters.

Table 4: Characteristics of Our Filters.

		Flat Spectrum		CMB Spectrum	
Channel	λ_{Peak} (mm)	$\overline{\nu}$ (GHz)	$\Delta\nu$ (GHz)	$\overline{\nu}$ (GHz)	$\Delta\nu$ (GHz)
1	3.3	97	26	97	25
2	2.1	169	32	146	30
3	1.3	243	45	238	44
4	1.1	270	47	265	46

The second stage of the cold optics is already in the bolometer chamber at a temperature of 0.35 K. To avoid thermal contact with the previous stage there is a gap between them. To avoid contaminating photons entering the bolometer chamber through the gap, a new fluorogold filter is used as a high frequency blocking element which efficiently removes most of those undesired photons. After going through this filter, the photons are splitted into two beams by means of a high frequency pass aluminum thick grill filter set at a 45 degree angle to the optic axis. Each optic tube leads to another beam designed to pass the appropiate frequencies so that at the end we have 4 beams wich means of corresponding Wiston cones are concentrated onto the individual bolometers. It is the combination of the initial fluorogold filter and subsequent beam splitters what defines the frequencies seen by each of our channels. The normalized transmission spectra for each of our bands are depicted in figure 4, summarized in table 4 in terms of the peak wavelegnth (λ_{Peak}), effective band centres ($\overline{\nu}$) and band dispersion ($\Delta\nu$) as obtained using the following prescriptions in [96]:

$$\overline{\nu}_i = \frac{\int \nu F_i(\nu) I(\nu)\, d\nu}{\int F(\nu) I(\nu)\, d\nu} \qquad \Delta\nu_i = \int F_i(\nu) I(\nu)\, d\nu I(\overline{\nu}_i)$$

where $F_i(\nu)$ is the normalized transmission at frequency ν for channel i in figure 4 and $I(\nu)$ is the reference spectrum, which in table 4 are a flat spectrum ($I(\nu)$ = constant) and a blackbody CMB spectrum.

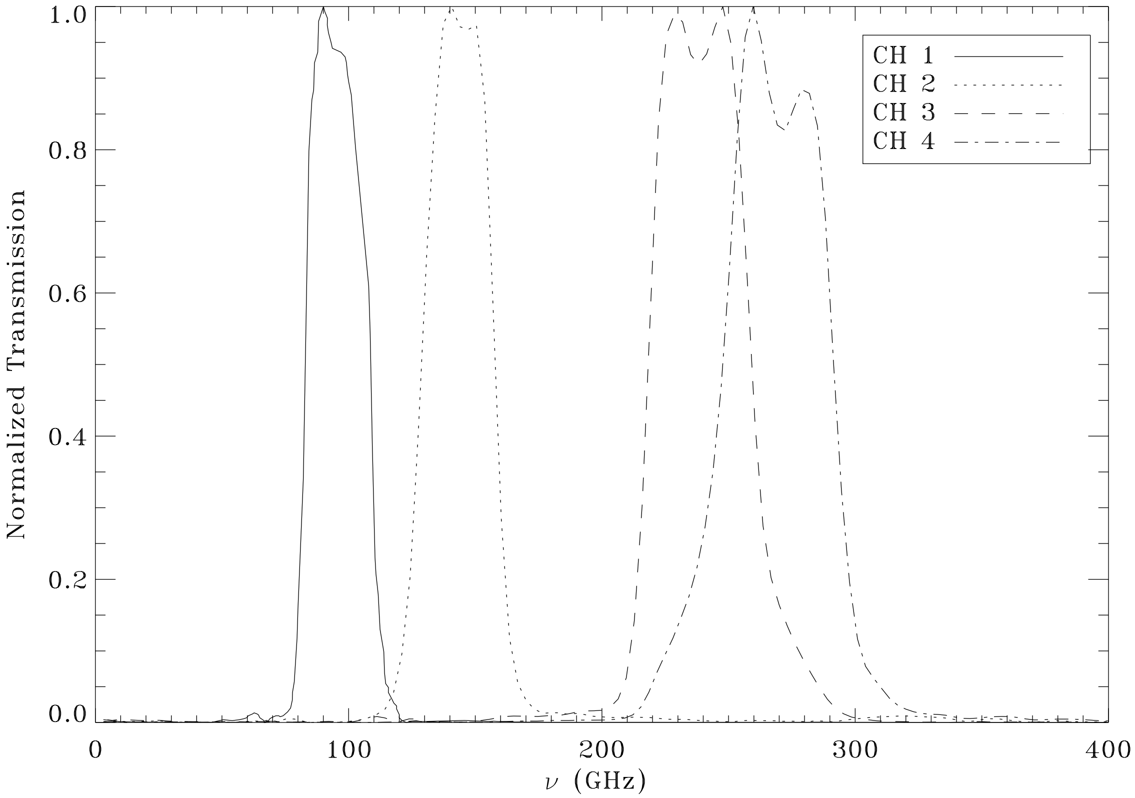

Figure 4: Normalized transmission spectra of the band-pass filters.

Detectors: Bolometers

The detector in our system was a four-channel photometer equipped with bolometers working in the frequency ranges above described by combination of suitable filters. From a simplistic point view, a bolometer is a piece of a given material whose electric resistance changes with temperature. By measuring the voltage between the two extremes of the piece of material we can find out how much energy was carried by the photons striking the piece of material.

A typical bolometer is made of six fundamental parts [108], namely the thermal absorber, the supporting substrate, the thermometer, the thermal link, the thermal sink and the mechanical support. For a god bolometer we require the following properties on the different components:

The thermal absorber must have the appropiate size to intercept the signal. It requires a larg absorptivity over the frequency range to be measured and a low heat capacity.

The supporting substrate should have a large thermal conductivity with a very low heat capacity in order to remain isothermal during bolometer operation.

The thermometer with a resistance R and attached either to the radiation absorbe or to the supporting substrate will exhibit a temperature response given by:

$$\alpha = \frac{1}{R}\frac{dR}{dT}$$

which expreses the temperature dependence of its electrical resistance and must be adequate to our purposes. Additionally we want this part of the bolometer to exhibit low electrical noise and low heat capacity.

The thermal link will transfer the absorbed heat by the radiation absorber and passed onto the supporting substrate to the thermal sink. It is required to have a low heat capacity and an appropiate thermal conductance.

The thermal sink will exhibit a stable temperature appropiate for the application. It is basically where we will throw out the heat without changing the temperature of the whole system.

The mechanical support must be stiff to avoid mechanical resonant frequencies higher than the operating frequencies of the bolometr. This part should exhibit low thermal conductance and low heat capacities so that no leaks can occur through this element.

The way a bolometer works is basically as follows. Photons strike the radiation absorber causing it to heat up. Because of its very low heat capacity and its good thermal conductivity all the heat is passed on the supporting substratewich retains no heat due to its very low heat capacity and thanks to its high thermal conductivity passes all the energy to the resistor (the thermometer). The resistor will heat up and this will cuase a change in its resistance which will be measured by means of reading out the voltage between its extremes (a small current known as bias current passes through the resistor). The thermal link is intended to transfer as fast a possible the heat from the active portions of the bolometer (ie., the abosorber or the substrate) to the heat sink. The velocity with which this heat transfer is done limits the response time of the bolometer τ_{eff} defined below.

The responsivity $S$of the bolometer as the volts read out per watt of incident signal power. The higher the responsivity is, the more sensitive our detector is. A simple bolometer response theory based in energy conservation arguments is sketched in [108] to obtain an expression for the responsivity in terms of the thermal properties of the different components above described:

$$S = \frac{V}{P} = \frac{IR\alpha}{G - I^2R\alpha + i\omega_S C} \tag{10}$$

where the presence of the complex i is justified because we are assuming incident periodic signal expressed in complex notation ($e^{i\omega_S t}$). In this picture, I is the bias current, R the resistor resistance under no incident radiation and G the thermal conductivity with the thermal sink. Because of thermal feedback caused by the aditional heating in turn caused by the change of resistance, some modifications need to be done. Thus, let us define a effective conductance G_{eff} and a time scale τ_{eff} given by:

$$G_{eff} = G - I^2R\alpha \qquad \tau_{eff} = C/G_{eff}$$

then the responsivity has a Lorentzian form given by:

$$S = \frac{IR\alpha}{G_{eff}(1 + i\omega\tau_{eff})} \tag{11}$$

Finally, it is worth mentioning about the noise in a bolometer and which is usually refered to as Noise Equivalent Power (NEP, in units of $W/\sqrt{Hz}$) and it is defined as the amount of power to be supplied to the bolometer in order to have a S/N ratio of 1. There are three sources of noise contributing to generate the final NEP:

- Johnson noise is simply the thermal noise in any resistor caused by the thermal motions of electric carriers in the resistor. Thse Brownian motions generate a zero mean current but not a zero mean power (i.e. $< I >= 0$ but the power is $P = R < I^2 >$)
- Phonon noiise, is the equivalent concept but due to the Brownian motion of thermal carriers in the lattice (i.e phonons).
- Photon noise due to the phonons coming from the source are expected to follow a Poisson distribution so that there are expected fluctuations in the number of photons arriving to the absorber.

These three sources of noise are independent from each other so they are added in quadrature when computing the values for the NEP. This final value must also consider the noise introduced by the different amplification stages (in our case achieved by a JFET amplifier) together with the amplification of the noise but such stage. In real life however, the appropiate choice of bolometer and amplifier puts most of the noise in the Johnson noise from the bolometer so the only effect of the amplifier is to amplify the bolometer noise. The laboratory measurements in the NEP values for our bolometers are 0.735, 0.373, 0.283 and 1.510 $mK/\sqrt{Hz}$ for channels 1 to 4 respectively.

2.1.3 Data Acquisition System

It can be thought as made of the three following parts :

1. Bolometers Electronic Box: this contains the batteries which power the bolometers and a set of amplifiers to amplify the output of each bolometer with a gain of 26 dB. The electronic box is shielded to avoid Radio Frequency interferences, and all external connections pass through a π filter to prevent RF noise entering the system. A second stage allows to amplify the signal of each channel i with a gain $(0.301G_i + 1)$ dB, where G_i can be varied as desired between 0 and 9 for each channel. By changing the gain factor G_i for channel i so we can perform observations of CMB or observations of a much brighter source of the Moon without saturating the ADC converters and having a good element of resolution (see below).

2. Analogic to Digital conversion with a 16 bit ADC and an input signal of $\pm 5\,V$. The input analogic signal is converted in $2^{16} = 65356$ discrete levels, so that the resolution (i.e minimum detectable signal change) is $0.15\ mV$. This is why we have amplified previously the signal so we do not waste dynamic range: if the input signal only reaches 0.1 V then we would be wasting dynamic range for our resolution element in Voltage is 0.15 mV (0.15 % of the signal), but if previous to the ADC the $0.1\ V$ signal is amplified to, let's say, $3\ V$ then the resolution is 0.005% of the input signal.

3. Transmission of the data with a serial line (RS232) and storage in a computer. Inside the data acquisition system a microprocessor collects the numbers from the ADC and from the housekeeping system (which controls the timing and moving of the mirror, temperature within the ^{4}He bath, etc). The microprocessor sorts these data in a series of 1 long frame and 19 short frames corresponding to the 20 samples for each mirror oscillation, and where the long frame indicates when a new mirror oscillation begins. The structure of these frames is:

   - Short frame= flag+ fast counter+ reading of the four channels
   - Long frame = short frame+ time counter + housekeeping information

   where:

   - The flags indicates whether this is a long or a short frame
   - The fast counter gives the time within a mirror cycle and it is used to compute the time of each sample (20 samples per cycle of mirror). The fast counter is a 24 bit counter and sets to zero every 54 s, implying a resolution of $3.2\ \mu s$
   - Time counter gives the UT.
   - Housekeeping information refers to voltages and temperatures to manage the system.

2.2 Instrumental Response

2.2.1 Demodulation of the Data and Mapping Function

In addition to the optics, the response of the instrument to a point-like source depends on the observing strategy and demodulation of the data ([147]). The observing strategy consisted in daily drift scans at constant declination achieved by fixing the telescope in azimuth (ϕ) and elevation (θ). Additionally the beam moves on the sky as the primary mirror wobbles sinusoidally at a frequency $f_w = 3.94 Hz$, while the secondary is fixed. The right ascension (α) and declination (δ) at which the antenna is pointing at time t are given in a good approximation by: $\delta(t) = \delta_0$ and $\alpha(t) = \alpha_0 + \beta_0/\cos(\delta_0) \times \sin(2\pi f_w t + \epsilon)$, where (α_0, δ_0) is the initial position of the antenna, $\beta_0 = 2.6°$ is the zero-to-peak chopping amplitude at a reference frequency $f_w = 4$ Hz and ϵ is an phase constant. Each bolometer's output is sampled at $f_s = 80$ Hz coherently with the mirror movement so to have 20 samples per mirror oscillation. The signal is demodulated in software by evaluating the amplitude of the first 1F (4 Hz) and second 2F (8 Hz) harmonic of the reference frequency f_w. In practical terms this is achieved by multiplying the data stream by sinusoidal functions of frequencies f_w and $2f_w$ for the 1F and 2F demodulations respectively. This product has to be coherent with the mirror's movement and this is the reason why the data acquisition system keeps record of the mirror's movement: we need to know the time of each sample with respect to the beginning of the cycle where the sample was taken. Because of failures or problems with the synchronism between movement of mirror and data acquisition system, a 3.3% of the total data had to be rejected.

Each demodulation (1F and 2F for the first and second harmonic respectively) can be divided in two components: the in-phase component containing mostly the sky-signal coherent with the reference motion plus the instrument noise and the out-phase containing mostly the instrument noise plus other sources of systematic noise. Such division requires a careful choice of phase which was obtained from observation of the Moon transiting the instrument beam. The concept of mapping function is somewhat equivalent to the concept of Point Spread Function in optics, but taking into account that we are not in position of doing image. By knowing the mapping function we can predict the response of our instrument to any source on the sky. We can easily obtain the expression for the mapping function of harmonic n at a sky location of coordinates (α, δ) when the antenna is pointing towards (α_0, δ_0):

$$M_{nF}(\alpha, \delta; \alpha_0, \delta_0) = \frac{N_n}{\sqrt{2\pi\sigma^2}} f_w \int_{-1/(2f_w)}^{1/(2f_w)} dt \, \cos(n \, 2\pi f_w t + \zeta) \exp\left[-\frac{\Delta^2(t)}{2\sigma^2}\right] \tag{12}$$

where:

- $\sigma = \mathrm{FWHM}/\sqrt{8\ln 2}$ and β are the beam size and wobbling amplitude respectively. They are obtained from our analysis of the Moon transiting the instrument beam as described in section 3.3.2.
- ζ is a phase constant required to project the sky signal onto the in-phase component for each demodulation. This phase can only be obtained from observations of a strong point source, in our case the Moon. For each channel and demodulation we have different values for ζ and this is because the delays introduced by the electronic components.

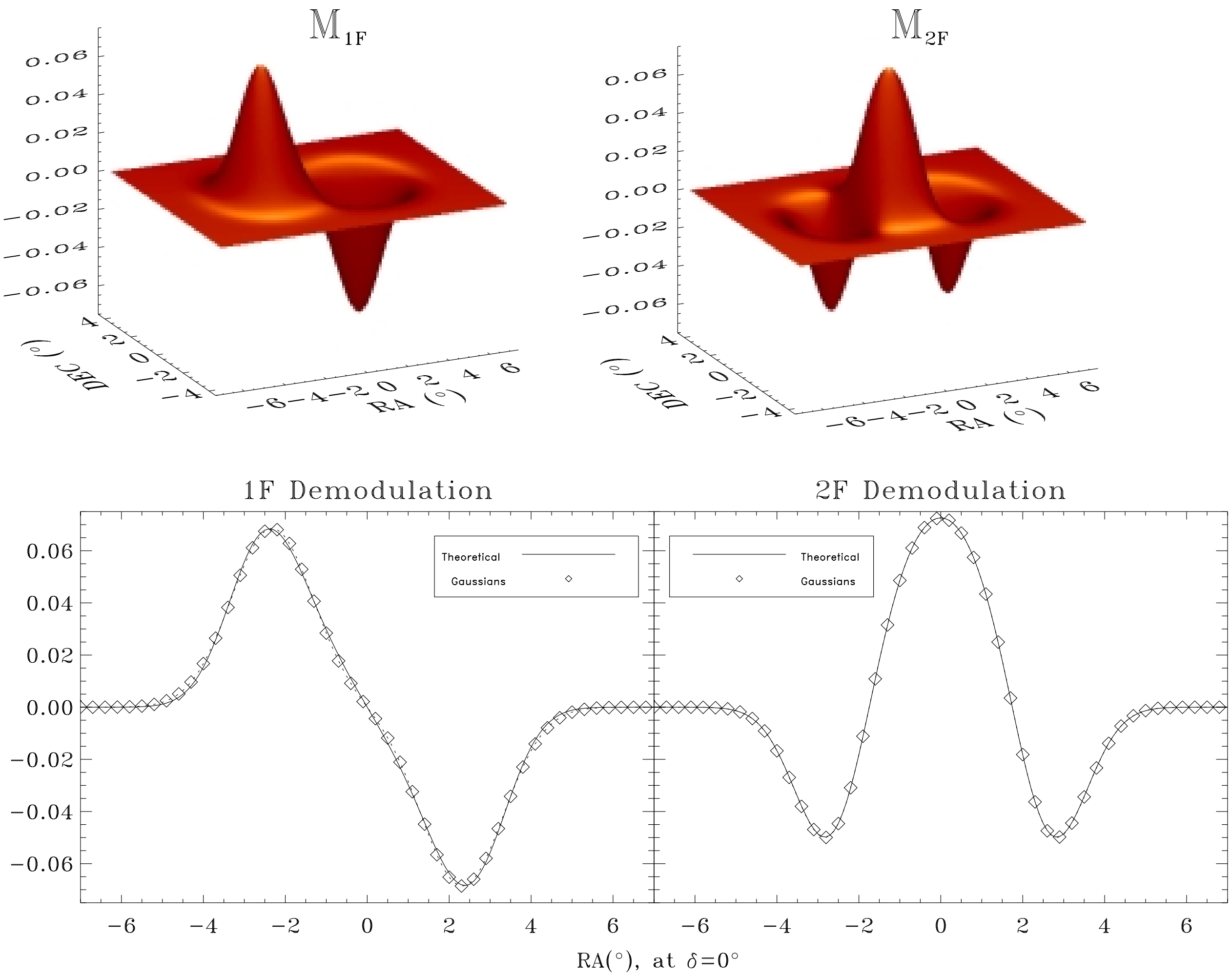

Figure 5: Mapping Functions and fits to them in terms of asymmetric Gaussians.

- N_n is a normalization constant of the window function for the n demodulation (see below).
- $\Delta(t)$ is the angular distance between the point of coordinates (α, δ) and the center of the beam at time t within the period of mirror's movement: $(\alpha', \delta') = (\alpha_0 + \beta_0/\cos(\delta_0) \times \sin(2\pi f_w t + \epsilon), \delta_0)$

$$\cos[\Delta(t)] = \cos\delta' \, \cos\delta_0 \, \cos[\alpha' - \beta_0/\cos(\delta_0)\sin(2\pi t/T)] + \sin\delta' \, \sin\delta_0$$

The response of the 1F and 2F demodulations resembles the usual 2-beam and 3-beam responses to the transit of a point-like source through the beam. In figure 5, upper panels illustrate the bidimensional mapping functions for both demodulations. The 1F demodulated data are well fitted by a 2-beam response with asymmetric Gaussians with $\sigma_\alpha = 1.03°$ in the RA direction and $\sigma_\delta = 0.86°$ in the declination direction, and with a beam throw of $\beta_0 = 2.38°$. The 2F demodulated data are fitted by a 3-beam response with $\sigma_\alpha = 1.56°$, $\sigma_\delta = 0.86°$ for the positive lobe, and $\sigma_\alpha = 0.89°$, $\sigma_\delta = 0.86°$ for the negative lobes and a beam throw of $\beta_0 = 2.40°$. Additionally, these fits must be multiplied by the factors $\aleph_{1F} = 0.362$ and $\aleph_{2F} = 0.593$ to yield the normalizations to the actual response functions for 1F and 2F respectively. Figure 5 also shows the fits by linear combination of elliptical Gaussians to the theoretical mapping function corresponding to the 1F and 2F each demodulations. These approximations greatly simplify the statistical analyses as discussed in chapter 8.

2.2.2 Window Function of the Experiment

In terms of the multipole expansion, the finite size of the experimental beam is equivalent to convolving the Auto-Correlation Function (ACF) with a low pass filter which efficiently cancels out the multipole terms $\ell > \sigma^{-1}$. In addition, the switching and posterior demodulation to the 1F and 2F response causes the suppression of low multipoles. The response of a give instrument to different angular scales (represented in terms of the corresponding multipole moment ℓ) is completely specified by the window function. The decomposition in Legendre polynomials of the ACF as measured by a given experiment is related to the intrinsic ACF and window function. Indeed, this can be easily understood as the generalization of the convolution theorem on a sphere.

$$< \tilde{T}(\alpha_1, \delta_1)\tilde{T}(\alpha_2, \delta_2) >= \frac{1}{4\pi}\sum_{l=1}^{\infty}(2l+1)C_l W_l(\alpha_1, \delta_1, \alpha_2, \delta_2)$$

In fact, the above relation is valid as long as one is willing to make the assumption that CMB anisotropy is a realization of a homogeneous and isotropic random field[1]. In these circumstances the actual positions are of no relevance and only the angular separations must be taken into account . Accordingly it suffices to give W_l only as a function of ψ, the angular separation between (α_1, δ_1) and (α_2, δ_2). As shown by [147], in the case of constant declination scan, the window function for the product of two temperature measurements separated an angle ψ and for the n harmonic demodulation is:

$$W_\ell(\psi)_{nF} \;=\; N_n^2\, B_\ell^2(\sigma) \sum_{r=0}^{\ell} \frac{(2\ell-2r)!(2r)!}{[2^\ell r!(\ell-r)!]^2}\, J_n^2[(\ell-2r)\beta_0]\, \cos[(\ell-2r)\psi]\, j_0^2\left[\frac{(\ell-2r)\Delta\Phi}{2}\right] \qquad (13)$$

where:

- B_ℓ refers to the beam profile: $B_\ell(\sigma) = \exp[-\ell(\ell+1)\sigma/2]$.

---

[1] In fact, most CMB models go beyond these assumptions for they also consider CMB anisotropy being a Gaussian random field

- J_n is the n-th order Bessel function of the first kind.
- j_0 is the zeroth-order spherical Bessel function.
- $\Delta\Phi$ is the bin size in radians on the sky. In our final data sets a bin size of 4 minutes in RA has been chosen and taking into account that the anetnna was observing at $\delta = 40°$ then $\Delta\Phi \simeq 1.34 \times 10^{-2}$.

The value of the normalization constant has been obtained using equation (31) in [147] which states that the value N_n is obtained by requiring an output of 1 K when the input signal corresponds to an extended source of 1 K filling the whole positive lobe. Denoting by D the region along the x-axis (azimuth or RA axis) where the mapping function is positive:

$$1 = \frac{N_n}{2\sigma\sqrt{2\pi}} \int_D \int_{-\pi}^{\pi} dx\, dr\, \cos(nr) \exp\left[-\frac{(x-\alpha\sin r)^2}{2\sigma^2}\right]$$

It is expected that the value of $W_\ell(\psi)$ does not decay rapidly with the value of ψ so in the literature we only find plots ℓ versus W_ℓ for $\psi = 0$.[2] In figure 6 we have plotted the window functions for each channel and demodulation (different colors) together with the corresponding curves when we assume the averaged values from 1F data[3] (thick black curves). As seen in table 7 the values of the wobbling amplitude are consistent between channels and demodulation. For the σ values this does not occur as we observe a monotonic decrease in the σ and a simple χ^2-test yields no consistency between the different values from each channel. In any case, we can see both in the figure and in table 5 that the slight changes in σ and β have little effect on the final values of W_l so given the low S/N ratio in our data we do not expect this to be a source of significant error. To avoid confusion between different channels and demodulations, we will assume in the statistical analysis that all channels share the same values of beam width and chopping angle as given by the average values from all channels at 1F demodulation: $\sigma = 0.84°$, $\alpha = 2.83°$. In table 5 we also give the ℓ ranges where the window function has amplitudes larger than $e^{-1/2}$. The central values of such ℓ intervals correspond to the band power average.

---

[2] This may not be the case when the instrument measurement technique cancels W_ℓ between neighboring pixels

[3] We take this because the transit is better defined at 1F

Table 5: ℓ-ranges for Each Demodulation and Normalization Constants N_n

	1F DEMODULATION		2F DEMODULATION	
Channel	$< \ell_{1F} >$	N_{1F}	$< \ell_{2F} >$	N_{2F}
1	33^{+27}_{-15}	1.062	52^{+27}_{-17}	1.622
2	34^{+27}_{-16}	1.053	54^{+27}_{-19}	1.533
3	35^{+27}_{-16}	1.049	54^{+27}_{-18}	1.510
4	35^{+27}_{-17}	1.044	55^{+28}_{-19}	1.440
VALUES ADOPTED	$\mathbf{34^{+27}_{-16}}$	**1.051**	$\mathbf{55^{+27}_{-19}}$	**1.448**

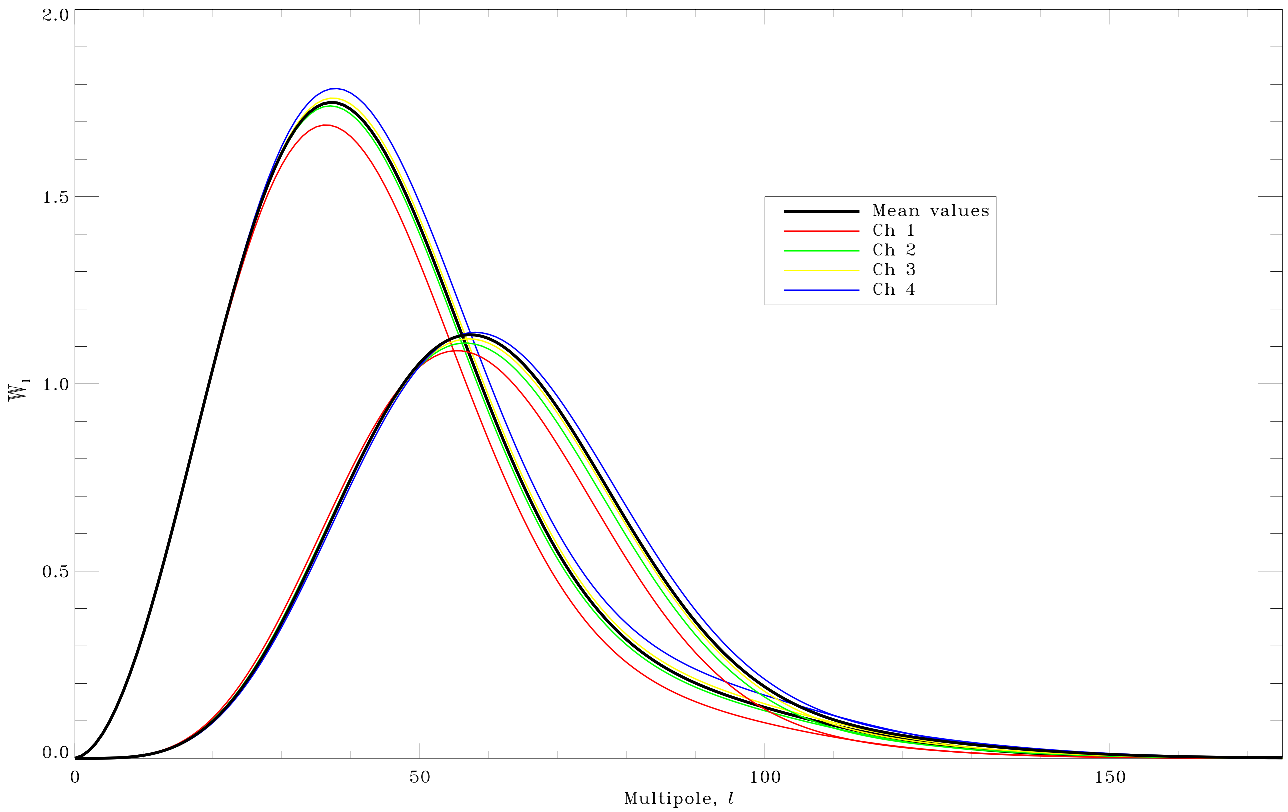

Figure 6: Window Functions for the different channels(see text) at both demodulations and for the assumed values.

Chapter 3

Calibration and Observations

3.1 Laboratory Calibration

Since the instrument will perform differential measurements, the calibration basically consists in calibrating the output of the system when the instrument observes two black body radiators whose temperature difference is known. Because the instrument is intended to measure anisotropies on a black body at ~ 2.7 K, we would like to use black body radiators with temperatures close to this value. However this is not possible given the lack of stable sources at 2.7 K. Then we use radiators at 77 K (Liquid Nitrogen) and 90 K (Liquid Oxygen).

Table 6: Laboratory Calibration Factors

	RJ cal (μV/mK)	RJ to CMB factor	CMB cal (μV/mK)	Error (%)
Ch 1	5.73	1.288	4.45	5.9
Ch 2	25.6	1.66	15.4	1.5
Ch 3	43.6	3.66	11.9	5.3
Ch 4	62.2	4.82	12.9	7.6

Laboratory calibrations were performed by placing blackbody radiators at different temperatures in front of the optical window. By means of an off-axis mirror the optics within the cryostat is redirected towards a vessel containing eccosorb and divided in four sections. Two sections were filled with liquid Nitrogen alternately placed between the other two sections which were filled with liquid Oxygen. A measurement of the pressure at which these two liquids evaporate gives a precise measurement of the temperature. Then the container is rotated at 2 revolutions per second so the detectors see two black bodies of known temperatures. The calibration factors together with their uncertainties are shown in table 6. Since we are concerned with the possibility of systematic effects in the laboratory calibration process we use an additional calibration based of our observations of the Moon (see below).

The presence of the Rayleigh-Jeans to CMB conversion factor is due to the fact that the calibration is done with black body radiators with temperatures such that at the observing frequencies are well within the Rayleigh-Jeans regime, while these frequencies encompass the peak of a black body with $T \sim 2.7$ K.

3.2 Maintenance Tasks: Cooling Down the Cryostat

The only maintenance task performed during the campaign concerned the cooling of the cryostat and its permanent supervision to avoid it warmed up. The first stage in the cooling process is to pump down the cryostat in order to reach a high degree of vacuum. This is needed to ensure that heat transfer by convection is not to occur, so pumping down is performed while we are cooling down the system. The pumping requires in turn three steps:

1. Mechanical pumping involving expansion and contraction.
2. Diffusion pumping once mechanical pumping is inefficient. Then molecules are apart from each other and they are eliminated by being trapped by oil bubbles which can be easily removed from the system.
3. At low temperatures, neither of the two methods described above is efficient anymore. Further molecules can be eliminated from the system by using a cold trap: molecules at low temperature have a very low kinetic energy and can be easily trapped by a porous surface. In our case we use charcoal which is extremely folded so it exhibits a large surface. In this stage we require very low temperatures so we use liquid Nitrogen (LN)

Now the compartment containing the bolometers has achieved a high degree of vacuum so we can cool it down to its working temperature:

1. We reduce the temperature of the bolometer chamber below the fusion T of Nitrogen. To do so we fill the cryostat with Liquid Nitrogen (LN) so we reach $T \sim 70K$
2. We get rid off the LN in the Helium tank (see figure 3) by turning on small resistors which boil off any leftover of the LN from the previous step. Then the helium tank is filled with Liquid Helium (LHe) cooling down the Helium tank to $T \sim 4K$.
3. To reach the working temperature at $\sim 0.35K$ we open the zeolite valve (see figure 3) so the ^{3}He expands by being absorbed by the zeolite and this cools down the bolometer chamber.

The pumping down procedure is only needed once at the beginning of the campaign and care had to be taken to avoid loose the vacuum. The cooling procedure starting from step 1 had to be done once every three days, while LHe refilling occurred at least once a day. To ensure the radiation shield was working, permanent track of the LN level in the LN tank was needed.

3.3 Observations

The experiment operated from June 16th until August 8th 1994 at Observatorio del Teide (Tenerife, Spain), collecting about 550 hours of data. The choice of this observing place (latitude 28.29° and altitude 2400 m) was motivated by the excellent transparency and stability of the atmosphere as well as by its low content of precipitable water vapor. This is also the location of the Tenerife experiment [54] which has already reported two detections of CMB structures [55],[50]. Overlapping observations with the region seen by the Tenerife experiment could lead to the detection of features spanning over a broad range of frequencies. Unfortunately, the sensitivity achieved during this campaign does not allow such joint analysis given the much better S/N ratio of the Tenerife data and the relatively small overlapping region of the sky. Additionally, the different experimental configurations and measurement techniques make difficult to combine both data sets.

The bulk of the observations concentrated on CMB observations at $\delta = 40°$ by fixing the antenna relative to the ground and pointing towards elevation $h = 78°.7$ and azimuth $az = 180°$ (i.e looking at the local meridian towards the North). Some time was also devoted to the observation of the Moon (for calibration purposes), Jupiter (in an unsuccessful attempt to detect an excess of millimetric emission during the collision of the Levy-Schomaker comet) and several Gamma Ray Burst transits (also unsuccessful).

3.3.1 CMB Observations

They constitute the goal of this experiment and therefore they constitute they bulk of the data collected with this instrument. The data were always collected after the Sun was below the horizon and stopped by 10 UT of the following day. In this way we avoid Solar contamination in the data. Likewise, the angular separation between the Moon and the beam was always larger than 23.5° giving confidence on the absence of any Lunar contamination in our data. An example of a typical night of observation for the data in both demodulations in shown in figure 18. The details of the analysis of these data are presented in chapter 7. In addition to the data presented and analyzed in this thesis, an improved version of the same intrument repeated measurements from the same observing place and looking at the same region of the sky during May and June 1996. Works on the data analysis of the data collected during the 1996 campaign are in progress at the moment of writing this work.

3.3.2 Moon Observations

Moon observations were performed in order to check laboratory calibrations and to obtain the phase constants for a proper demodulation of the data. In all cases the observations consisted in

Table 7: Results From Fits To Extended Moon Transits

	1F DEMODULATION		2F DEMODULATION	
	σ (°)	α (°)	σ (°)	α (°)
Ch 1	0.91 ± 0.03	2.81 ± 0.03	0.96 ± 0.03	2.74 ± 0.03
Ch 2	0.854 ± 0.028	2.83 ± 0.03	0.898 ± 0.027	2.770 ± 0.028
Ch 3	0.826 ± 0.027	2.827 ± 0.027	0.876 ± 0.024	2.772 ± 0.024
Ch 4	0.795 ± 0.027	2.835 ± 0.025	0.822 ± 0.023	2.800 ± 0.022

fixing the telescope in azimuth at $az = 0°$ and elevation attained by the Moon at the moment it is transiting the Meridian, and letting the Moon drift across the instrumental beam. Three observations of the Moon were performed in this way on June 24th, July 23th and July 30th. Only the Moon on June 24th was taken in full Moon phase so this is the one we have used in the following analysis. Ideally the observation of an astronomical source with a know flux as the Moon should be useful to obtain an astronomical calibration. Such astronomical calibration should then be given more confidence than the calibration in the lab since we are performing a calibration in the same conditions than the actual observations. In principle, by fitting the observed Moon to the theoretical Moon response we can estimate the beam width chopping angle in addition to the sought calibration constants. Unfortunately, there is a degeneracy for the couple of parameters offset in elevation (o_{el}) and Moon Temperature (T_M) . This degeneracy can partially be broken if we have a raster scan of the Moon and not an observation of the Moon at a single elevation as in our case. In any case, assuming the laboratory calibration we obtain estimates for the absolute value of the offset in elevation: $|o_{el}| = 1.1° \pm 0.1°$. This is done by comparing the output value of T_M of our simulation (see below) with the predicted value for the Moon brightness temperature at channel 1 on June 24th 1994 from the Lunar model in [8]. This lunar model provides the disk-averaged brightness temperature at a given phase angle with a nominal uncertainty less than 5%. In the simulation we have also considered the proper motion of the Moon during the observation with the program Horizons (JPL, [59]) and realistic values for the atmospheric opacity at our frequencies by using balloon measurements of the integrated water vapor.

The model we use assumes a Gaussian beam characterized by a width σ sinusoidally wobbled in azimuth with amplitude α. We must also considered the possibility of having an offset in elevation o_{az} and azimuth o_{el} of the antenna so that the Moon may not be transiting through the center of the beam. Finally we have also taken into account that a slight deviation from the vertical of the wobbling axis would result in a chopping movement in elevation characterized by some amplitude β and with the same angular frequency as the chopping in azimuth. The details together with the mathematical expressions arising from this model are given in Appendix B.

In tables 8 and 9 the results for the most relevant parameters, namely σ and α, are presented . It can be seen that for each channel the estimates on σ and α are consistent and they are rather insensitive to the actual value of o_{el}. Since a priori no value of o_{el} is preferred, we assign to σ and

α the weighted average of the corresponding values in tables 8 and 9, while the assigned error bars are computed as the non-weighted averages of the corresponding error bars. The values for each channel and demodulation are given in table 7. The results on β (chopping amplitude in elevation) strongly depend on the o_{el} assumed, but in all cases its absolute value is smaller than 1°. If we are willing to assume $o_{el} = \pm 1.1^\circ$ then we have $|\beta| < 0.09^\circ$. In figure 7 we show one of these fits for the case $o_{el} = 1.1$ for both demodulations.

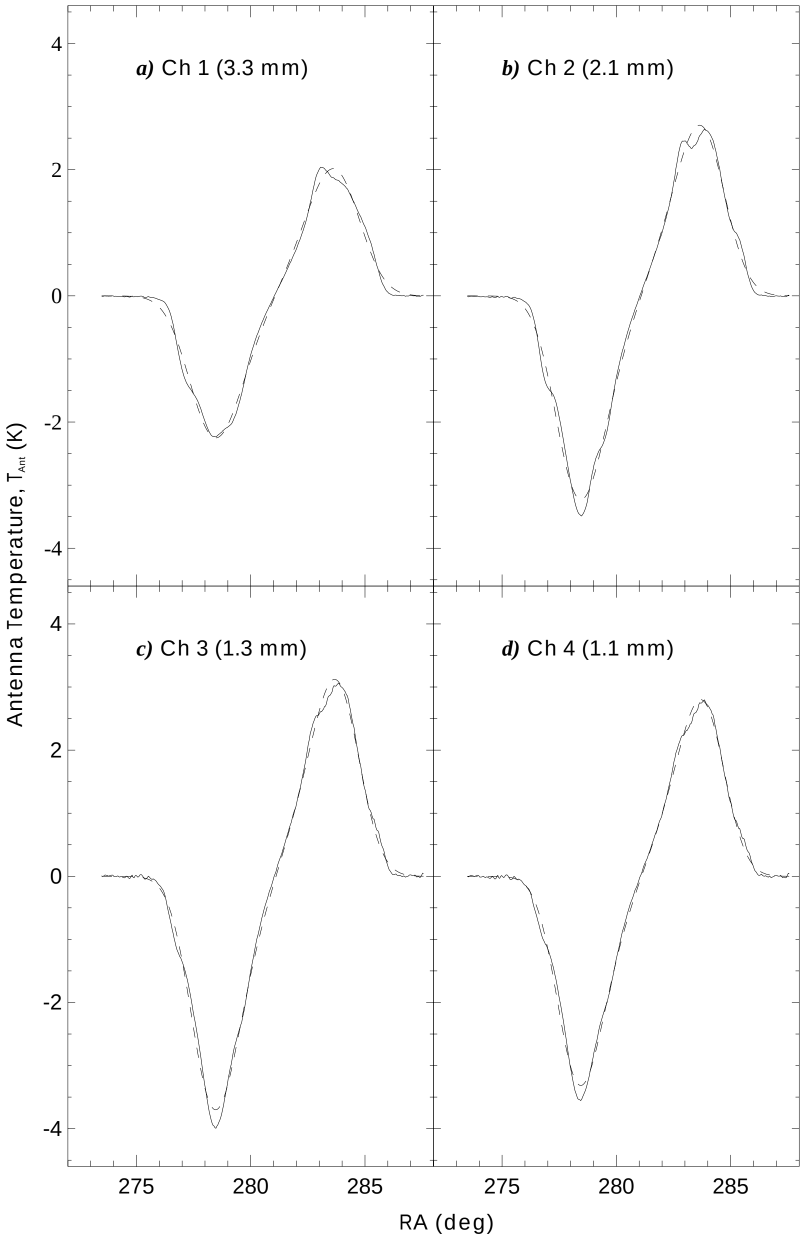

Figure 7: Fit (dashed line) to the observed Moon transit (solid). The offset in elevation assumed is 1.1°.

Table 8: Fits To Extended Moon Transits at 1F.

	CHANNEL 1		CHANNEL 2	
o_{el} (°)	σ (°)	α (°)	σ (°)	α (°)
-1.40	0.906 ± 2.9e-02	2.782 ± 2.6e-02	0.850 ± 2.7e-02	2.796 ± 2.4e-02
-1.20	0.907 ± 2.9e-02	2.786 ± 2.6e-02	0.851 ± 2.7e-02	2.800 ± 2.4e-02
-1.00	0.908 ± 3.0e-02	2.790 ± 2.6e-02	0.852 ± 2.7e-02	2.804 ± 2.4e-02
-0.80	0.909 ± 3.0e-02	2.794 ± 2.6e-02	0.853 ± 2.7e-02	2.808 ± 2.4e-02
-0.60	0.910 ± 3.0e-02	2.798 ± 2.6e-02	0.854 ± 2.7e-02	2.813 ± 2.4e-02
-0.40	0.911 ± 3.0e-02	2.803 ± 2.6e-02	0.854 ± 2.7e-02	2.819 ± 2.5e-02
-0.20	0.910 ± 3.0e-02	2.812 ± 2.7e-02	0.850 ± 2.7e-02	2.835 ± 2.5e-02
0.00	0.856 ± 5.9e-02	2.952 ± 1.1e-01	0.780 ± 5.2e-02	2.989 ± 8.3e-02
0.20	0.911 ± 3.0e-02	2.820 ± 2.7e-02	0.848 ± 2.7e-02	2.847 ± 2.6e-02
0.40	0.915 ± 3.0e-02	2.816 ± 2.6e-02	0.858 ± 2.7e-02	2.832 ± 2.5e-02
0.60	0.917 ± 3.0e-02	2.818 ± 2.6e-02	0.860 ± 2.8e-02	2.832 ± 2.5e-02
0.80	0.918 ± 3.0e-02	2.821 ± 2.6e-02	0.862 ± 2.8e-02	2.835 ± 2.5e-02
1.00	0.919 ± 3.0e-02	2.824 ± 2.7e-02	0.863 ± 2.8e-02	2.838 ± 2.5e-02
1.20	0.921 ± 3.0e-02	2.827 ± 2.7e-02	0.864 ± 2.8e-02	2.841 ± 2.5e-02
1.40	0.922 ± 3.0e-02	2.831 ± 2.7e-02	0.866 ± 2.8e-02	2.844 ± 2.5e-02
	CHANNEL 3		CHANNEL 4	
-1.40	0.823 ± 2.6e-02	2.798 ± 2.4e-02	0.792 ± 2.6e-02	2.806 ± 2.3e-02
-1.20	0.824 ± 2.6e-02	2.802 ± 2.4e-02	0.793 ± 2.6e-02	2.810 ± 2.3e-02
-1.00	0.825 ± 2.6e-02	2.806 ± 2.4e-02	0.794 ± 2.6e-02	2.814 ± 2.3e-02
-0.80	0.826 ± 2.6e-02	2.810 ± 2.4e-02	0.795 ± 2.6e-02	2.818 ± 2.3e-02
-0.60	0.826 ± 2.6e-02	2.814 ± 2.4e-02	0.795 ± 2.6e-02	2.822 ± 2.3e-02
-0.40	0.827 ± 2.6e-02	2.820 ± 2.4e-02	0.795 ± 2.6e-02	2.828 ± 2.3e-02
-0.20	0.823 ± 2.6e-02	2.834 ± 2.4e-02	0.792 ± 2.6e-02	2.841 ± 2.3e-02
0.00	0.759 ± 4.8e-02	2.969 ± 7.5e-02	0.729 ± 4.5e-02	2.964 ± 6.8e-02
0.20	0.821 ± 2.6e-02	2.845 ± 2.5e-02	0.790 ± 2.6e-02	2.851 ± 2.4e-02
0.40	0.830 ± 2.7e-02	2.833 ± 2.4e-02	0.799 ± 2.6e-02	2.841 ± 2.3e-02
0.60	0.833 ± 2.7e-02	2.834 ± 2.4e-02	0.801 ± 2.6e-02	2.842 ± 2.3e-02
0.80	0.834 ± 2.7e-02	2.837 ± 2.4e-02	0.803 ± 2.6e-02	2.845 ± 2.3e-02
1.00	0.836 ± 2.7e-02	2.840 ± 2.4e-02	0.804 ± 2.6e-02	2.848 ± 2.3e-02
1.20	0.837 ± 2.7e-02	2.843 ± 2.4e-02	0.805 ± 2.6e-02	2.851 ± 2.3e-02
1.40	0.838 ± 2.7e-02	2.846 ± 2.4e-02	0.806 ± 2.6e-02	2.855 ± 2.3e-02

Table 9: Fits To Extended Moon Transits at 2F.

	CHANNEL 1		CHANNEL 2	
o_{el} (°)	σ (°)	α (°)	σ (°)	α (°)
-1.40	0.967 ± 3.2e-02	2.700 ± 3.5e-02	0.885 ± 2.8e-02	2.746 ± 2.8e-02
-1.20	0.967 ± 3.3e-02	2.704 ± 3.6e-02	0.886 ± 2.8e-02	2.750 ± 2.8e-02
-1.00	0.968 ± 3.3e-02	2.708 ± 3.6e-02	0.887 ± 2.8e-02	2.753 ± 2.8e-02
-0.80	0.970 ± 3.3e-02	2.711 ± 3.6e-02	0.888 ± 2.8e-02	2.757 ± 2.8e-02
-0.60	0.971 ± 3.3e-02	2.715 ± 3.6e-02	0.888 ± 2.8e-02	2.761 ± 2.8e-02
-0.40	0.972 ± 3.3e-02	2.719 ± 3.6e-02	0.888 ± 2.8e-02	2.765 ± 2.8e-02
-0.20	0.975 ± 3.3e-02	2.721 ± 3.5e-02	0.886 ± 2.8e-02	2.770 ± 2.8e-02
0.00	0.958 ± 6.6e-04	2.742 ± 2.4e-03	0.907 ± 5.5e-03	2.767 ± 1.6e-02
0.20	0.977 ± 3.3e-02	2.728 ± 3.6e-02	0.888 ± 2.8e-02	2.776 ± 2.8e-02
0.40	0.979 ± 3.3e-02	2.731 ± 3.5e-02	0.892 ± 2.8e-02	2.778 ± 2.8e-02
0.60	0.978 ± 3.3e-02	2.735 ± 3.6e-02	0.895 ± 2.8e-02	2.781 ± 2.8e-02
0.80	0.981 ± 3.3e-02	2.738 ± 3.5e-02	0.897 ± 2.8e-02	2.784 ± 2.9e-02
1.00	0.983 ± 3.3e-02	2.741 ± 3.5e-02	0.898 ± 2.8e-02	2.788 ± 2.9e-02
1.20	0.984 ± 3.3e-02	2.744 ± 3.5e-02	0.900 ± 2.9e-02	2.791 ± 2.9e-02
1.40	0.985 ± 3.3e-02	2.747 ± 3.5e-02	0.901 ± 2.8e-02	2.794 ± 2.8e-02
	CHANNEL 3		CHANNEL 4	
-1.40	0.844 ± 2.5e-02	2.763 ± 2.5e-02	0.807 ± 2.4e-02	2.775 ± 2.3e-02
-1.20	0.845 ± 2.5e-02	2.767 ± 2.5e-02	0.809 ± 2.4e-02	2.779 ± 2.3e-02
-1.00	0.846 ± 2.5e-02	2.771 ± 2.5e-02	0.810 ± 2.4e-02	2.783 ± 2.3e-02
-0.80	0.847 ± 2.5e-02	2.775 ± 2.5e-02	0.810 ± 2.4e-02	2.787 ± 2.3e-02
-0.60	0.847 ± 2.5e-02	2.779 ± 2.5e-02	0.811 ± 2.4e-02	2.790 ± 2.3e-02
-0.40	0.846 ± 2.5e-02	2.783 ± 2.4e-02	0.811 ± 2.4e-02	2.794 ± 2.3e-02
-0.20	0.843 ± 2.5e-02	2.788 ± 2.4e-02	0.810 ± 2.4e-02	2.798 ± 2.3e-02
0.00	0.877 ± 6.3e-04	2.769 ± 2.1e-03	0.824 ± 1.9e-03	2.799 ± 6.1e-03
0.20	0.846 ± 2.6e-02	2.793 ± 2.5e-02	0.812 ± 2.4e-02	2.804 ± 2.3e-02
0.40	0.849 ± 2.5e-02	2.796 ± 2.5e-02	0.816 ± 2.4e-02	2.807 ± 2.3e-02
0.60	0.853 ± 2.5e-02	2.799 ± 2.5e-02	0.818 ± 2.4e-02	2.811 ± 2.3e-02
0.80	0.856 ± 2.6e-02	2.802 ± 2.5e-02	0.819 ± 2.4e-02	2.814 ± 2.3e-02
1.00	0.857 ± 2.6e-02	2.805 ± 2.5e-02	0.821 ± 2.4e-02	2.817 ± 2.3e-02
1.20	0.859 ± 2.6e-02	2.808 ± 2.5e-02	0.822 ± 2.4e-02	2.821 ± 2.3e-02
1.40	0.860 ± 2.6e-02	2.812 ± 2.5e-02	0.823 ± 2.4e-02	2.824 ± 2.3e-02

Table 10: Upper Limits To NET (mK $s^{1/2}$) In Thermodynamic Units

	1F DEMODULATION		2F DEMODULATION	
	IN-PHASE	OUT-PHASE	IN-PHASE	OUT-PHASE
Ch 1	3.5	3.2	3.3	2.8
Ch 2	2.7	1.0	1.1	0.8
Ch 3	4.8	1.8	2.5	1.5
Ch 4	5.3	1.4	4.1	1.0

3.4 Estimates of the Instrument Noise Levels

As we will see in chapter 4, one of the effects of atmospheric emission is a big increase of the noise in each night of observation with respect to the instrument noise levels. The aim of this section is to obtain the best possible estimates for the instrument noise levels. In order to do so we will rely on the assumption that at a high enough frequency the instrument noise is **white noise**. Therefore if all the noise in our data is due to the instrument we should observe a flat power spectra. Assume an uncorrelated stationary random series (i.e. white noise) exhibiting a variance $\sigma^2_{\Delta t}$ when the sampling time is Δt. The spectral power density of such a process is [142]:

$$S(\nu) = \sigma^2_{\Delta t}\Delta t \tag{14}$$

This gives an alternate method to estimate the value of $\sigma^2_{\Delta t}$ rather than computing the *rms* of such process[1]. The reader may think this method is reluctant for computing *rms* values is far more straightforward that computing $S(\nu)$. The usefulness of this method is that it is more general than the *rms* allowing good estimators of $\sigma^2_{\Delta t}$ even in some situations when the series exhibits white noise characteristic only above a given frequency (i.e $S(\nu)$ becomes flat for $\nu \geq \nu_0$). Indeed this is our case: our data are a combination of instrument noise, atmospheric noise and astronomical signal, the latter to be ignored given its weakness in each night of observation. In figure 8 we show the noise spectra in thermodynamic temperature for all channels and both demodulations for a typical night of observation. We notice that at low frequencies it quite departs form white noise: neither the instrument noise nor the atmospheric noise exhibit flat spectra at low ν. Bolometers show a characteristic $1/f$ spectrum while atmospheric fluctuations have a more complicated spectrum and in general follow a $1/f^k$ spectrum with k variable. On the other hand, the spectra of both contributions flatten at high frequencies, becoming indistinguishable from each other. At high frequencies the power spectra are flat, and assigning to the instrument noise the value corresponding to such noise floor is a huge overestimation.

In theory, this problem could be solved by using the out-phase component produced during the

---

[1] In the case of white noise both methods give identical results, so one would use the *rms* value rather than $S(\nu)$

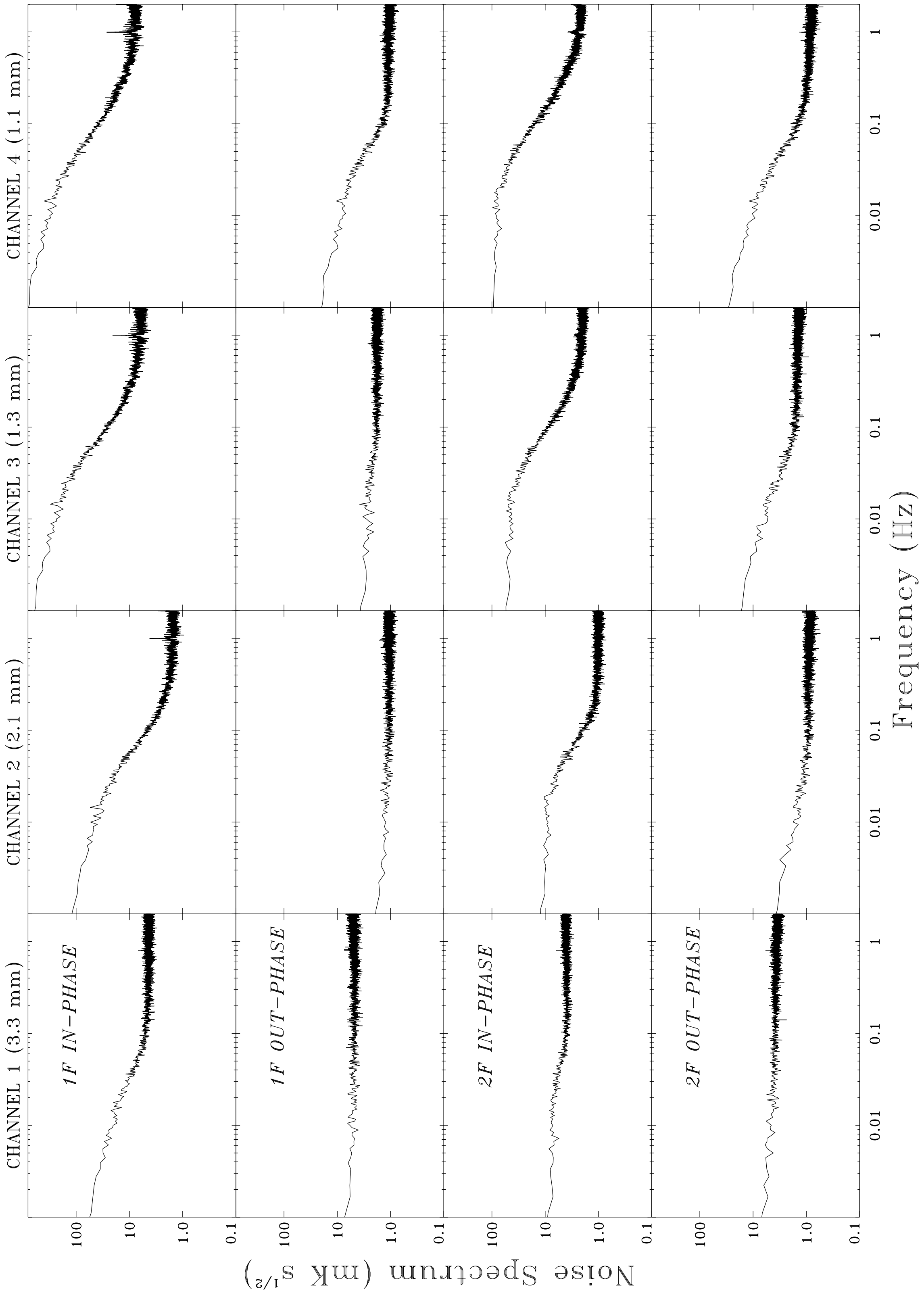

Figure 8: Noise spectra for all channels, both demodulations and both components. We can see how the noise spectra approach at high frequencies the expected white noise behavior.

demodulation because it is expected to contain only instrumental noise. In practice, even in the out-phase component there are still residual amounts of atmospheric noise[2]. From figure 8we see that channel 1 exhibits power spectra almost flat in the out-phase spectra for 1F and 2F demodulations, indicating that most of the noise in channel 1 at high frequencies is due to instrument noise. The out-phase components for the rest of the channels still contains considerable amounts of atmospheric noise as indicated by the similar shapes of the spectra in the in- and out-phase components. This interpretation is strongly supported by the fact that the spectral shape at low frequencies, and the noise floor at high frequencies, change from day to day. The higher values for the instrumental noise as obtained from the analysis of the out-phase components of the the 1F data indicate the greater ability of the 2F demodulation in removing linear gradients caused by atmospheric emission . The final **upper limits** in thermodynamic units assigned to the instrument noise are 2.8, 0.8, 1.5 and 1.0 mK $s^{1/2}$ for channels 1 to 4 obtained as the minimum amplitude of the flat region during the whole campaign of $S(\nu)$ for $\nu \geq \nu_0$ and from the out-phase components of 2F.

---

[2] It is impossible to find a constant demodulation phase which completely sets to zero the sky signal in the out-phase component

Chapter 4

Atmospheric Effects on Our Data

The aim of this section is to describe the effects of atmospheric emission on our data. By comparing the presence of these effects on the data before and after applying the atmospheric technique we will be in position to assess the performance of our technique.

4.1 Increase of Noise

At first sight the influence of atmospheric noise on our data manifests itself as a big increase of the noise with respect to the noise levels expected solely from instrumental noise. To study this effect it is convenient to plot the histograms for the rms values. This has been done in the left panels of figure 9 for both demodulations and all channels, where we plot the histogram of the rms values obtained from the data after being binned to 10 s (see below for justification of this bin size). We obtained a rms value from each 0.1 hour segments of data which contain about 36 points. These rms values were computed only for those portions of the data surviving the different editions leading to portions of data to be cleaned from atmospheric noise (see chapter 6). With this approach, it will be possible toestablish a comparison with the situation before and after applying the atmospheric cleaning. In the right panels we plot the theoretical distribution of rms values obtained as $rms = \sqrt{\sum_{i=1}^{n}(T_i - \bar{T})^2/(n-1)}$ where the T_i's are independent variables drawn from a Gaussian distribution of mean μ_T and variance σ^2: $N(\mu_T, \sigma)$. The pdf[1] of the statistics rms turns out to be closely related to the pdf of a χ^2 with $n-1$ degrees of freedom[2]:

$$f_{rms}(z) = \frac{(n-1)^{\frac{n-1}{2}}}{2^{\frac{n-3}{2}}\,\Gamma\left(\frac{n-1}{2}\right)\,\sigma^{n-1}}\, z^{n-2}\, \exp\left[-\frac{(n-1)z^2}{2\sigma^2}\right] \qquad (15)$$

---

[1] pdf stands for Probability Density Function.

[2] The lost of one degree of freedom is due to our lack of knowledge of the true mean μ_T so we have to use $\bar{T}$ instead

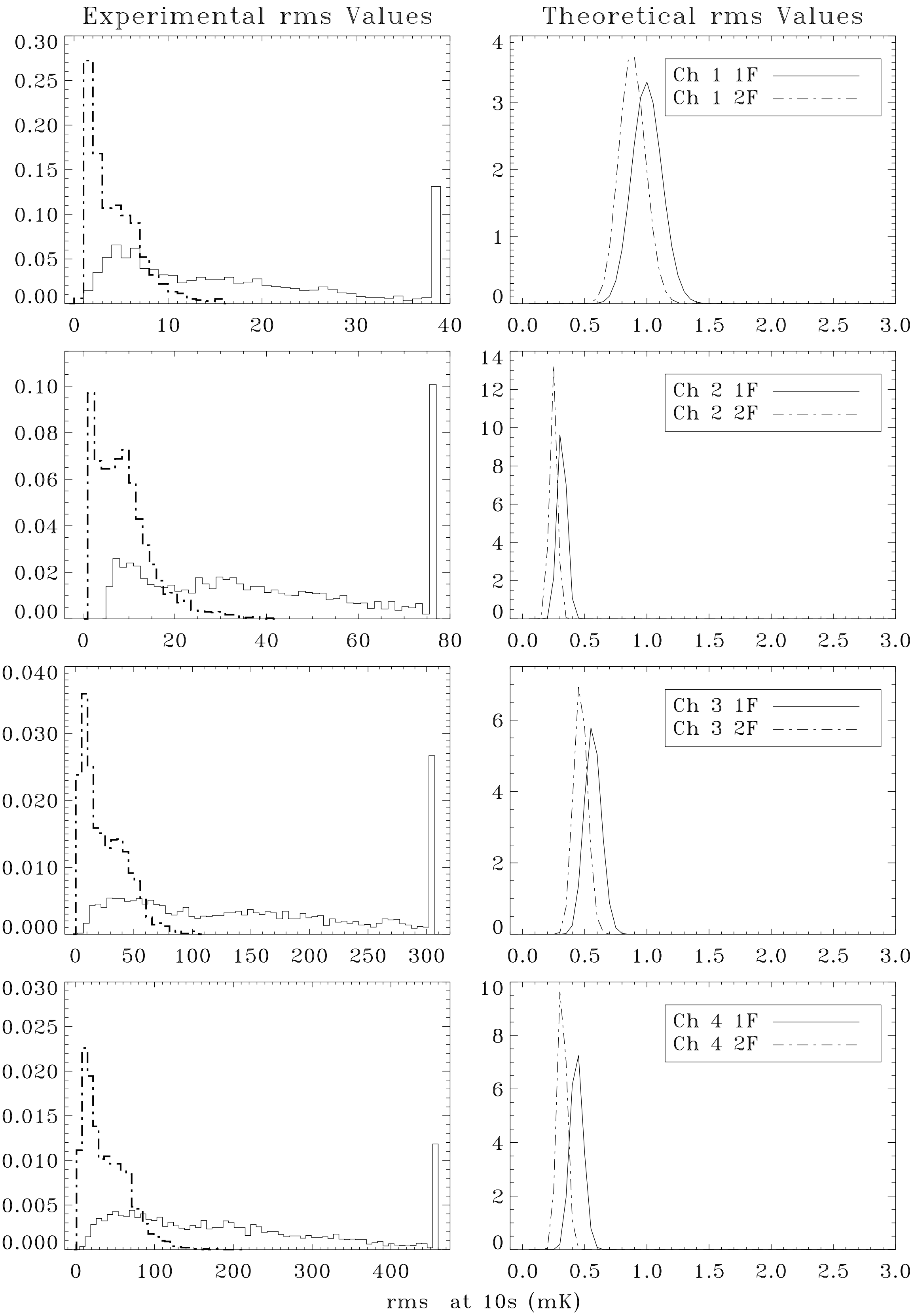

Figure 9: Distribution of the *rms* values for both demodulations and all channels. The *rms* temperatures along the x-axis refer to thermodynamic temperatures. Note the height of the last bin in all histograms due to that it contains the contribution of that bin plus all following bins.

The pdf curves plotted in figure 9 correspond to assuming $n = 36$ and the values of σ listed in table 10 in the OUT-PHASE columns for each demodulation. It is obvious that neither demodulation follows a Gaussian distribution. The experimental distributions are much wider than the theoretical distributions, a clear indication that the noise is much higher that the instrumental noise. The difference in shape between the theoretical and actual *rms* distributions is due not only to the bigger value of σ in the data but also to the fact that the T_i values at 10 *s* are not independent from each other as we will see in the next section. The figure is also telling us about the better rejection of the 2F demodulation to atmospheric noise as the *rms* values for the 2F data are far more clustered than the corresponding *rms* values for the 1F data.

4.2 Auto-Correlations Introduced by Atmospheric Noise

In addition to increasing the noise levels, the atmosphere is introducing correlation between adjacent data points. A first evidence on this is that the noise in our scans does not decrease according to the $1/\sqrt{N}$ law as we increase the number of points (N) in our bins. This can be seen in figure 10 where we have plotted with diamonds the *rms* values for a typical day as obtained from the same night of observation and binned to 0.25, 2, 5, 10, 16, 25, 40, 64, 128 and 240 *s* corresponding to using N = 1, 8, 20, 40, 64, 100, 160, 256, 512 and 960 points respectively. In solid lines we also plot what one would expect if the data points were independent. From this figure we see that for this particular day only channel 1 2F shows an evolution of *rms* with bin size close to what one would expect if the data corresponded to white noise. All other channels show a huge divergence from this behavior. In general the above behavior for channel 1 2F only happened on very good days in terms of atmospheric noise, while it never happened for any of the other channels at any demodulation.

The presence of non-zero correlation between adjacent data points has tremendous implications on the way we estimate our error bars. Indeed, when the data points are correlated the error bar associated to the mean of N points is not any more $\sigma/\sqrt{N}$, where σ is the standard deviation of the N points, but we have to use:

$$\sigma_{\bar{x}} = \frac{\sigma}{\sqrt{N}} \sqrt{1 + \frac{2}{N} \sum_{i=1}^{N} \sum_{j=i+1}^{N} \rho(\tau_{ij})} \tag{16}$$

obtained from [35] and further assuming that the time series is a stationary process so that the autocorrelation function only depends on the distance τ_{ij} between points i and j. To evaluate the autocorrelation function for each night of observation we make use of the Wiener-Khinchin relations (see e.g. [7] or [142]):

$$S_f(\nu) = \int_{\infty}^{\infty} d\tau \, B_f(\tau) \, e^{-i\,2\pi\,\nu\,\tau} \tag{17}$$

$$B_f(\tau) \;=\; \int_{\infty}^{\infty} d\nu\, S_f(\nu)\, e^{i\,2\pi\,\nu\,\tau} \tag{18}$$

where $B_f(\tau)$ is the auto-covariance function of the stationary process $f(t)$ and is defined and related to the autocorrelation function $\rho_f(\tau)$ according to:

$$\begin{aligned} B_f(\tau) &\equiv E[(f(t+\tau)-\mu_f)(f(t)-\mu_f)] \\ \rho_f(\tau) &\equiv \frac{B_f(\tau)}{\sigma^2} \end{aligned}$$

and μ_f is the mean of the stationary process $f(t)$, and $E[\,]$ the expectation operator. On the other side, the power spectral density S_f is defined as:

$$S_f(\nu) = \lim_{T\to\infty} \mathrm{E}\left[\frac{|F_T(\nu)|^2}{2T}\right]$$

$2\,T$ is the size of the window function applied in the time domain and $F_T(\nu) = \int_{-T}^{+T} dt\, f(t)\, e^{-i\,2\pi\,\nu\,t}$ is the truncated Fourier transform. The power spectrum estimator obtained by squaring the absolute value of the result of an FFT routine is called periodogram and it exhibits a very small efficiency: it has a 100% standard deviation. A better estimator[3] can be obtained by averaging M independent periodograms so that the variance is reduced by a factor $1/M$. This procedure is known as Bartlett's Procedure ([92]). A smaller spectral variance per data point can be further obtained by slightly modifying the Bartlett's approach: the segments are not completely independent but they overlap each other by half their length. In this way, if previously we had M independent segments, we now have $K = 2M - 1$ overlapping segments and the estimator variance is reduced by a factor $9K/11$, where the factor $9/11$ is due to the segments not being statistically independent [102]. Once we have obtained estimates for the power spectrum we simply use equation 18 and divide by $\sigma^2 = B_f(0)$ to obtain the auto-correlation function[4] $\rho_f(\tau)$ for the stationary[5] process f.

In figure 11 we have plotted the averaged auto-correlation functions, $\rho(\tau)$ in equation 15, for all channels and both demodulations. These curves have been obtained by averaging the auto-correlation curves from all scans contributing to the final data sets in each case. For a given lag we observe that the auto-correlation function is always larger in the high frequency channels when comparing within the same demodulation. Likewise, for the same channel we always observe a

---

[3] In the sense of having a smaller variance

[4] It is worthy remarking that in doing the FFT's to obtain the periodograms we have subtracted the mean value of the FFT'ed segment. Otherwise, we would observe a very high value of $\rho_f(\tau)$ at all τ due to the presence of a common offset

[5] The requirement of stationary is a crucial one in all of this treatment. This is somehow guaranteed by using the edited data where noisy sections have been eliminated and we have kept data with more or less the same levels of noise

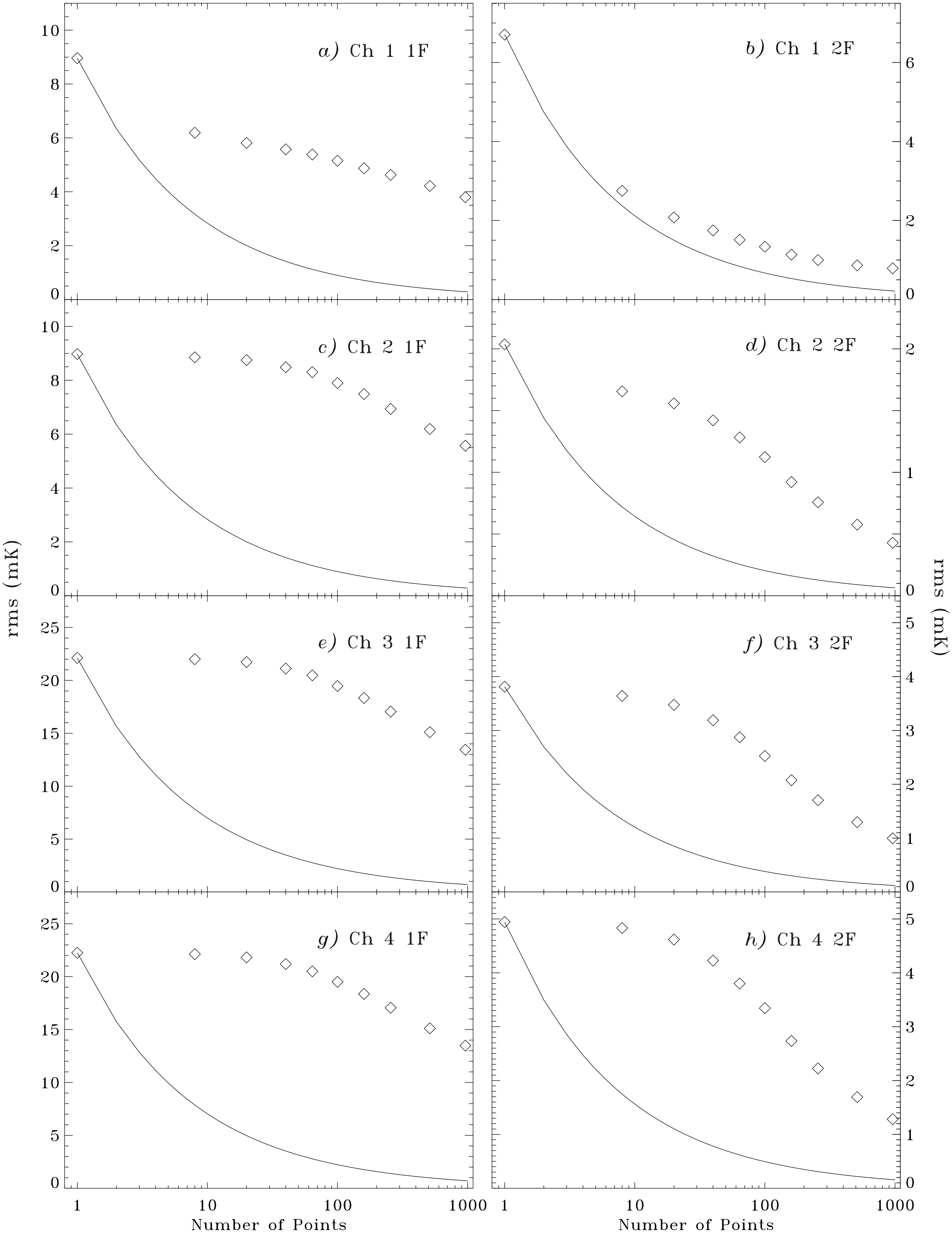

Figure 10: Evolution of *rms* values with number of points for both demodulations and all channels on a typical day. Diamonds are the *rms* values obtained from the data at different bin sizes (i.e using different number of points), and the solid line is the evolution one would see if the data points were independent.The *rms* values on the y-axis refer to antenna temperatures.

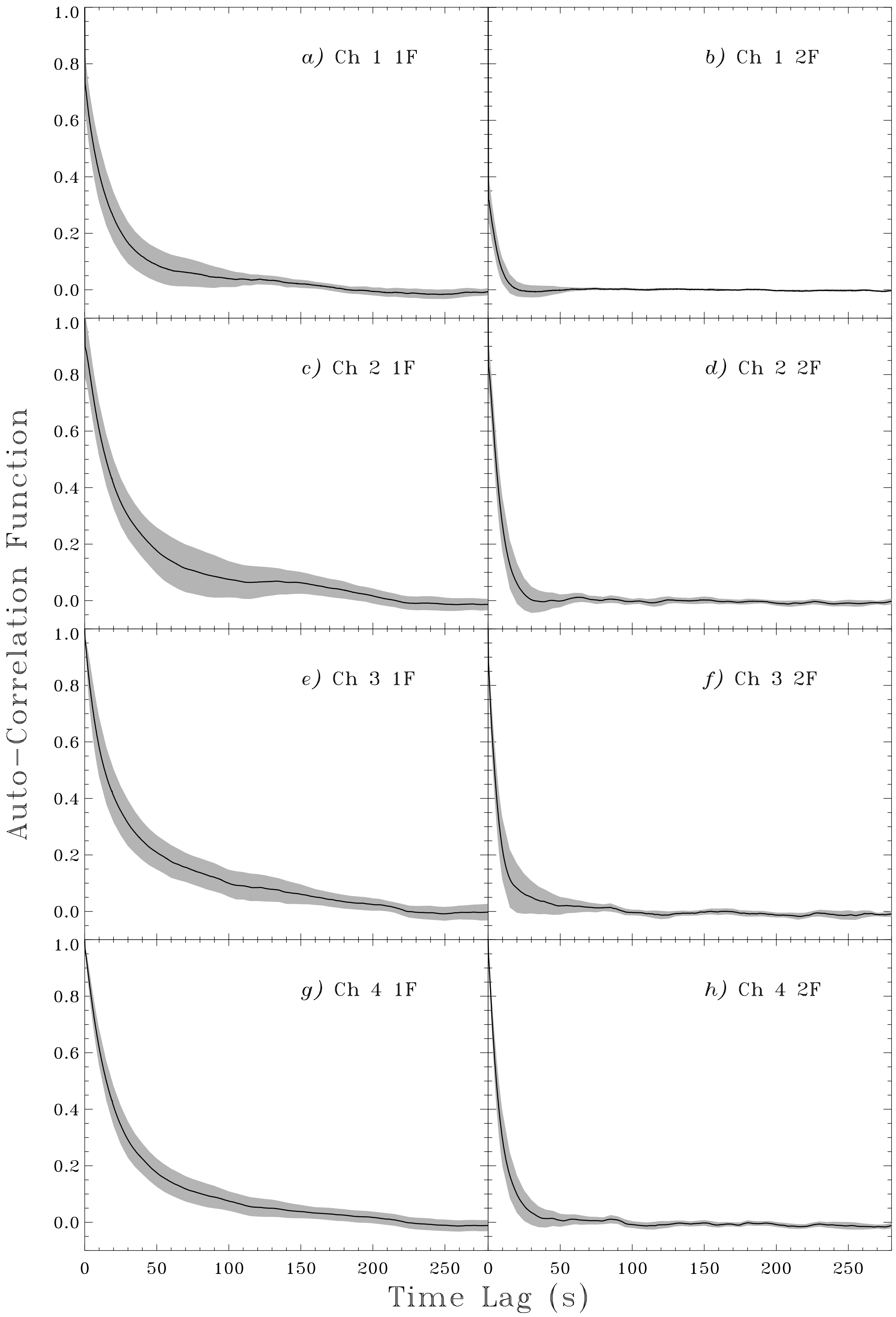

Figure 11: Mean auto-correlation curves for each demodulation and channel obtained from the average of the auto-correlation curves from each of the observing nights used to generate the final data sets (see chapter 6). The shaded regions correspond to $\pm 2\sigma$.

larger coherence time for the 1F demodulation than for the 2F demodulation. This is understood as the 2F demodulation being able to reject atmospheric noise with a higher efficiency than the 1F technique. Another important conclusion from figure 11 is the necessity to use bins large enough such that correlations between adjacent bins are reduced. In this way we will ensure that standard deviations are properly computed and assigned as error bars in the subsequent cleaning process.

4.3 Correlation Between Channels

This is the key point which allows us to attribute the observed excess of correlated noise to atmospheric origin. We measure extremely high correlations between the time-variable signals seen by all channels within the same night of observation as shown in table 11. These correlations are lost however when comparing the signals taken at different nights. This point discards the observed signals being due to astronomical sources while the fact of high correlation between channels can not be attributed to correlated detector noise between channels. This fact will be exploited subsequently as the cornerstone for our analysis to reduce atmospheric noise. In table 11 we give the mean correlation between channel i ($i = 1, 2, 3$) and channel 4 for all the data surviving the first edition (see chapter 6, section 6.2) for the fraction of the data selected to build the final data sets. Because atmospheric emission increases with frequency, we expect a higher correlation in the high frequency channels as we observe in this table. Likewise, the higher ability of the 2F demodulation to eliminate atmospheric gradients explains why we observe higher correlations in the 1F data.

Table 11: Correlation Between Channels Before Applying Atmospheric Correction.

	1F DEMODULATION		2F DEMODULATION	
	Whole Campaign	Final Data Set	Whole Campaign	Final Data Set
Ch 1 - Ch 4	0.965 ± 0.010	0.990 ± 0.010	0.884 ± 0.023	0.91 ± 0.09
Ch 2 - Ch 4	0.983 ± 0.008	0.995 ± 0.011	0.977 ± 0.007	0.991 ± 0.010
Ch 3 - Ch 4	0.99963 ± 0.00010	0.99984 ± 0.00010	0.9956 ± 0.0011	0.995 ± 0.010

Chapter 5

Galactic and Extragalactic Foregrounds

5.1 Introduction

Observations of CMB are conducted principally at centimetric and millimetric wavelengths where the 2.7 K radiation is by far the dominant contribution to the microwave and millimetric sky (see figure 12). Yet, we are interested in the level of CMB anisotropy and given its low value ($\Delta T/T \sim 10^{-5} - 10^{-6}$) we are concerned about the possibility of other radiation fields of much lower total brightness exhibit the same levels of anisotropy than those from CMB. An exhaustive list of these "contaminant" radiation fields[1] can be found in [4]. It turns out to be convenient to separate them into Galactic Foregrounds and Extragalactic Foregrounds. This distinction is mainly motivated by the angular scales at which they are of concern:

Extragalactic Foregrounds Most of them become relatively important only at small angular scales. These foregrounds include fluctuations due to synchrotron and dust emission in both resolved and unresolved sources, emission from dust in the intracluster medium (S-Z effect) and emission by radio sources (radio galaxies).

Galactic Foregrounds In this category we include the diffuse contribution due to synchrotron, free-free and dust emission from the Galaxy. These foregrounds are relevant at all angular scales although its importance decreases as the angular scale decreases.

Future satellite missions (MAP and Planck) are expected to produce data with high S/N ratios so its crucial to devise methods able to separate CMB anisotropy from the different foreground fluctuations. Until very recently, these methods relied entirely on the Planckian nature of CMB

---

[1] From now on we will refer to these contaminant radiation fields as **foregrounds**.

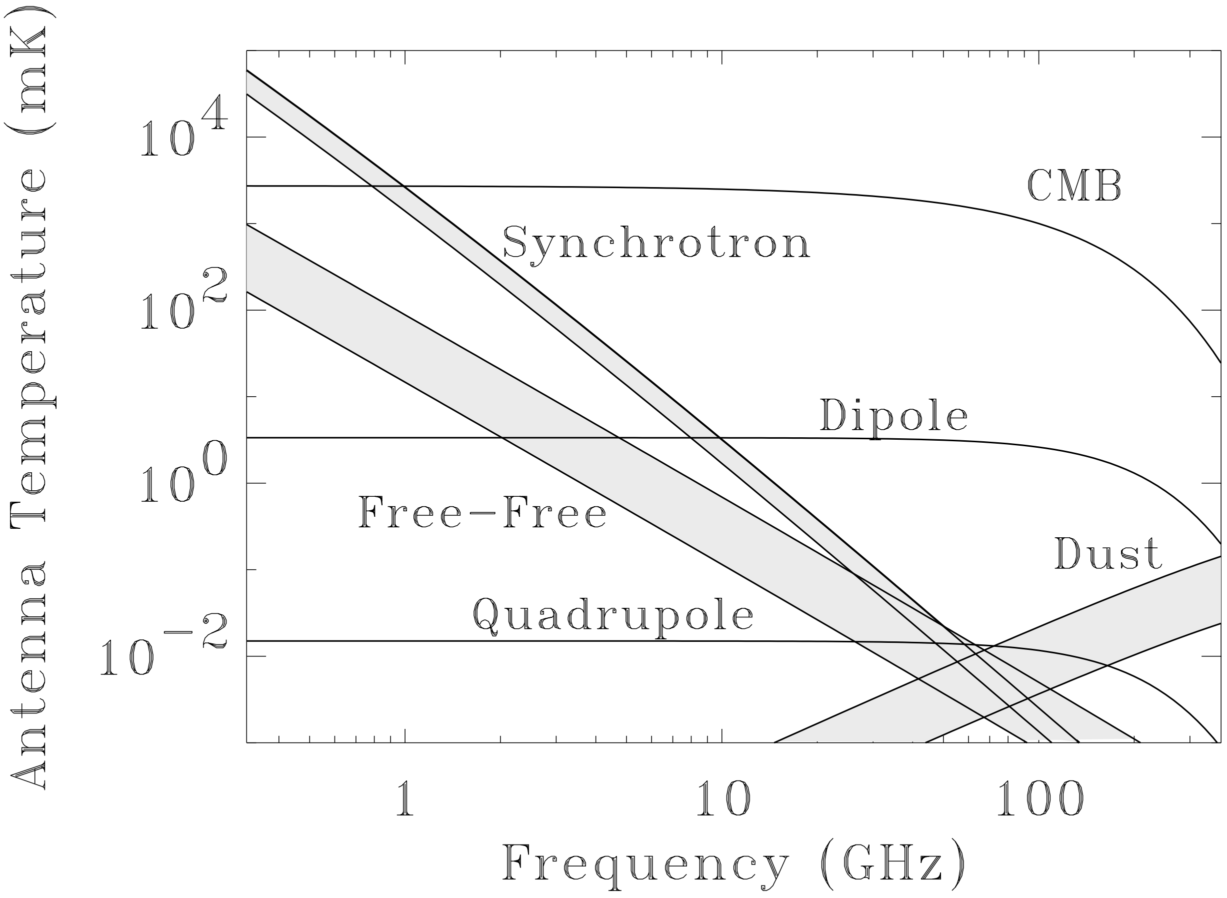

Figure 12: Different Galactic Foregrounds and both CMB emission and its level of anisotropy shown as **quadrupole** (After Smoot 1998)

Figure 13: Angular scales and frequencies where various foregrounds dominate. The shaded regions indicate where fluctuations from different foregrounds exceed the expected levels of CMB anisotropy: green indicates point sources (at low frequencies emission from radio galaxies and at high frequencies from IR galaxies), blue marks the area contaminated by synchrotron radiation, pink is where free-free dominates over CMB and red where CMB is dominated by Galactic dust emission (After Tegmark 1997)

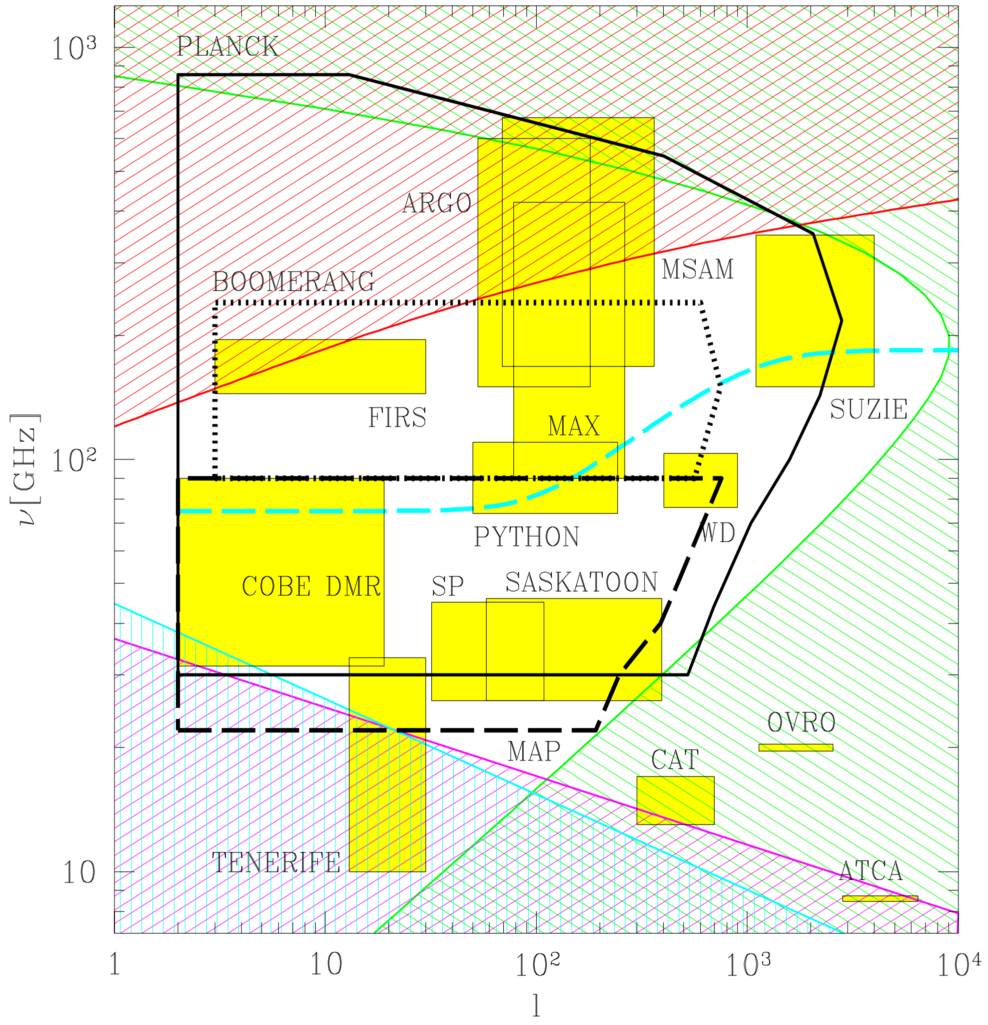

signals versus the characteristic spectrum of each of the foregrounds of concern. In this way, a fit to a multi-frequency observation would isolate the CMB signal (for an example on this technique see [17]). In a series of papers by Tegmark *et al.* [135, 137], new methods are presented which also use the different angular behavior of these foregrounds. An interesting result of such analysis is shown in figure 13 taken from [135].

In this work no attempt to perform any foreground removal was made given the very low S/N ratios. Instead we will show that the different foregrounds are of no concern. The expected levels of foreground contamination are much smaller than the atmospheric noise in each night of observation and even smaller than the observed fluctuations in our final data sets except for the regions close to the Galactic Plane (GP for short). Even so, we incorporate these estimations into the atmospheric technique with the hope of recovering the GP. The statistical analysis applied will also consider the possibility of part of the signal being caused by different foregrounds (see chapter 7) using the peculiar frequency spectrum of these foregrounds.

5.2 Diffuse Galactic Foregrounds

These are the sources of most concern for large and medium angular scale experiments like ours. Three diffuse Galactic foregrounds are of capital importance in searches of CMB anisotropy at cm & mm wavelengths, namely synchrotron emission, free-free emission or bremsstrahlung and dust emission.

5.2.1 Emission Mechanisms

Synchrotron

Relativistic electrons accelerated by magnetic fields produce a complex and characteristic radiation known as synchrotron emission as opposed to the cyclotron emission produced by non-relativistic electrons. Cyclotron radiation constitutes no problem for CMB studies because its emission concentrates on a unique emission line at much lower frequencies than ours. Synchrotron emission exhibits however a very complex spectrum which we describe briefly in this section.

Consider a particle of absolute charge q and mass at rest m_0 moving relativistically[2] with velocity $\vec{v}$ within a magnetic field $\vec{B}$. The spectrum of the radiation emitted by such a particle is (see [112] and references therein):

$$P(\nu, E, \vec{B}) = \frac{\sqrt{3}\, q^3\, B |\sin\alpha|}{mc^2}\, F(\nu/\nu_c) \qquad (19)$$

---

[2] $\beta \equiv \frac{v}{c} \sim 1$, $\gamma \equiv 1/\sqrt{1-\beta^2} \gg 1$. Energy is given by $E = \gamma m_0\, c^2$

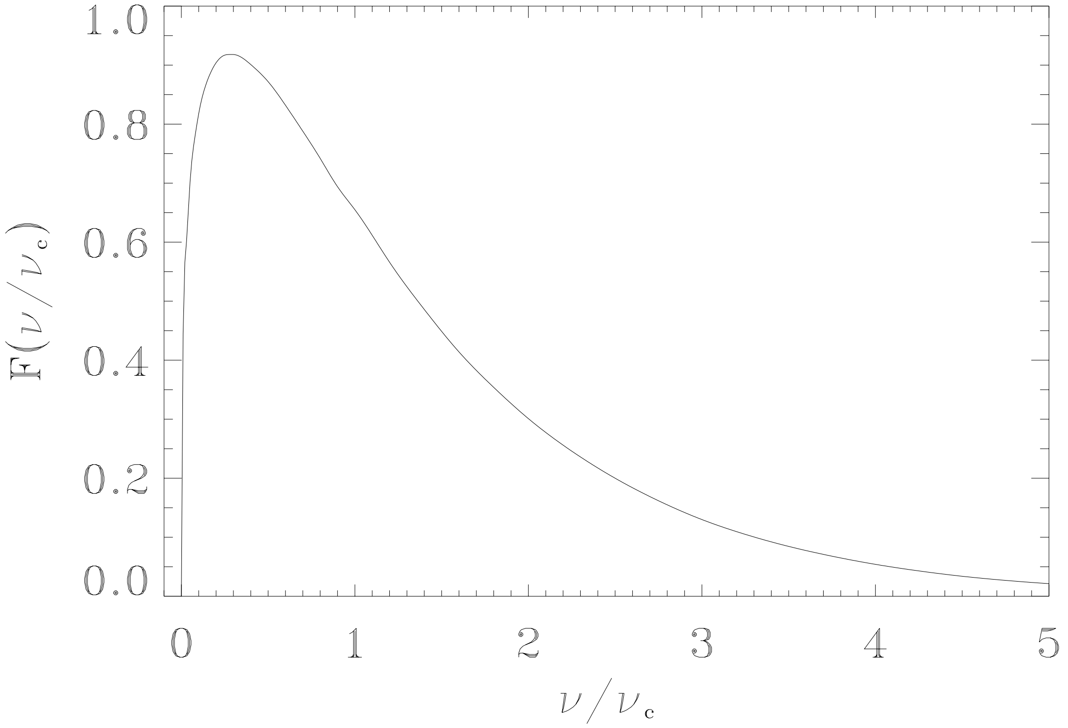

Figure 14: Function describing the spectrum of synchrotron emission

where:

- $F(x) = x \int_x^\infty dz\, K_{5/3}(z)$ and $K_{5/3}$ is the modified Bessel function of 5/3 order. The integral function is plotted in figure 14.
- α is the pitch angle: the angle between $\vec{v}$ and $\vec{B}$.
- $\nu_c = (3\gamma^2 qB|\sin\alpha|)/(4\pi mc) = \frac{3}{2}\gamma^3\nu_B|\sin\alpha|$ where $\nu_B = (qB)/(2\pi\gamma mc)$ is the rotation frequency of the particle in its helicoidal movement . ν_c is a characteristic frequency such that the spectrum of synchrotron emission spans in frequency till about ν_c as seen in figure 14.

The volume emissivity $\varepsilon^{sync}(\nu, \vec{l}, \vec{B})$ at frequency ν towards line of sight $\vec{l}$ is obtained by integrating $P(\nu, E, \vec{B})$ over the particle distribution law of relativistic electrons : $N(E, \vec{l})\, dE \equiv$ number of electrons per unit volume with energies between E and $E + dE$ along line of sight specified by $\vec{l}$. Assuming a power law distribution $N(E, \vec{l})\, dE \propto E^{-p} dE$ we obtain [112]:

$$\varepsilon^{syn}(\nu, \vec{l}, \vec{B}) = \int_{E_{min}}^{E_{max}} dE\, P(\nu, E, \vec{B})\, N(E, \vec{l}) \propto (B|\sin\alpha|)^{\frac{p+1}{2}} \nu^{-\frac{p-1}{2}} \tag{20}$$

Finally, the contribution to brightness temperature due to synchrotron emission wit a power law distribution of energies for relativistic electrons is (k_B is the Boltzmann constant):

$$T_b^{syn}(\nu) = \frac{c^2}{2\nu^2 k_B} I_{syn}(\nu) \propto \nu^{-\beta_{syn}}, \qquad \beta_{syn} = \frac{p+3}{2} \tag{21}$$

Free-Free Emission or Bremsstrahlung

This is the radiation emitted by charges accelerated in the electric field produced by other charges. A classical treatment of this process is possible in the classical energetic regimes, while in other regimes the classical expressions need to be corrected with the Gaunt factors: $g_{ff}(v,\nu)$. Because the ratio q/m is biggest for electrons, we only consider the case where the radiating particles are accelerated electrons. Thus, consider a medium with ion density n_i, with ions carrying a charge Ze, and electronic density n_e with all the electrons with the same velocity v. If we let m be the mass of the electron, then the volume emissivity due to bremsstrahlung is [112]:

$$\varepsilon^{ff}(\nu, v) = \frac{8e^6}{3\sqrt{3}\, c^3 m^2 v}\, n_e n_i Z^2 g_{ff}(v,\nu) \tag{22}$$

By averaging ε^{ff} over a thermal distribution of velocities we obtain the expression for the volume emissivity due to thermal bremsstrahlung for a medium with electronic temperature T_e and ion and electronic densities n_e and n_i respectively [112]:

$$\varepsilon^{ff}(\nu, \vec{l}, T) = \frac{32\pi e^6}{3mc^3}\left(\frac{2\pi}{3k_B m}\right)^{1/2} T_e^{-1/2} Z^2 n_e\, n_i \,\exp\left(-\frac{h\nu}{k_B T_e}\right) \bar{g}_{ff} \tag{23}$$

where $\bar{g}_{ff}$ is the velocity-averaged Gaunt factor. The dependence on frequency of the brightness temperature due to bremsstrahlung can be easily obtained by assuming that the interstellar plasma is electrically neutral, with negligible optical depth and constant electronic temperature along the line of sight [9]:

$$T_b^{ff}(\nu) = \frac{c^2}{2\nu^2 k_B} I_{ff}(\nu) \propto \nu^{-\beta_{ff}}, \qquad \beta_{ff} = 2.+\frac{1}{10.48 + 1.5\ln(T_e/8000K) - \ln(\nu/1\text{GHz})} \tag{24}$$

Dust Emission

Qualitatively this component is easy to understand: light from the interstellar radiation field (ISRF) is absorbed by grains which reradiate at much longer wavelengths. On the other hand, this is the most difficult component to model because of the high number of involved unknowns: dust properties of each kind of grain involved (geometry, size and atomic structure), spatial distribution, temperature distribution of grains and the heating ISRF. In any case it is generally accepted that dust radiates as a grey body: $I_D(\nu) \propto \nu^{\alpha} B_{\nu}(T_D)$, with $B_{\nu}(T_D)$ being the spectrum of a black body at temperature T_D. It is still a matter for debate whether dust emission is only due to a single warm component ($T_D \gtrsim 20K$) with any value for α or it is a superposition of a warm ($T_D \sim 20K$) and a cold ($T_D \lesssim 6K$) components, both of them with $\alpha = 2$ though with different optical depths ([103] versus [16]). Recent works based on fits to DIRBE data [103, 16] indicate that either in the one component or in the two component fits, emissivities should go with $\alpha = 2$.

5.2.2 Estimation Method

Synchrotron and free-free emission

To study the contribution from synchrotron and free-free to our data it is convenient to distinguish between the Galactic Plane ($|b| \gtrsim 12°$) and outside the GP because different processes dominate in each of these regions.

Outside the GP synchrotron emission is the dominant process an it is modeled with a power-law: $T_{sync} \propto \nu^{-\beta}$. The spectral index β is obtained by fitting this law to the low frequency maps at 408 MHz ([57]) and at 1420 MHz ([105]) shown in figure 15. The value assigned to β at pixel (i, j) is obtained as:

$$\beta(i,j) = \frac{\ln[T_{408}(i,j)/T_{1420}(i,j)]}{\ln[1420/408]} \tag{25}$$

Then the synchrotron template is extrapolated pixel by pixel with its corresponding value for β. This method takes into account small spatial variations of β as it is expected if we consider that not only the amplitude of $N(E, \vec{l})\, dE \propto E^{-p} dE$ changes with position but also the value of p and the effective Galactic magnetic field [5, 9]. In any case the values of β obtained are highly clustered around $\beta = 2.9$ [28]. On the other side, studies of the cosmic ray energy spectrum in the Solar vicinity yield a value of $p = 3.3 \pm 0.2$ [9] so we get $\beta = 3.15 \pm 0.10$. It must also be noted that the steepening with frequency of β was already consider by [5], who estimated that this could give a rise of up to $\Delta\beta = 0.25$ in the extrapolation range from 1420 MHz to 10.5 GHz. The more complex estimation procedure considering the cosmic ray energy spectrum was considered by [9], but the difference with respect to our approach is very small [71].

In the GP region the map at 1420 MHz is dominated by free-free emission due to the presence of the Cygnus X HII region and many other unresolved HII regions [29]. A non-negligible contribution from synchrotron in the GP region in the 1420 MHz map is still present given the spectral indexes required to reproduce from 1420 MHz the GP crossings observed at 31.5 and 53 GHz by COBE DMR. On the other hand, to recover the GP at 53 GHz from the 31.5 GHz GP we require a spectral index $\beta = 2.145 \pm 0.005$ (to be compared with $\beta_{ff} = 2.148$ as derived from equation 24). This confirms our initial hypothesis that the GP's seen by DMR at 31.5 and 53 GHz are entirely due to free-free emission. The synchrotron emission (plus any other base level) in the 1420 MHz map was determined by degrading the original map to the DMR resolution and requiring that the free-free signal equals the 53 GHz DMR GP section extrapolated to 1420 MHz. The same process was performed with the 31.5 GHz DMR map, obtaining essentially the same results. Finally, we interpolate back to the original 1420 MHz resolution and subtract the estimated synchrotron to the original 1420 MHz map in order to extrapolate in frequency according to the xpectal index expected for free-free emission. On the other hand, the synchrotron level is extrapolated with a steeper spectral index ($\beta = 2.7$) confirming it yields negligible contributions in the GP section: $rms_{sync}(ch\,1) = 5.3\,\mu K$ with a conservative spectral index for synchrotron emission.

Once we have found out the values of β, we extrapolate the template to each the frequencies of each channel and simulate the observing strategy by convolving the extrapolated map with the instrumental response of each demodulation as obtained in chapter 2.

An alternative approach consists in using other experimental results in the same region of the sky. This is specially convenient to put limits on the contribution of free-free given the lack of any template for this process. The most reliable indication of the levels of contamination by synchrotron and free-free emission is provided by the results of the Tenerife experiment. Taking the detection at 10.4 GHz being caused by both CMB and Galactic signal, while the signal jointly detected at 14.9 and 33 GHz being of CMB origin, [28] obtain a $2-\sigma$ upper limit on Galactic contribution at 10.4 GHz of 43 μK. Assuming a GACF for both the CMB and the Galactic signal we can estimate what the rms value at 10.4 GHz would be for an experiment like ours: $\lesssim$17 and $\lesssim$13 μK for 1F and 2F demodulation respectively. Assuming an spectral index $\beta = 3.0$ (synchrotron) or $\beta = 2.1$ (free-free) yields $rms \lesssim 0.5$ μK for both demodulations at any of our channels. Based on these results we discard synchrotron and free-free emission as potential problems for our data at high $|b|$. It is worth mentioning that the 4-year DMR data [71] place similar limits to those from the Tenerife experiment but at 53 GHz and at larger scales ($\Delta T_{ff} = 6.8 \pm 2.6\,\mu$K) on the contribution from the free-free component correlated with dust emission. Observations of the H_α intensity distribution on smaller angular scales can be used to place similar upper limits to the contribution from the free-free background [107]. According to Reynolds' data we would expect $\Delta T_{ff}/T \lesssim 2 \times 10^{-2}(\nu/1\ GHz)^{-2.1} \csc|b|$, which translates to $\sim 6\,\mu$K at our lowest frequency. Given that both approaches predict very little contributions from synchrotron and free-free emission at high $|b|$ we are confident on neglecting them as sources of astronomical signal.

Dust emission

We have chosen as template for dust emission the 240 μm DIRBE map shown in figure 15 and no attempt to remove the zodiacal contribution was attempted given its low contribution at these wavelengths. To extrapolate to our frequencies we have considered the model by [16] obtained from the fit to the FIRAS data: $I_D(\nu) \propto \nu^2 B_\nu(17.5\text{ K})$. We have checked the validity of this model at low $|b|$ by reproducing the expected dust contribution to the GP seen by COBE DMR at 90 GHz

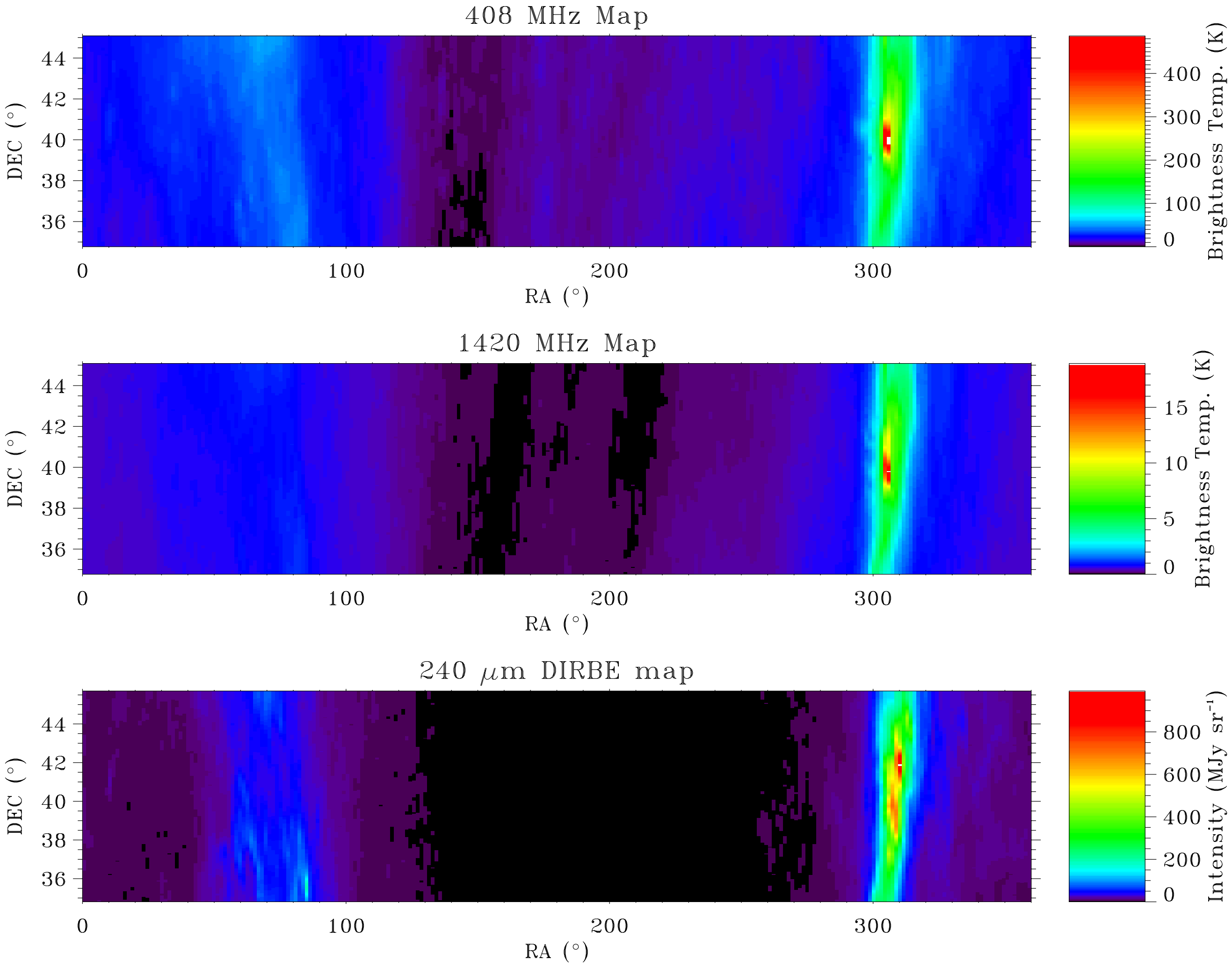

Figure 15: Templates used to model Galactic synchrotron and dust emission.

Table 12: Expected *rms* Values Due To Diffuse Galactic Emission. Units Of μK.

			1F DEMODULATION			2F DEMODULATION		
Model	Reference	Description	rms_{Ch1}	rms_{Ch2}	rms_{Ch3}	rms_{Ch1}	rms_{Ch2}	rms_{Ch3}
1	1	$I_\nu^D \propto \nu^2 B_\nu(17.5)$	1.2	2.4	12.3	0.6	1.3	6.7
2	1	$I_\nu^D \propto \nu^2 B_\nu(18.2)$	1.1	2.2	11.3	0.6	1.2	6.1
3	2	$I_\nu^D \propto \nu^2 (B_\nu(20.4)+$ $+ 6.7 \times B_\nu(4.8))$	1.5	3.1	13.6	0.8	1.7	7.4
4	3	$I_\nu^D \propto \nu^{1.65} B_\nu(23.2)$	1.5	2.9	13.1	0.8	1.6	7.1
5	4	$I_\nu^D \propto \nu^2 B_\nu(18.0)$	1.1	2.3	11.6	0.6	1.2	6.3
6	5	$I_\nu^D \propto \nu^{1.4} B_\nu(23.3)$	2.5	4.9	19.6	1.3	2.6	10.6
7	6	$I_\nu^D \propto \nu^{1.9} B_\nu(18)$	1.3	2.8	13.7	0.7	1.5	7.4
8	7	$I_\nu^D \propto \nu^{1.5} B_\nu(20)$	2.5	5.2	21.4	1.3	2.8	11.6
9	8	$I_\nu^D \propto \nu^{1.5} B_\nu(22)$	2.2	4.3	18.2	1.1	2.3	9.8
10	9	$I_\nu^D \propto \nu B_\nu(22.1)$	7.0	12.5	41.0	3.8	6.8	22.2
11	10	$I_\nu^D \propto \nu^2 B_\nu(22.1)$	0.9	1.5	8.0	0.5	0.8	4.3
12	11	$I_\nu^D \propto \nu^{1.6} B_\nu(24)$	1.6	3.1	13.5	0.8	1.6	7.3

(1) Boulanger *et al.* 1996; (2) Reach *et al.* 1995; (3) Wright *et al.* 1991; (4) Bersanelli *et al.* 1995; (5) Davies *et al.* 1996a; (6) Kogut *et al.* 1996a; (7) Kogut *et al.* 1996b; (8) de Bernardis *et al.* 1991; (9) Banday & Wolfendale 1991; (10) Page *et al.* 1990; (11) Fischer *et al.* 1995.
I_ν^D and $B_\nu(T)$ stand for the dust spectrum and a black-body spectrum at a temperature of T Kelvin respectively.

where the relevant section has been smoothed to 10° FWHM. As in the case of synchrotron + free-free, the estimation of the dust contribution at each of our channels is obtained by convolving the extrapolated maps with the instrumental response obtained in chapter 2. Together with a brief description and reference to the dust model used, in table 12 we give the *rms* values expected from synchrotron plus free-free and dust emission for different dust models outside the GP ($|b| \gtrsim 12°$). These *rms* values are completely negligible as compared to the observed *rms* values in our final data sets (see chapter 7). This can also be seen by using the figure of $\Delta T_{dust} = 2.7 \pm 1.3 \mu K$ at 53 GHz and 10° angular resolution by [71].

5.2.3 Limitations of the Estimations

1. As noticed by [74, 5, 28], the maps at 408 and 1420 MHz suffer from serious systematics effects which limit their utility to predict contributions due to synchrotron emission beyond 10 GHz. Among these systematics effects [28] cite striations caused by the scanning technique used and the accuracy of the zero levels. Specially relevant the latter ones for spurious noise excursions may trigger unphysical β values. In addition, the huge range of extrapolation (over 2 orders of magnitude) greatly amplify any small uncertainty on β to almost an order of magnitude at the extrapolated frequencies. The strips of the maps used in this analysis were unstripped in the way described in [28], but as pointed out by these authors, important striations are left even after accounting for them. We conclude that the approach of modeling synchrotron emission and using the low frequency maps to extrapolate to our frequencies should only be viewed in terms of the order of magnitude of the signal expected from synchrotron: $\lesssim$1 μK at both demodulations and in all channels at high $|b|$.

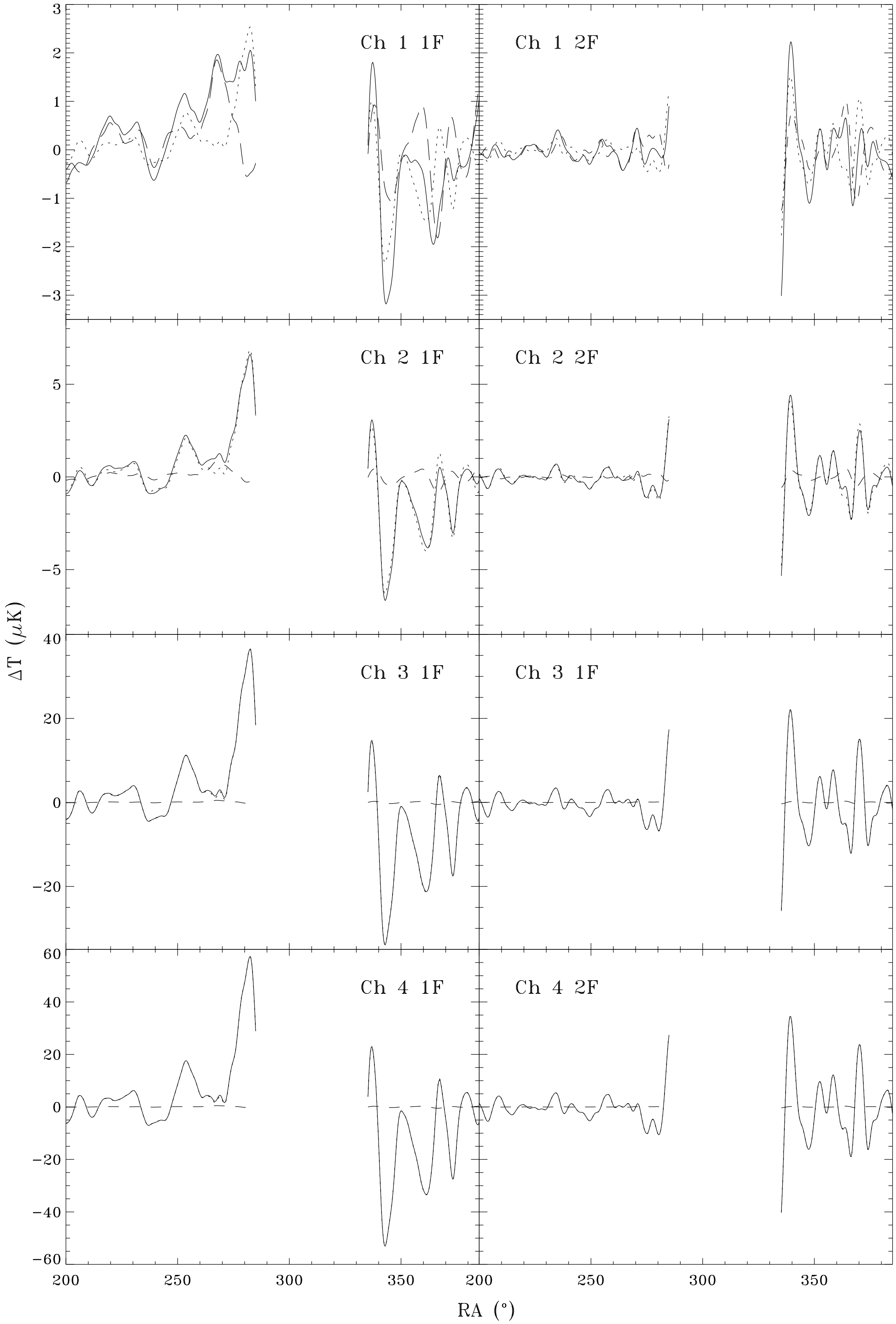

Figure 16: Contribution of the different Galactic Foregrounds at declination 40°. Synchrotron contribution is plotted in dashed lines, dust in dotted lines and the joint contribution in solid lines. We observe that synchroton only contributes significantly at channel 1, while the rest of the channels are affect by thermal dust emission.

2. Experimental measurements of thermal dust emission in the mm and sub-mm range do not yield unique values for (α, T_D), but instead a wealth of models can be found in the literature. Until recently, most models relied on fits to measurements at frequencies much higher than our channels. This situation has changed with the FIRAS data which maps FIR emission in the range [150,3000] GHz. Yet it is not possible to conclude or not on the existence of a cold component ([103] versus [16]). Also, there is evidence of a spatial distribution of temperature values [103] along the Galaxy as expected from the non-uniformity of the heating ISRF and possibly from a non-uniform distribution of dust. There is also the recent controversy about the origin of the correlated signal found between DIRBE and IRAS maps tracing dust emission and CMB maps at frequencies of a few tens of GHz and over a wide range of angular scales [70, 71, 33, 75]. [75] resort to "anomalous" free-free emission due to very hot gas ($T \gtrsim 10^6$ K) in order to explain the excess of emission at 14.5 GHz, while the other authors explain this emission as a free-free component correlated with dust. On the other side, [34] give an alternative answer based on the emission from rotating very-small dust grains while pointing out on the impossibility of being caused by very hot gas.

5.3 Extragalactic Foregrounds

5.3.1 Unresolved sources

The integrated emission of all unresolved sources generate a background whose properties are well know: 50 K at 150 MHz and extrapolated to higher frequencies using a spectral index $\beta = -2.75$ [74]. This value for the spectral index inmediately reveals that the main mechanism of emission by unresolved radio sources is synchrotron emission. According to this model we should subtract to the maps at 408 and 1420 MHz the corresponding EG background contributions which amount to 3.19 and 0.10 K respectively[3]

In addition to the DC level we must consider the fluctuations introduced by the randomly distribution of these undetected sources. At long wavelengths, these fluctuations are due to the emission from radio sources for which deep VLA radio surveys at cm wavelengths (i.e $\lambda \gtrsim 3$ cm) exist. At higher frequencies ($\nu \gtrsim 100$ GHz), far-IR galaxies start to contribute and become dominant at millimetric wavelengths. The studies on the expected levels of fluctuation account properly on the angular power spectrum which can be easily obtained by assuming a Poisson distribution. More refined analysis consider the effect of source clustering, although it turns out not to be specially relevant. More important is the fact that the spectral behavior of each kind of source considered and its evolution in time. Thus, most of the uncertainty is due to the long extrapolations in frequency. In any case we take the results from [42] to exclude such source of fluctuations at our angular scales and frequencies.

---

[3] In addition, to the maps we have subtracted the CMB contribution (2.726 K) and in the case of the 1420 MHz we also apply a zero-point offset of -0.13 K

5.3.2 Resolved sources

This category includes EG sources found in different catalogues: the Kühr catalog [72] and the Green Bank sky survey [22] complemented by the Michigan and Metsahovi monitoring program [52]. The weakest considered source presents a flux density at 5 GHz of 0.18 Jy. We extrapolate the flux density to our frequencies using the fit obtained by [72] where available. Fluxes of sources not present in [72], but for which we have measurements at three different frequencies, were fitted to a power law and extrapolated to our frequencies, while flat spectra were assumed for those sources for which flux densities were available only at a single frequency. The main limitation of this estimation technique lies on the large extrapolations required and lack of knowledge on the behavior of the spectral index in the region over which measurements are extrapolated. A further complication is the variability of some of these sources which would require a constant monitoring. In any case we obtain for all channels and both demodulations values for the expected rms in the section of interest ($|b| > 12°$) much smaller than 1 μK. Such a small value gives us confidence that point sources are of no concern to us despite all above limitations in their modeling.

Chapter 6

Data Processing And Atmospheric Cleaning

In chapters 4 and 5 the different foregrounds susceptible to contaminate our data have been discussed. Their importance to our case has been assesed and it was reached the conclusion that while Galactic foregrounds are of no relevance to us, the primary goal of any data processing should be the reduction of the atmospheric noise present in those data. In this chapter a new simple method to reduce the atmospheric noise is presented. Next, the editions leading to prepare the data before being cleaned are discussed together with the aplication of the aforesaid cleaning technique. Several tests to the method performance are presented. The final section of this chapter discusses how the final data sets are generated by stacking all the data surviving all the data analysis stages.

6.1 Introducing a Method to Reduce Atmospheric Noise

The approach adopted in this work consists in exploiting the high correlation between channels as an indicator of the atmospheric emission so that by using a channel as atmospheric monitor we can clean the rest of the channels. Because atmospheric emission increases with frequency, our highest frequency channel (the 1.1 mm band) is the most sensitive channel to atmospheric emission, Accordingly we adopt this channel as the monitor channel. The method developed and subsequently used relies on a series of simple and realistic assumptions:

- At each channel i we have a superposition of astronomical signal ($\Delta T^{astro}_{ANT,i}$) attenuated by the atmospheric transparency at the frequencies sampled by channel i (f_i), plus the contribution from the atmospheric emission in this band ($\Delta T^{atm}_{ANT,i}$). The indexes ANT refer to the fact we are expressing all quantities in antenna temperature.

$$\Delta T_{ANT,i} = f_i \Delta T^{astro}_{ANT,i} + \Delta T^{atm}_{ANT,i} \tag{26}$$

- The atmospheric contributions are perfectly correlated between different channels:

$$\Delta T^{atm}_{ANT,i} = \alpha_i \times \Delta T^{atm}_{ANT,4} \tag{27}$$

  This assumption is completely justified given the high correlation between data at different channels and taken during the same night of observation (see tables 11, 13 and 14). As explained in section 4.2.3., the high correlation between the time-variable signals recorded at each channel during the same night of observation together with the lack of correlation between data of different nights are the key point to assign atmospheric origin to the fluctuations in the raw data. Further, the amplitude of the signals are too high to be attributed to CMB signal or other astronomical signals (see chapter 5). These considerations allow us to obtain good estimates for the coefficient α_i from the slope of the best-fitting straight line in a diagram $\Delta T_{ANT,i}$ versus $\Delta T_{ANT,4}$. This estimate of α_i is independent of the value of any constant offset present either in $\Delta T_{ANT,i}$ or in $\Delta T_{ANT,4}$.

- Any astronomical signal is perfectly correlated between channels. We denote by ΔT^{astro}_i the thermodynamic value obtained as $\Delta T^{astro}_i = c_i \times \Delta T^{astro}_{ANT,i}$, where the factors c_i are the Rayleigh-Jeans to thermodynamic conversion factors (c_i =1.29, 1.66, 3.66 ,4.82 for channels 1 to 4 respectively). In thermodynamic temperatures, this last assumption is easily written as:

$$\Delta T^{astro}_i = \rho_{i4} \times \Delta T^{astro}_4 \tag{28}$$

  To assign values to the parameter ρ_{i4} we can think of two extreme cases:

  1. The astronomical signal is completely dominated by CMB signal. In this case, because CMB is a perfect black-body emitter, we would have $\rho_{i4} = 1$ for $i = 1, 2, 3$.
  2. The astronomical signal is completely dominated by Galactic emission. Then, because the different foreground contributing to the Galactic emission have strong departures from a Planckian spectrum at $T \sim 3\ K$ we would expect $\rho_{i4} \neq 1$. However we could still obtain estimates for ρ_{i4} from our analysis of the Galactic contaminants in chapter 5.

  The estimates on Galactic contributions to these data allow us to consider we are in case 1 for channels 1 and 2 at $|b| > 12°$, and in case 2 for channels 3 and 4 and for all channels when we are close to the Galactic Plane. For the latter case, this does not constitute any problem given the extremely high degree of correlation between channels 3 and 4 at any demodulation given their proximity in frequency. Thus, when we subtract atmospheric noise to channel 3 with channel 4 we would also be subtracting to a high degree the part due to Galactic emission. It is also important to point out that when correcting channels 1 and 2 any contribution from the Galaxy is going to be reduced by the factor α_i, which exhibited averaged values of 0.3 and 0.4 for channels 1 and 2 respectively for the data at both demodulations used to generate the final data sets. The introduction of the factor ρ_{i4} is of crucial relevance if an attempt is to be made to recover the Galactic Plane crossing. This is discussed later in this chapter as the recovery of the Galactic Plane in all channels constitutes an important test on the performance of the cleaning technique.

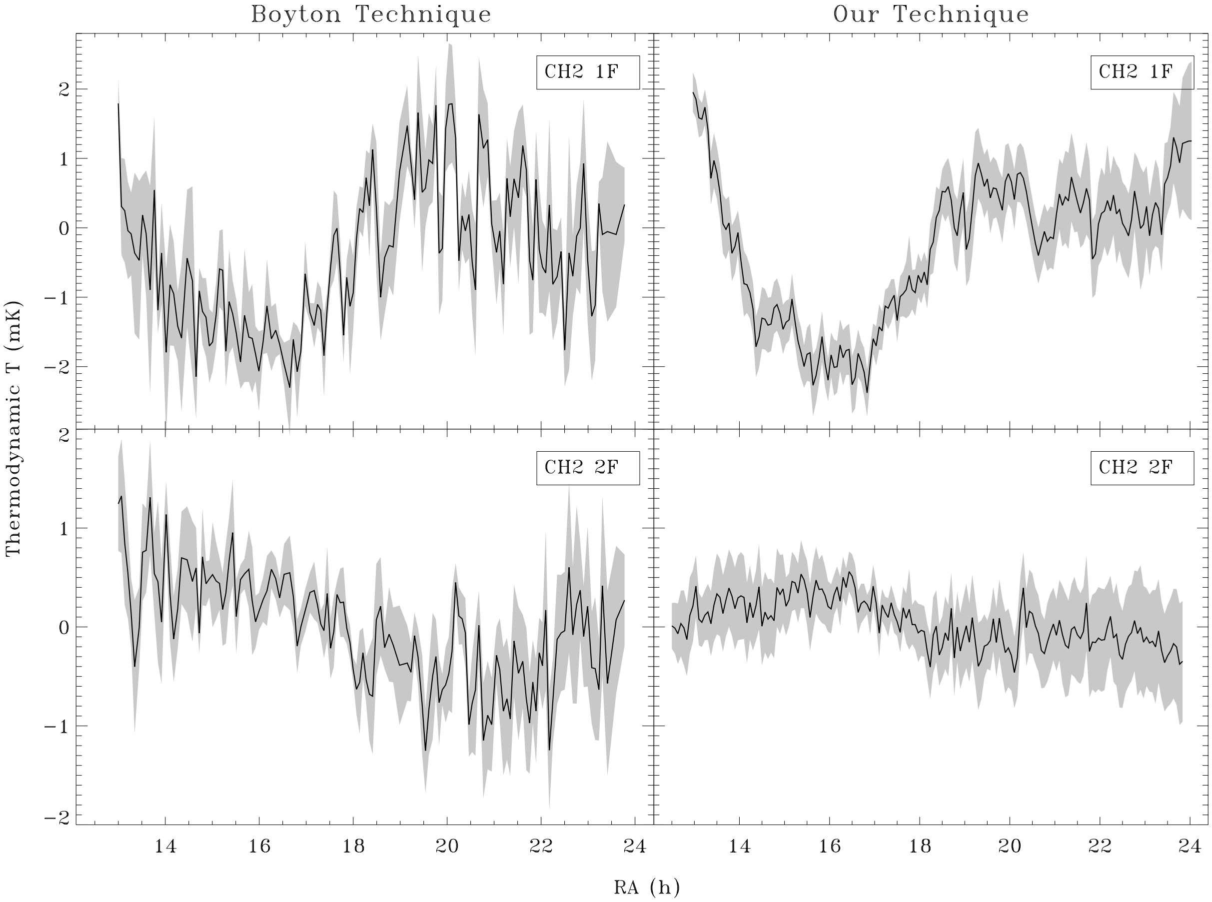

Figure 17: Comparison between the outputs of the cleaning technique developed by us and that of Boyton. Shaded regions represent the ±2σ regions.

Putting all these pieces together, to recover the astronomical signal at channel i in thermodynamic temperature (ΔT_i^{astro}) and referred to the top of the atmosphere we only need to solve the following linear equation:

$$\Delta T_{ANT,i} = \frac{f_i}{c_i}\Delta T_i^{astro} + (\Delta T_{ANT,4} - \frac{f_4}{c_4}\frac{1}{\rho_{i4}}\Delta T_i^{astro}) \times \alpha_i \tag{29}$$

To our knowledge, prior to this work only one attempt was made to clean millimetric data from atmospheric emission. This method was first proposed by P. Boynton in 1974 and it is sketched in [86]. It also consists in simultaneous observations at two different frequencies away from atmospheric lines so that there is a linear relation between the atmospheric absorptions. Performing the sum (S) and subtraction (D) of the two channels and then a linear fit S versus D would yield the value of the astronomical signal. This procedure was attempted by [2] without success. In any case, this method was also applied to our data yielding cleaned scans very similar to those obtained with our technique as can be seen in figure 17. This is not surprising for both methods are based on the same underlying idea: using a channel as atmospheric monitor and exploiting the high correlation caused by atmospheric emission. The advantage of the Boyton method is that it does not require prior knowledge of the atmospheric transparencies but does not allow for the astronomical signal to have different amplitudes at each channel. Therefore, while we could still recover a feature looking like the Galactic Plane, its amplitude would not match that from the predictions. On the other side, our method requires the knowledge of realistic atmospheric opacities. This is achieved by using atmospheric data and the use of an atmospheric transmission code such as that by [27] (see below in this chapter).

6.2 Data Processing

The process the data go through in order to generate the final data sets encompasses the following data editions and binnings. These stages are summarized below and explained in detail in the following sections:

1. A first edition selects those portions of data from which the auto-correlation curves of the data for each night of observation will be obtained (section 6.2.1)
2. The knowledge of the auto-correlations allow us to bin the data assigning proper error bars (section 6.2.1)
3. Application of the cleaning technique to the fraction of data selected in the first edition (section 6.2.2)
4. Binning from 10 seconds to 4 minutes and removing remnant baselines (section 6.2.3)
5. Stacking of the scans at 4 minutes to generate the final data sets (section 6.2.3)

6.2.1 Preparing the Original Data To Be Cleaned

As explained in chapter 2, the detectors are sampled at a rate of 80 Hz. The demodulation process produces a single data point every 0.25s per each 1F and 2F demodulation and per channel. During the demodulation 3.3% of the data was rejected due mainly to problems of synchronism between the mirror movement as identified from the values of the flag in the long frames (see chapter 2, section 2.1.3). However, the bulk of the rejection is done in subsequent phases of binning and edition of the data. Thus, after demodulation, a first binning is done to bring the data from 0.25s to 10s. This is a iterative process for, as discussed in chapter 4, the knowledge of the auto-correlation curves, $\rho(\tau)$, is needed in order to have good estimates of the associated error bars. The first binning does not consider any auto-correlation curve and is intended only to select good portions of data having all of them the same levels of noise and which will be used to compute $\rho(\tau)$. Most of the sections of data discarded in this first edition correspond to the beginning of the night of observation, when the detectors are settling down, to periods of bad weather and when we ran out of liquid Helium and the cryostat started warming.

Once the auto-correlation curves have been obtained, the data are binned from 0.25s to 10s using equation 16 to assign error bars. This binning process applies an iterative 3σ filter to discard glitches due to malfunctions of the data acquisition system not reflected in the flag of the long frames. Bins of of 10s should contain about 40 points but because of missing points during the acquisition of data or demodulation or glitches removal, it often occured that that condition was not satisfied. Therefore, bins of 10s constructed using less than 15 data points at 0.25s were discarded. In total, the amount of data rejected in this binning process is about 8% for all channels and both demodulations.

The choice of a 10s bin size was motivated by inspection of the auto-correlation curves for the 2F demodulation for the whole campaign and very similar to those depicted in figure 11. The choice of 10s corresponds to a trade-off between the need to reduce correlation between adjacent bins ($\rho(10s) < 35\%$ for the 2F data) and still having a large number of points for the linear fits involved in the cleaning technique. The binning is also necessary to ensure we are in a domain of frequencies where noise is dominated by atmospheric fluctuations: at 0.25s the cleaning technique could not be applied because instrument noise would spoil the high correlations required for the technique to work. Once it was chosen for the 2F data, we kept attached to it for the 1F data to avoid processing each demodulation in different ways.

6.2.2 Cleaning of Data

The cleaning technique is applied to the data binned to 10s after subtracting a constant offset to each channel. In figure 18 we show a typical night of observation after the first edition and binning to 10s. In figure 19 we can see the same data after being cleaned from atmospheric noise. In figures 18 we observe that our data are offseted previous to applying the cleaning in all channels by an amount which increases with frequency, the same as the atmospheric fluctuations. The origin of this offset is not very clear, but it is thought it could be due to the wobbling axis was not exactly vertical so that the detectors are seeing different air masses as the mirror wobbles. This interpretation is strongly supported by the fact that it is always negative, implying it can not be due to gain fluctuations since these are supposed to be random and should be negative and positive with the same frequency. Superimposed to this offset we can clearly observe a modulation of very large period. These ondulations are known as baselines and are mainly due to atmospheric fluctuations at very large angular scales. They are also supposed to be of atmospheric origin because of the obvious correlation between baselines at different frequencies (gain fluctuations in the detectors are not expected to be correlated) . Figure 18 is also instructive to show the high correlation between channels which we have been pointing out as cornerstone for our atmospheric technique.

In the atmospheric cleaning we fit channel i versus channel monitor in 5 minute segments. These linear fits yield the values for the correlation coefficients α_i in equations 27 and 29. The implementation of the cleaning process required a correlation higher than 75% between channel i and monitor channel for the linear fit to be considered so that the assumption of correlation between atmospheric components at these two channels is accomplished with enough stregth. Because both

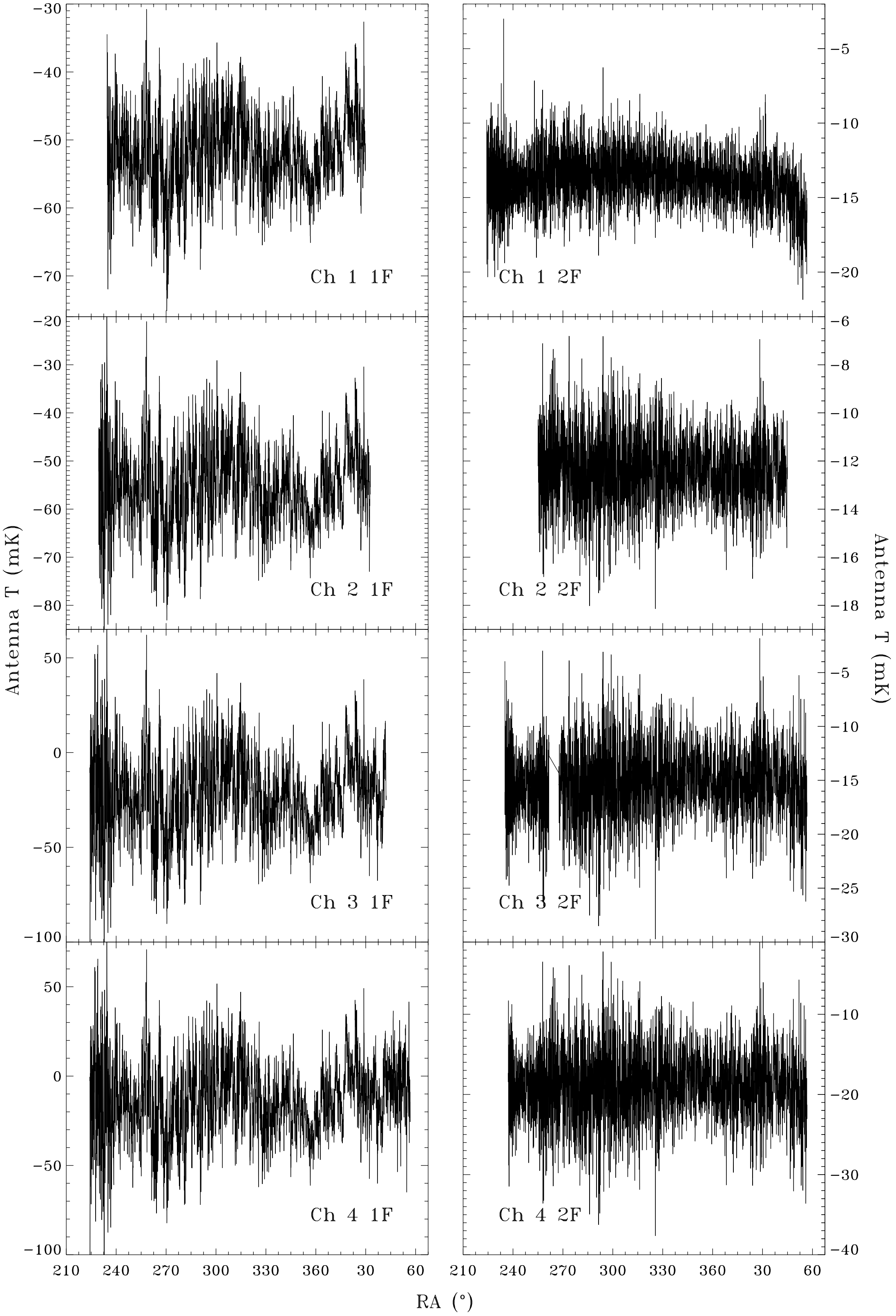

Figure 18: Typical night of observation at 10s bin size before applying atmospheric cleaning. The gap in the scan for channel 3 2F as well as the different starting and ending times for each scan are due to the rejection of data done during edition prior to cleaning.

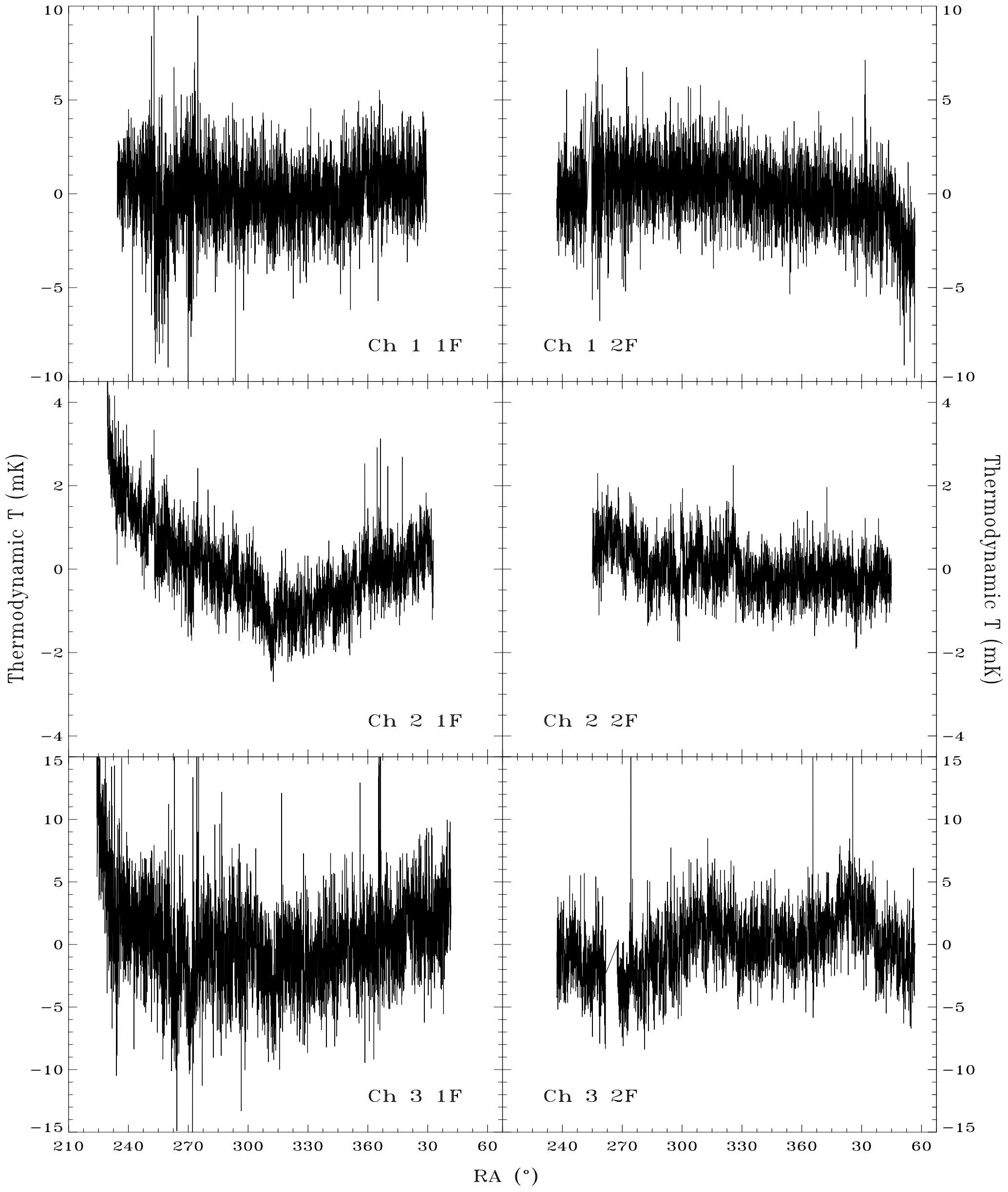

Figure 19: Same night of observation as in previous at 10s bin size after applying atmospheric cleaning.

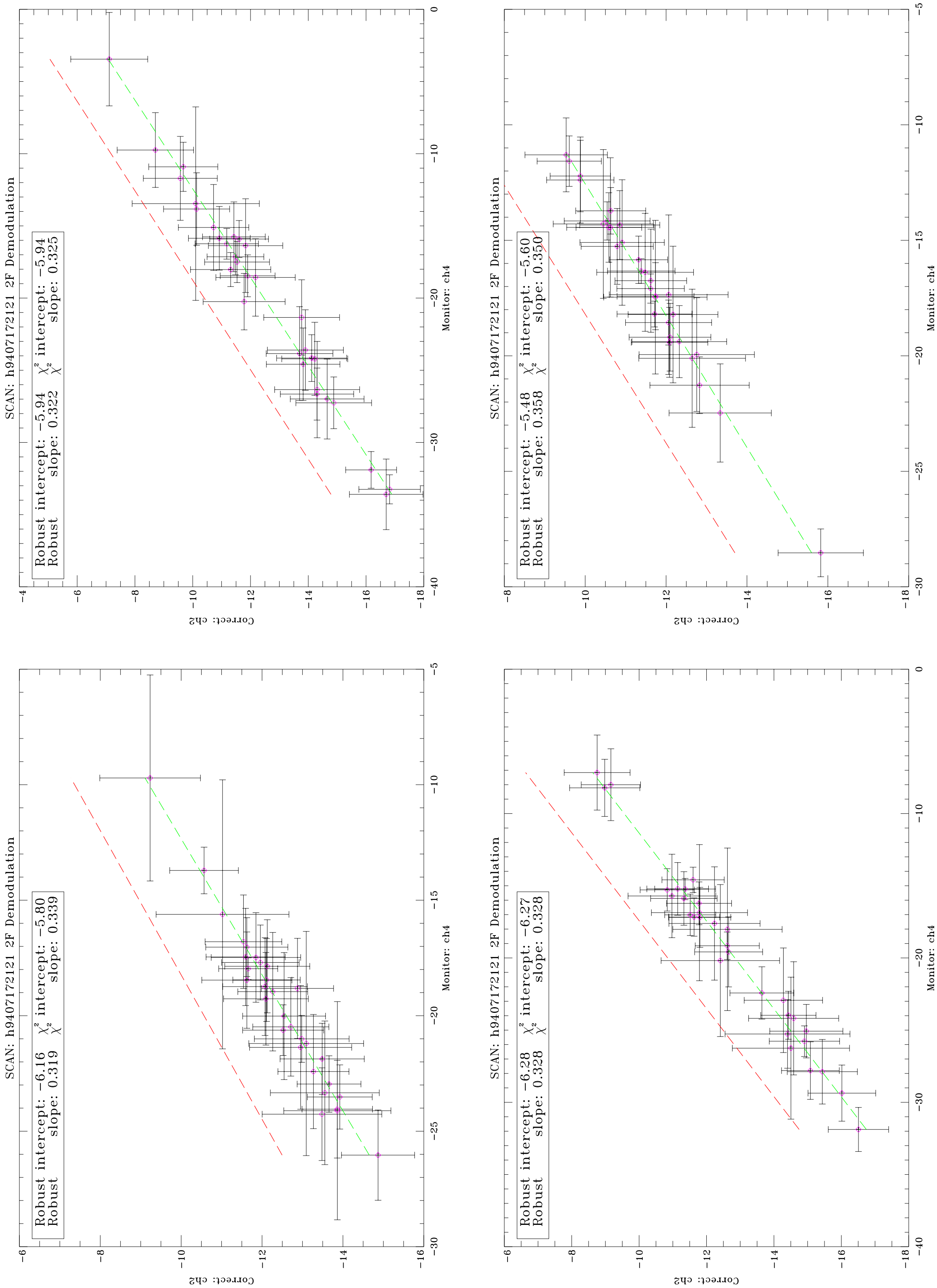

Figure 20: Several examples of linear fits between channel to be corrected and monitor in order to obtain an estimate for α_i. In order to being able to see both fits, the robust linear fit (red dashed lines) has been displaced vertically. Green dashed line corresponds to the χ^2 linear fit.

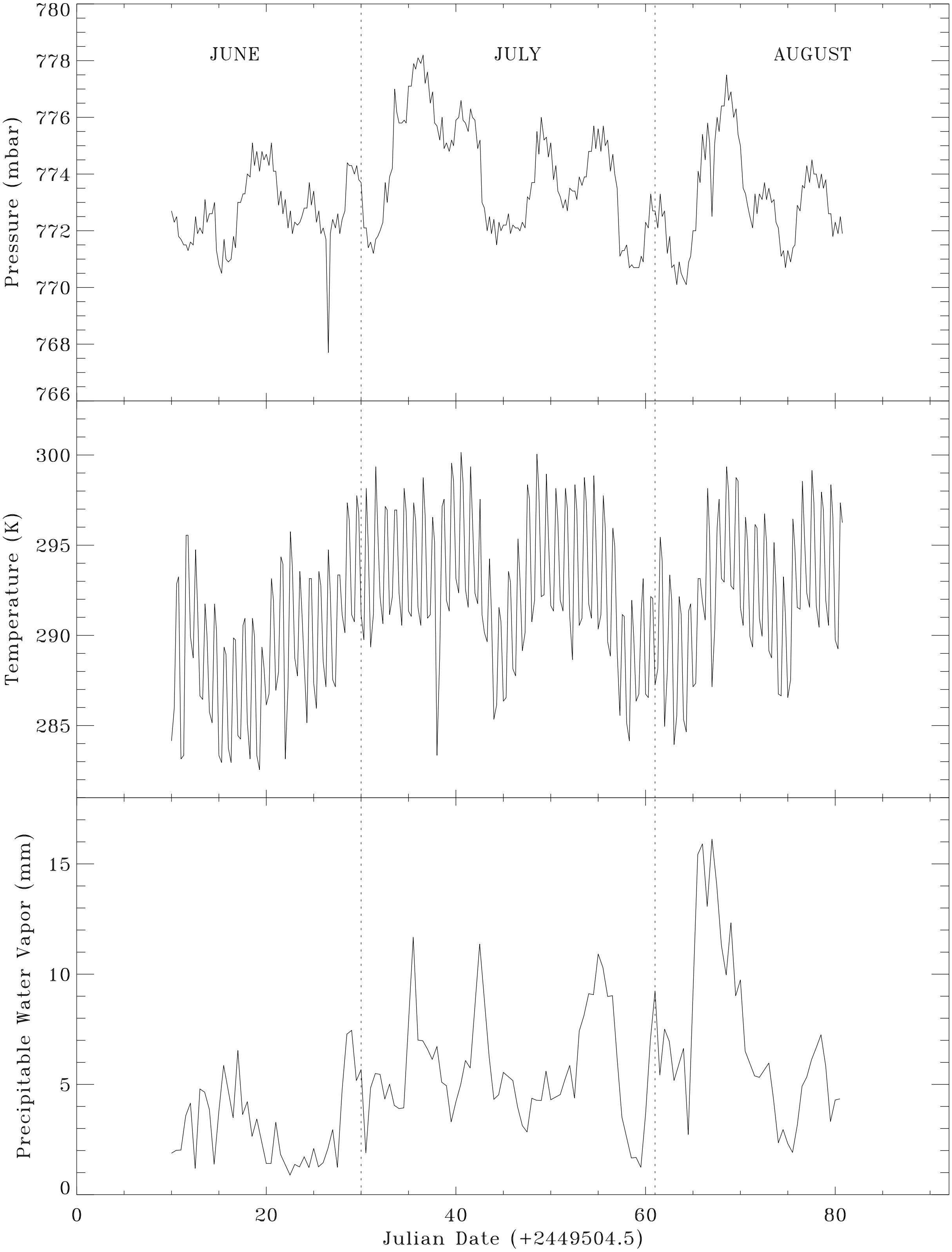

Figure 21: Weather conditions during the 1994 observing campaign.

Table 13: Summary of cleaning process on selected data at 1F demodulation.

	CHANNEL 1			CHANNEL 2			CHANNEL 3		
Filename	Correlation (%)	$rms_1^\star$ (mK)	$rms_2^{\star\star}$ (mK)	Correlation (%)	$rms_1^\star$ (mK)	$rms_2^{\star\star}$ (mK)	Correlation (%)	$rms_1^\star$ (mK)	$rms_2^{\star\star}$ (mK)
h9406201832				100	26.80	1.49	100	143.64	3.96
h9406212000				99	11.18	1.60	100	59.73	4.15
h9406222042	99	10.36	1.43	92	15.01	5.95	100	86.79	4.77
h9406240347	90	5.74	2.38	100	5.86	0.57	100	30.90	2.20
h9406242103	98	7.74	1.44				100	69.52	3.69
h9406252025	99	13.71	1.45	100	23.13	0.95			
h9406262040	97	6.41	1.26				100	55.34	2.58
h9406271804	98	7.15	1.30				100	71.92	3.76
h9406282017	99	24.51	2.40						
h9406292341	100	23.51	1.91	100	48.12	1.50			
h9407011936				100	24.56	0.80	100	130.45	5.66
h9406302037	99	22.72	2.52						
h9407031751	100	24.01	2.54						
h9407140204	100	33.69	1.47‡						
h9407142057	100	12.32	1.26‡						
h9407162229				99	15.61	2.39	100	86.32	10.29
h9407172121	97	7.18	1.91	100	14.09	1.04	100	77.31	3.84
h9407182057				100	54.30	1.64			
h9407192005	100	41.02	2.11	100	90.01	3.45			
h9407211959				100	72.21	2.70			
h9407232112	99	21.37	2.40						
h9407272008				100	76.03	1.80			
h9407282007	99	12.91	1.68	100	23.97	0.80	100	133.91	4.66
h9407291955							100	158.62	4.62

* *rms* values obtained from files before cleaning from atmospheric noise

** *rms* values obtained from files after cleaning from atmospheric noise

‡ Files cleaned using channel 3 as atmospheric monitor due to problems with channel 4.

Table 14: Summary of cleaning process on selected data at 2F demodulation.

	CHANNEL 1			CHANNEL 2			CHANNEL 3		
Filename	Correlation (%)	$rms_1^{\star}$ (mK)	$rms_2^{\star\star}$ (mK)	Correlation (%)	$rms_1^{\star}$ (mK)	$rms_2^{\star\star}$ (mK)	Correlation (%)	$rms_1^{\star}$ (mK)	$rms_2^{\star\star}$ (mK)
h9406161756	98	8.40	2.20[‡]	100	15.56	1.49[‡]			
h9406192035	94	5.18	1.87	97	7.77	2.38	99	20.49	11.62
h9406201832	91	3.63	1.69	100	5.26	0.53			
h9406212000	82	2.15	1.43	99	2.45	0.48	100	12.15	2.54
h9406222042	90	2.73	1.27				100	13.18	1.70
h9406240347	72	1.64	1.18[†]	92	1.30	0.63	100	6.11	1.39
h9406242103	76	1.67	1.22[†]				100	9.09	2.21
h9406252025	94	2.95	1.18	99	3.82	0.52	100	18.81	2.64
h9406262040	71	2.10	1.24[†]				100	8.27	1.30
h9406271804	76	3.01	1.30[†]				99	6.12	1.45
h9406282017	95	6.16	2.15						
h9406292341	98	4.78	1.20	100	7.92	0.81			
h9406302037	97	5.12	1.38	98	8.43	1.80			
h9407011936	96	3.66	1.17	100	5.66	0.55	100	28.32	4.21
h9407021937	99	6.63	1.26	100	10.57	0.89			
h9407031751	98	5.66	1.30	100	9.05	0.93			
h9407041750	99	6.79	1.36						
h9407140204	98	5.16	1.26[‡]						
h9407142057	90	2.45	1.19[‡]						
h9407152041	88	2.14	1.26[‡]						
h9407162229				98	2.78	0.66	99	13.19	5.47
h9407172121	70	2.25	1.80	98	2.36	0.59	100	11.67	2.70
h9407192005	99	111.74	1.76	100	19.59	1.35			
h9407211959				100	15.74	1.12			
h9407222108				100	13.13	1.25			
h9407232112	97	6.08	1.66	99	10.08	1.51			
h9407282007	92	3.19	1.42	99	4.19	0.60	100	15.73	3.31
h9407291955							100	11.18	2.10
h9408022032							100	26.20	5.62
h9408040057							100	13.20	3.05

[$\star$] *rms* values obtained from files before cleaning from atmospheric noise

[$\star\star$] *rms* values obtained from files after cleaning from atmospheric noise

[†] For these files there was not any clear improvement in using the atmospheric technique. They were only binned from 0.25s to the final bin size and then the baselines were removed as described in section 6.3

[‡] Files cleaned using channel 3 as atmospheric monitor due to unknown problems with channel 4.

channels have their corresponding error bars, the linear fit took this into account (e.g. see [102], chapter 15.3). To avoid spurious values of α_i caused by glitches within the bins of 5 minutes and surviving the filters so far, the above linear fit was compared with that resulting from a robust linear fit where the figure of merit is the absolute deviation[1]. In figure 20 several examples of these fits used in the cleaning of scan h9407172121 at 2F demodulation (see figures 18 and 19).

Another feature of the cleaning process concerns the evaluation of the atmospheric opacities at different frequencies. All points within the same 5 minute segment in the above linear fitting share the same f_i and f_4 as computed from the splined values of water vapor w, pressure P and temperature T from figure 21 used as input to the code by [27], which computes the atmospheric opacities due to water vapor and oxygen using the US standard atmosphere model [141]. The pressure and temperature data in figure 21 were collected at the observing site four times a day, while the data on water vapor were obtained from the measurements of balloons launched twice a day by the Spanish Meteorological Institute from sea level. In our case, the precipitable water vapor is obtained by integrating these balloon measurements from the Observatory level up to 12-15 Km.

A summary of the application of our cleaning technique is given in tables 13 and 14 where we list all those files selected to generate the final data sets at each channel and demodulation. For all these files we present the correlation between each cleaned channel and the monitor channel, the rms values before and after cleaning for the atmospheric noise and the number of points at 10s used. During the campaign, for some unknown reason, channel 4 did not work properly for a few days. In these cases, we use channel 3 the monitor channel. These files are marked in the table with a dagger symbol. It is also relevant to point out that for a randomly sample of scans the cleaning process was repeated to clean channels 1 and 2 using channel 3 as atmospheric monitor. The average Spearman correlation factor when comparing the 1F demodulation for channels 1 and 2 was 98% while for the 2F demodulation the average correlation factor was 93%. This indicates that there are no dramatic changes if instead of using channel 4 as monitor, we decide to use channel 3 such as stated by the second assumption done on formulating the reduction technique.

6.2.3 Producing the Final Data Sets

After cleaning, a new binning is performed to bring each processed night of observation from 10 second to 4 minute bin size (i.e 1° in RA) so the beam is sampled with at least 3 points. Once again a 3σ filter is applied to discard possible glitches occurred during the cleaning process. To each point at 4 minutes we assign an error bar given by the standard deviation of the mean of all points at 10s within the bin at 4 minutes. A similar analysis to that performed in chapter 4 (section 4.2.2) allows us to obtain the mean auto-correlation function for the processed data in each channel and both demodulations. These auto-correlation curves are shown in figure 22. From them we observe that points separated by 4 minutes the auto-correlation for all channels 1 to 3 and both

---

[1] The reason why we only use a robust method to make sure that possible outliers are not affecting the result is that while for χ^2 it is possible to get analytical expressions for the uncertainty on the model parameters, for robust methods there is no such analytical expressions.

demodulations ranges between 9% (Ch 2 1F) and 1% (Ch 1 2F). Therefore, our 4 minute bins can be considered uncorrelated as well as their error bars. In both demodulations and in all channels we observe residual baselines of very long periods. We proceed to remove these remnants by fitting linear combinations of sinusoidal functions after a re-edit of the data. The re-edit discards noisy sections which may affect the fitting process. The minimum period of the sinusoidal functions is chosen to be large enough so to remove signals corresponding to angular scales bigger than the ones to which the instrument is sensitive. Thus, for the 1F data the minimum period is 90° in RA and a minimum period of 72° in RA for the 2F data. These minimum periods were obtained from the inspection of the window functions described in chapter 2.

In figure 23 we display these various stages of the cleaning technique for a typical night as seen in all channels and both demodulations. In the last column of table 15 we give the mean amplitude of the baseline fits. Columns 1 and 2 show the percentage of total data used with respect to the original data at 0.25 s and the number of nights used to generate the final data sets. The percentage of data used is bigger in the 2F data as well as the number of used nights, with the exception of channel 3. The final data sets were obtained by stacking all individual baseline-cleaned nights where the *rms* did not exceed 0.65, 1.3 and 2.5 mK for channels 1, 2 and 3 respectively in the 1F demodulation and 0.4, 0.4 and 2.0 mK for channels 1, 2 and 3 respectively in the 2F demodulation. Column 3 in table 15 gives the mean *rms* in thermodynamic units for the surviving nights once residual baselines have been removed. The stacking process consists of computing weighted averages, where to the ith bin in the final data set we assign a value and error bar given by:

$$\overline{\Delta T_i} = \frac{\sum_{j=1}^{n_i} \Delta T_{ij}/\sigma_{ij}^2}{\sum_{j=1}^{n_i} 1/\sigma_{ij}^2} \tag{30}$$

$$\sigma_i^2 = \frac{\sum_{j=1}^{n_i} (\Delta T_{ij} - \overline{\Delta T_i})^2/\sigma_{ij}^2}{(n_i - 1)\sum_{j=1}^{n_i} 1/\sigma_{ij}^2} \tag{31}$$

where the indices ij refer to bin i in night j, ΔT_{ij} and σ_{ij} are the data point and standard deviation at bin i in night j, and n_i is the number of nights used for this ith bin in the final data set. The final data sets in the regions before and after the Galactic Plane crossing are shown in figure 24.

6.3 Testing The performance of the Technique

In this section several tests on the performance of our data analysis are presented. The result of these tests confirm that though a good rejection of atmospheric noise is achieved we dot yet achieve the white noise behavior expected from instrument noise alone.

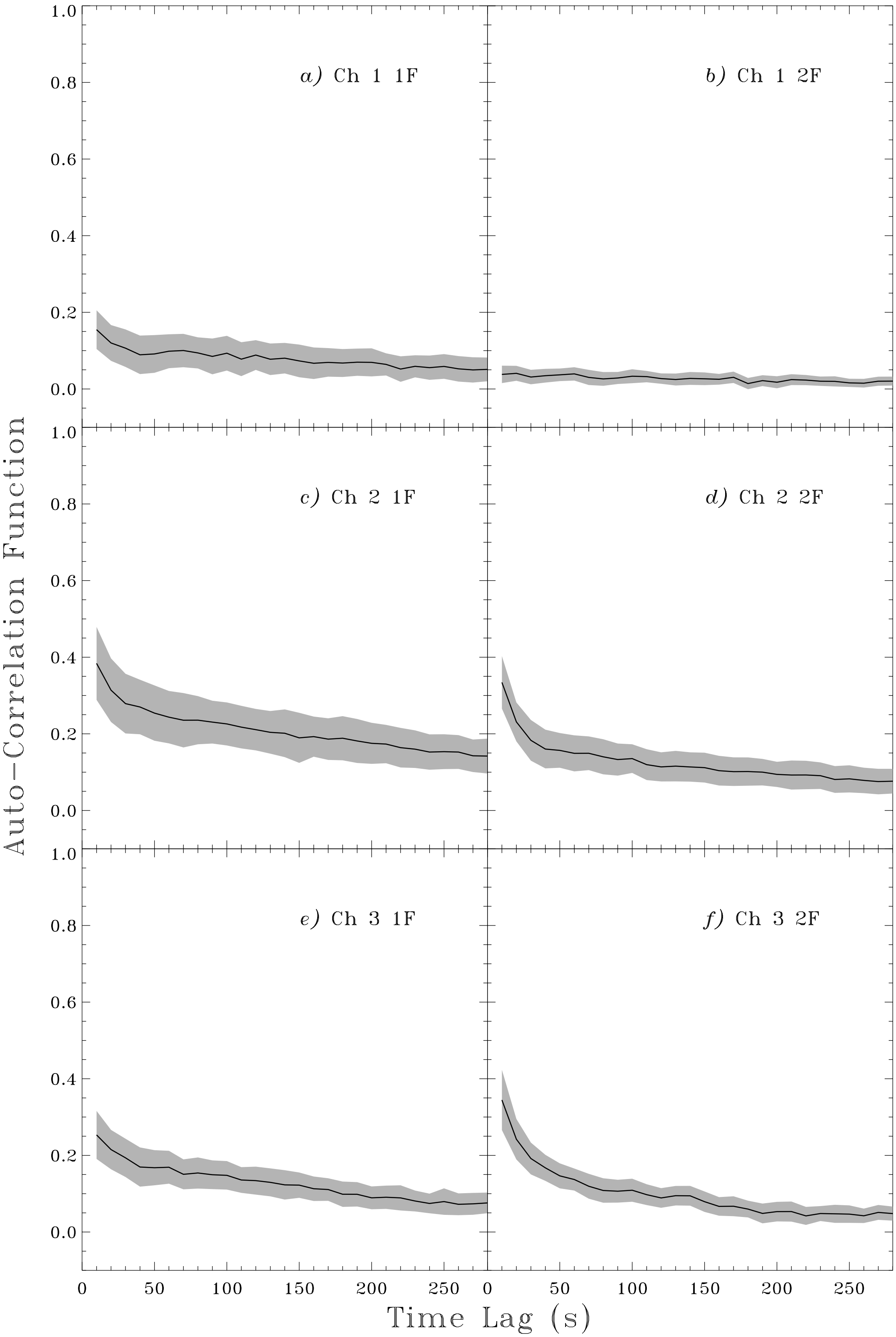

Figure 22: Averaged auto-correlation curves for the data in channels 1 to 3 and both demodulations after cleaning from atmospheric noise. This figure should be compared with the equivalent in chapter 4. The shaded reiong correspond to the $\pm 2\sigma$.

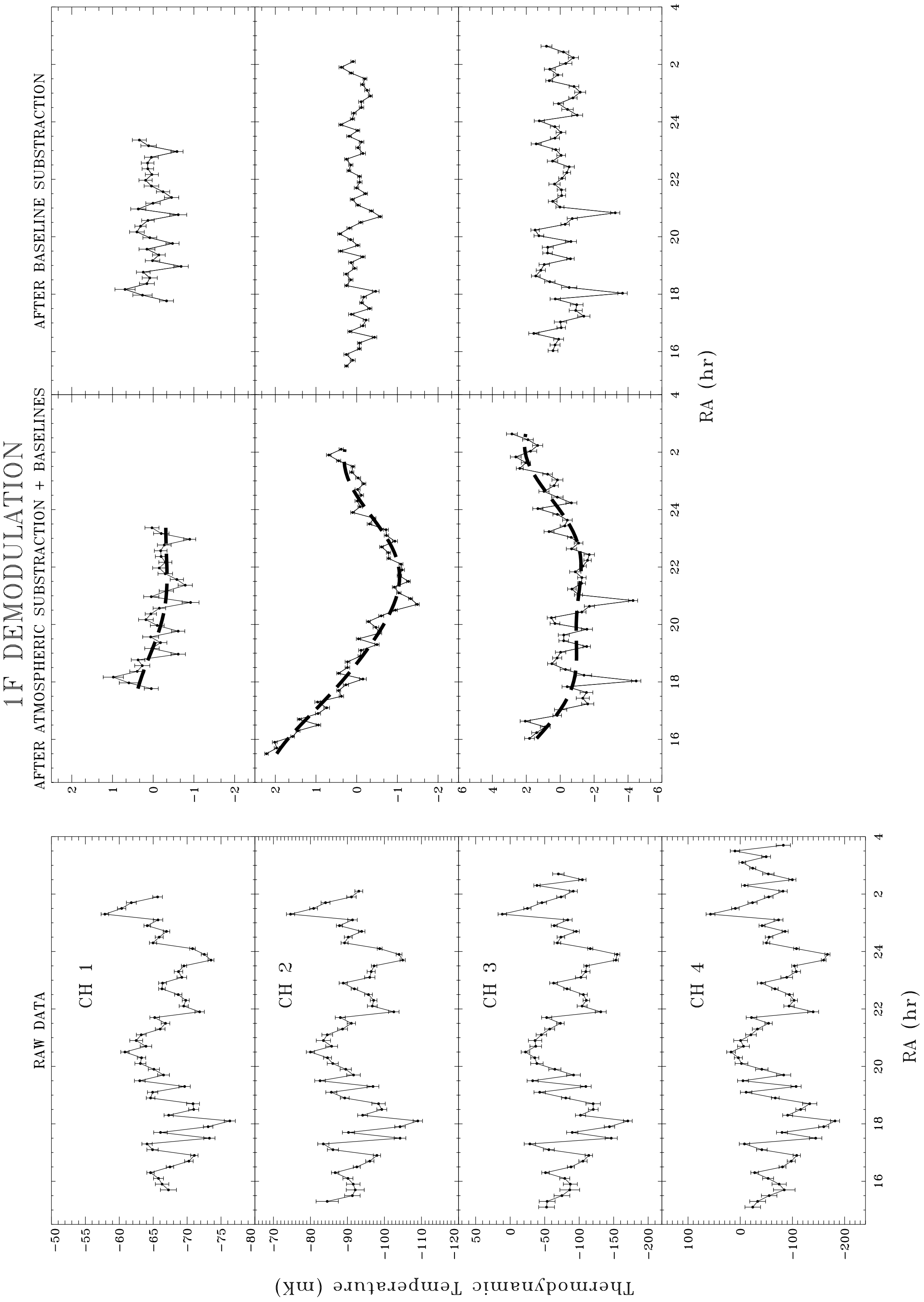

Figure 23: The different stages of the cleaning technique. Panels in the left column show the raw data. Center panels display the output of equation 23, superimposed the sinusoidal fit (thick dashed line). Right panels show the cleaned data with the baseline removed. All plots have been brought to a bin size of 3° in RA for display purposes. Temperatures in this figure refer to thermodynamic temperature values.

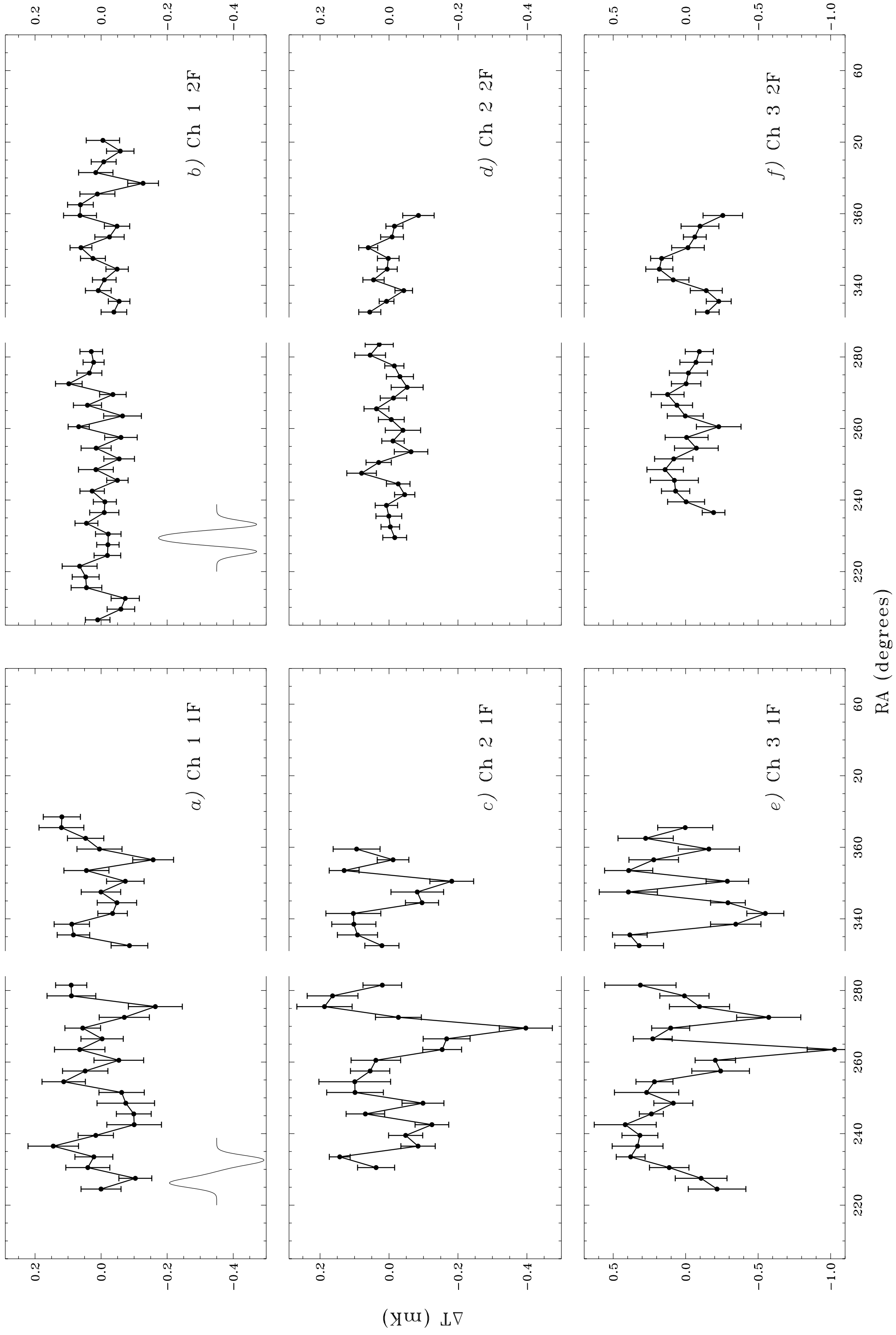

Figure 24: Final data sets in the regions to be considered for the posterior Likelihood analysis. The data have been binned to 3° in RA for clarity. We also show the the 1F and 2F profiles indicating the instrument response to point sources. Temperatures in this figure refer to thermodynamic temperature values.

Table 15: Data Used To Generate Final Data Sets.

Cannel	Percentage	Number of Nights	Mean rms (mK)	Amplitude Baseline (mK)
		1F DEMODULATION		
1	17.2 %	16	0.392 ± 0.024	0.78 ± 0.19
2	13.3 %	14	0.48 ± 0.07	1.23 ± 0.23
3	16.8 %	12	1.30 ± 0.14	1.81 ± 0.23
		2F DEMODULATION		
1	30.1 %	24	0.275 ± 0.024	0.46 ± 0.08
2	15.4 %	18	0.233 ± 0.018	0.85 ± 0.23
3	14.5 %	15	0.86 ± 0.12	1.28 ± 0.25

6.3.1 Comparison of *rms* Values Before and After Cleaning the Data

This is the obvious way to compare the data for it gives a fairly good idea of how much noise has been reduced in the data. Indeed, this comparison has already been done in tables 13 and 14 for the files selected to generate the final data set for each channel in both demodulations. A better way of doing the same comparison is to study the distribution of *rms* values and compare with the white Gaussian noise case as it was done in chapter 4. In figure 25 we show such a comparison between theory and observations for the whole cleaned data set. We observe a much narrower distribution for the *rms* distribution than in the case of unprocessed data. Yet, we are far from the ideal white Gaussian noise case: the observed *rms* pdf's are somehow wider and centred at higher values. The difference in the median of the theoretical and experimental distributions is easily interpreted as our data still having a larger noise than that expected from instrument noise alone. The higher spread and asymmetry of the experimental distributions can be due to several reasons such as correlations still present in our data thus decreasing the effective number of degrees of freedom or the data not being correctly described by a multivariate Gaussian. In chapter 7 we will apply a K-S analysis to test this last possibility on the data at 4 minutes.

6.3.2 Comparing Power Spectra of Data Before and After Cleaning the Data

The efficiency of the atmospheric reduction process is best demonstrated by looking at the power spectra of the data before and after its application. In figure 26 we show the power spectra of both demodulations and for channels 1, 2 and 3 for a typical night before and after cleaning. This figure corresponds to the same data as in figures 19 and 18. The reduction in the noise level is evident from these plots, so that the corrected Ch 1 and Ch 2 in both demodulations approach the levels expected from instrument noise. We also notice the flattening, approaching the ideal behavior of white noise. For channel 3 there is also an overall decrement in the power spectra of both demodulations indicating that a substantial fraction of the atmospheric noise has been

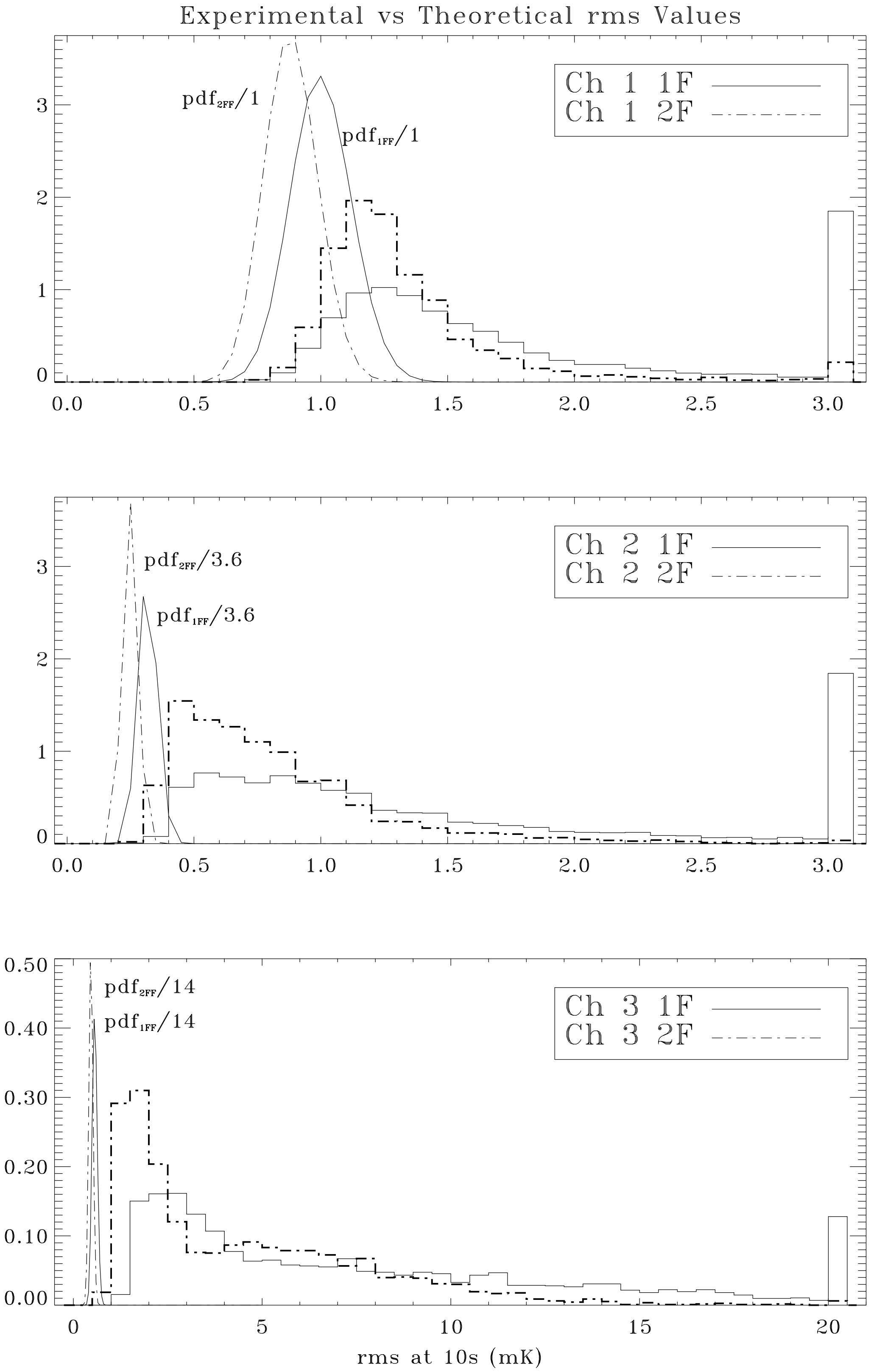

Figure 25: Distribution of the *rms* values for both demodulations and all cleaned channels. The *rms* temperatures along the x-axis refer to thermodynamic temperatures. The theoretical pdf's for uncorrelated Gaussian noise have been scale by the indicated factors for better display purposes. This figure is to be compared with the equivalent one in chapter 4. Note the height of the last bin in all histograms due to that it contains the contribution of that bin plus all following bins.

Table 16: Noise Spectrum ($mK\ s^{1/2}$) Before And After Applying Atmospheric Subtraction.

Channel	1F Out-Phase 1Hz	1F Out-Phase 0.001 Hz	1F In -Phase 0.001 Hz	1F In -Phase 0.001 Hz CLEANED
1	4.8±0.4	6.9±0.6	52±5	8.1±1.0
2	1.13±0.10	1.87±0.17	115±10	3.9±0.5
3	1.99±0.18	3.6±0.3	570±50	20.0±2.3
4	1.20±0.11	18.9±1.7	750±60	
Channel	**2F Out-Phase 1 Hz**	**2F Out-Phase 0.001 Hz**	**2F In-Phase 0.001 Hz**	**2F In-Phase 0.001 Hz CLEANED**
1	3.6±0.3	6.7±0.6	8.8±0.7	6.1±0.7
2	1.04±0.11	3.5±0.4	12.3±1.1	3.3±0.4
3	1.81±0.17	16.0±1.5	55±5	12.7±1.5
4	1.07±0.10	27.6±2.6	94±8	

subtracted. However, the levels of the cleaned data for channel 3 still show residual atmospheric contamination. In table 16 we give the values attained by the noise spectrum in the in-phase components at different frequencies and for both demodulations before and after cleaning for the same observing night as in figure 26. The corresponding values are also given for the out-phase component spectra. At low frequencies (i.e 0.001 Hz) where atmospheric effects are more evident the cleaned file exhibits lower values of the noise spectra than before cleaning; a good indication that most of the atmospheric noise has been removed. Further, this value approaches the values attained in the out-phase components containing small amounts of atmospheric noise due to the leakage during the demodulation.

6.3.3 Recovery of Galactic Plane Crossings

Another check of the performance is the recovery of the Galactic Plane (GP) crossing. The introduction of a factor $\rho_{i4} \neq 1$ to recover the GP explicitly assumes perfect spatial correlation of this signal as seen by channel i and channel 4. This is a very good approximation for channels 2, 3 and 4 where the bulk of the Galactic emission is due to dust emission. The estimated GP crossings in channel 2 1F demodulation (2F demodulation) is 99% (96%) correlated with channel 4, while the estimation of the GP in channel 3 1F demodulation (2F demodulation) attains a 100% (100%) correlation with respect to the GP seen by channel 4. For channel 1 the contributions from dust and free-free emission are comparable, the latter slightly more important. Furthermore, the free-free template (1420 MHz map) and the dust template (240 μm DIRBE map) show a relative slight displacement in the position of the GP at $\delta = 40°$, thus lowering the correlation between channel

1 and channel 4 down to 93% and 72% for the 1F and 2F data respectively. In figure 27 we show the predicted Galactic Plane crossings superimposed on our measurements for channels 1, 2 and 3 and both 1F and 2F demodulations. As discussed in chapter 5 (section 5.2.2), we have considered the dust model in [16], with the ρ_{i4} factors listed in table 17. We have also tried several different Galactic emission models in the literature and have checked that, while the absolute amplitudes in each channel depend strongly on the model used, their ratios are quite stable and so is the parameter ρ_{i4} as can be seen in table 17. The slight differences between the ρ_{i4} factors for the 1F and 2F demodulations are not relevant, except for channel 1. This is a direct consequence of the above mentioned displacements between the contributions generating the GP in channel 1. Using ρ'_{i4} in equation (29) instead of ρ_{i4} results in an amplification/attenuation of the restored GP given by:

$$\Gamma_i = \frac{f_i/c_i - \alpha_i \cdot f_4/(c_4 \cdot \rho_{i4})}{f_i/c_i - \alpha_i \cdot f_4/(c_4 \cdot \rho'_{i4})} \tag{32}$$

Table 17: Values Of ρ_{i4} For The Models Under Consideration.

		1F DEMODULATION			1F DEMODULATION		
Model	Reference	ρ_{14}	ρ_{24}	ρ_{34}	ρ_{14}	ρ_{24}	ρ_{34}
1	1	0.1167	0.1515	0.6458	0.1567	0.1533	0.6452
2	1	0.1249	0.1533	0.6453	0.1750	0.1551	0.6446
3	3	0.1292	0.1786	0.6724	0.1458	0.1787	0.6720
4	3	0.1291	0.1720	0.6624	0.1505	0.1720	0.6618
5	4	0.1233	0.1528	0.6454	0.1725	0.1546	0.6448
6	5	0.1229	0.1859	0.6778	0.1273	0.1851	0.6775
7	6	0.1147	0.1555	0.6511	0.1397	0.1556	0.6506
8	7	0.1137	0.1780	0.6739	0.1178	0.1773	0.6736
9	8	0.1195	0.1788	0.6723	0.1269	0.1779	0.6719
10	9	0.1386	0.2229	0.7063	0.1379	0.2224	0.7061
11	1 0	0.1552	0.1654	0.6438	0.1678	0.2105	0.6427
12	1 1	0.1299	0.1748	0.6649	0.1464	0.1749	0.6644

(1) Boulanger *et al.* 1996; (2) Reach *et al.* 1995; (3) Wright *et al.* 1991; (4) Bersanelli *et al.* 1995; (5) Davies *et al.* 1996a;(6) Kogut *et al.* 1996a; (7) Kogut *et al.* 1996b; (8) de Bernardis *et al.* 1991; (9) Banday & Wolfendale 1991; (10) Page *et al.* 1990; (11) Fischer *et al.* 1995.

The extreme values of Γ_i obtained when using the ρ_{i4} values obtained from the models described in table 12 are 0.6 and 1.2. In figure 28 we show the evolution of the parameters ρ_{i4} for both demodulations in a much wider range than that allowed by the models considered in the literature. The shaded regions represent the $\pm 2\sigma$ levels computed from the sample of Γ_i values from each of the scans considered in this analysis. In view of these results we do not expect big changes in the amplitude of the restored GP due to the change of dust model used to estimate the values of the ρ_{i4} factors. The general agreement between the predictions and our measurements constitutes probably the most important check on the performance of our system and method.

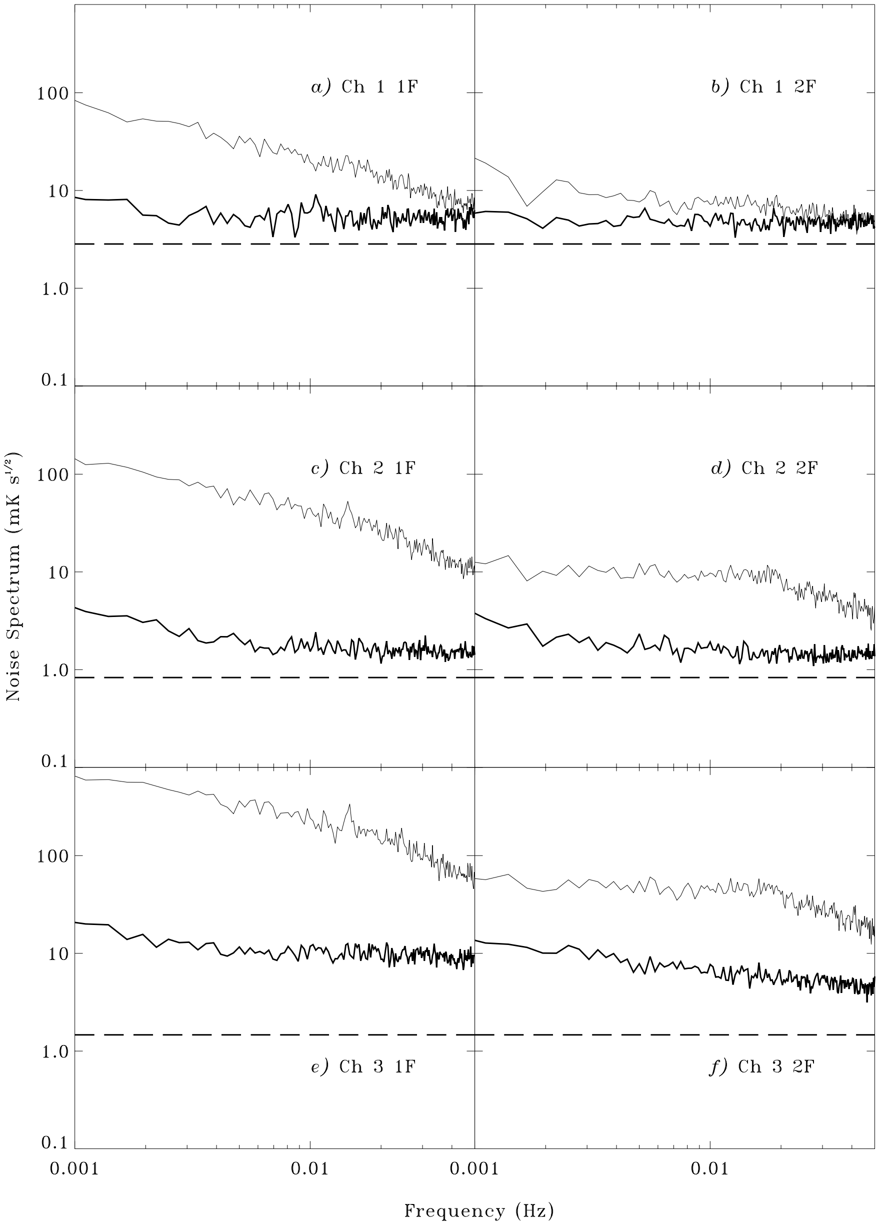

Figure 26: Power spectra of a typical night of observation in thermodynamic temperature at 10s before (thin line) and after (bold line) applying the cleaning technique. The dashed lines represent the upper limits to the instrument noise as estimated in chapter 3 (section 3.4). Temperatures are expressed in thermodynamic units.

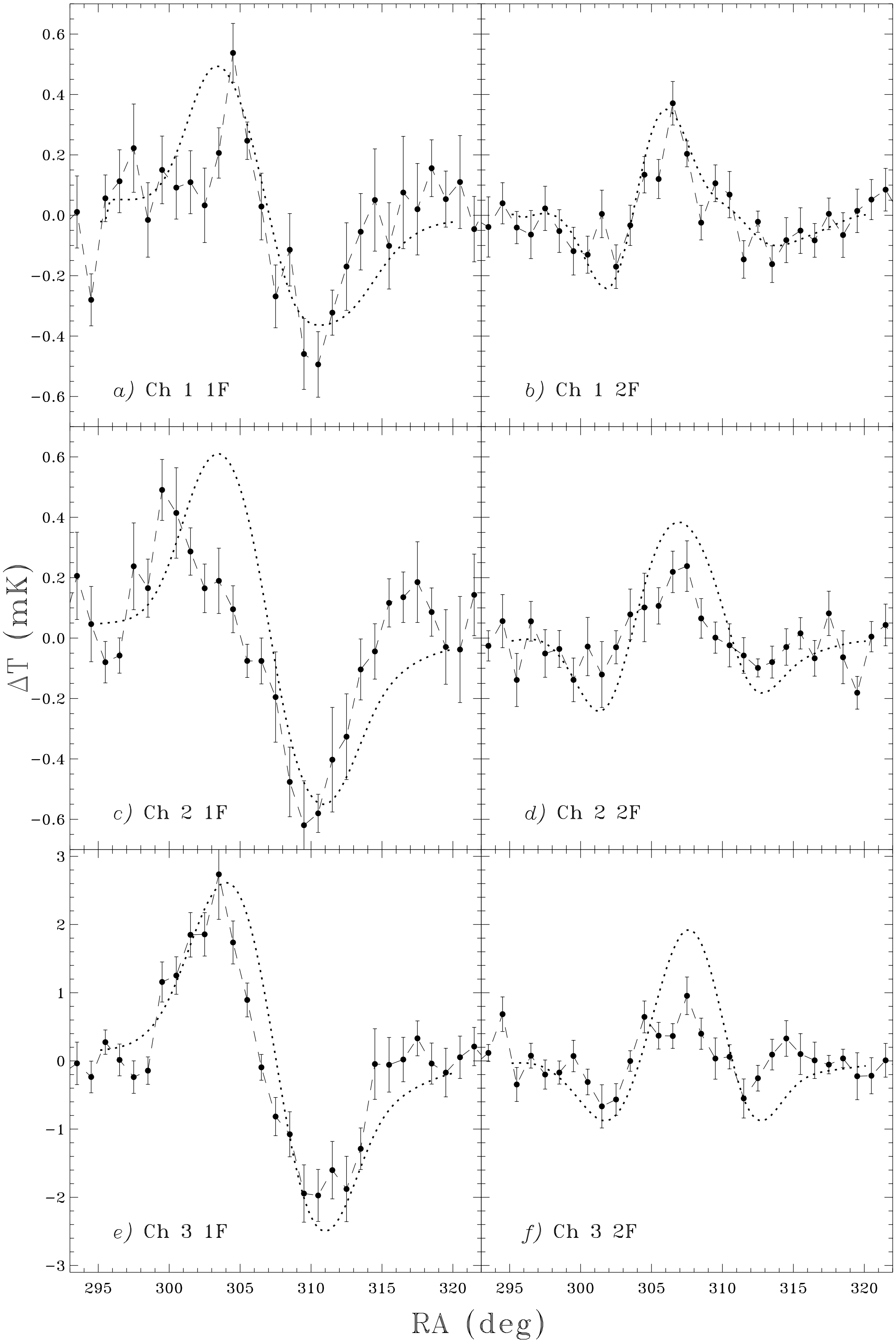

Figure 27: Recovery of the Galactic Plane crossing in all cleaned channels and both demodulations. Superimposed we show the predictions as dot lines. Temperatures along the y-axis refer to thermodynamic units.

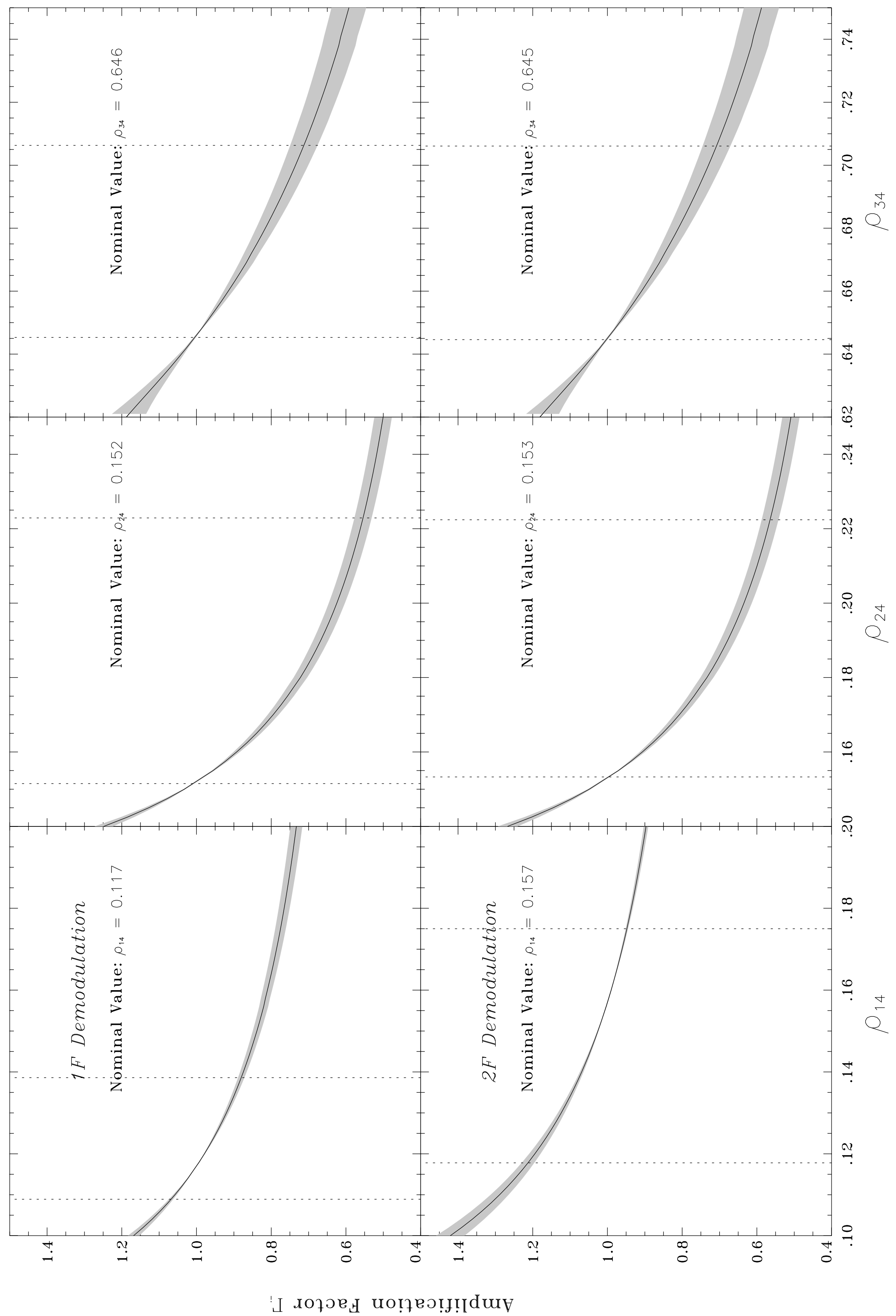

Figure 28: Curves showing the amplification to be applied to the recovered Galactic planes in channel i if a change on the parameter ρ_{i4} is made. Vertical dotted lines indicate the region where all considered models lie. Shaded regions mark the $\pm 2\sigma$ levels computed as indicated in the text.

Chapter 7

Statistical Analysis

7.1 Building the Likelihood Function

We have analyzed those sections of data satisfying two requirements. First, the data must correspond to $b < -15$ (RA_1 section) or to $b > +15$ (RA_2 section) so that we are excluding the region at low Galactic latitude where significant Galactic contamination is expected. Second, the number of points used must be as large as possible in order to reduce statistical fluctuations. It is this second requirement the responsible for the different RA ranges (columns 1 and 5 in table 18) over which each final data set spans as the number of points generating each bin (and in consequence the associated error bars) is not uniform along the data set nor between different channels/harmonics. This is due to the fact that the different editions performed consider only the channel in question (and the monitor channel in the cleaning technique) without taking care on other channels/harmonic. We have required a minimum of $n_i = 6$ in equations (30) and (31), except for channels 1 and 2 in the 2F demodulation where the higher number of used scans allows to increase this threshold, without discarding relevant RA sections, up to 9 and 8 points respectively. In all cases the number of points used to form the final data bins is large enough to allow for a Kolmogorov-Smirnov (KS) test. We have applied this test to all points from independent nights of observation falling in the same bin of any of the final data sets depicted in figure 24. The results of these KS tests are shown in figure 29, where the output of the KS test is 1-significance of the test. In this way, values close to 0 mean that the the cumulative distribution of the data is significantly different from that being compared: in our case we are comparing with a Gaussian pdf with the same values for the mean and σ as those in the data. The results of these tests indicate that our data are compatible with a Gaussian distribution.

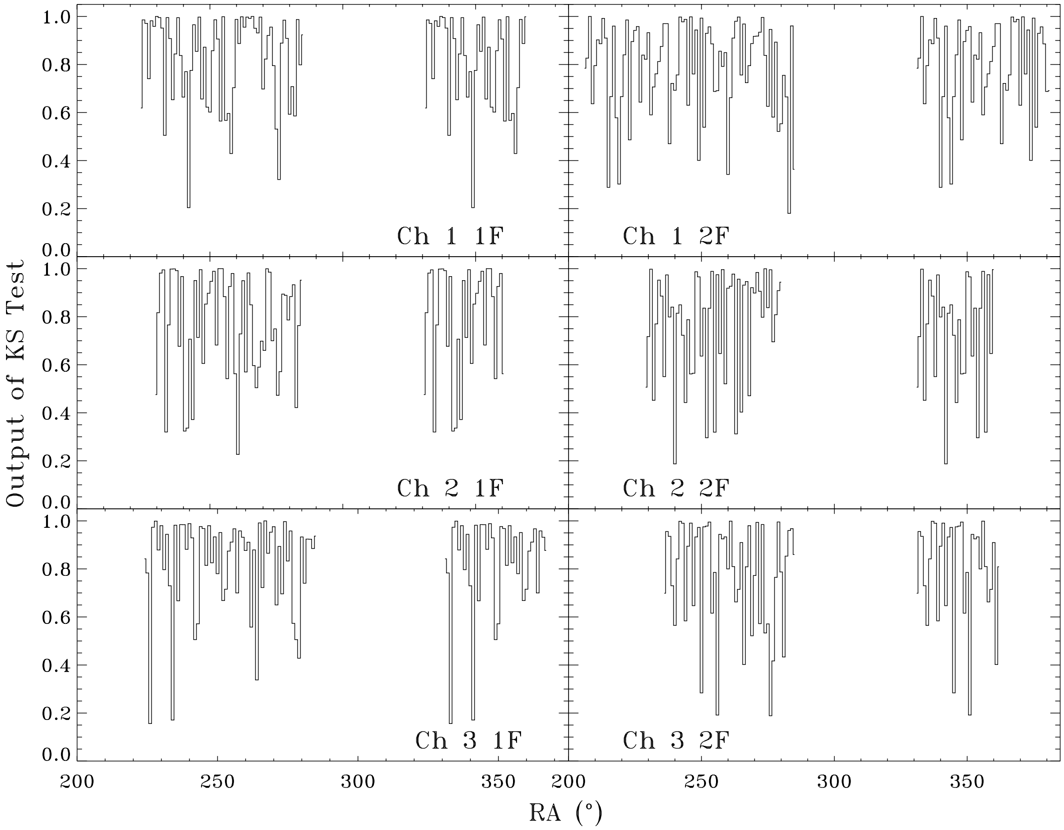

Figure 29: Applying the Kolmogorov-Smirnov test to the data generating the stacked data sets to test if they significantly differ from being drawn from a Gaussian distribution.

Therefore, from now on we will explicitly assume that our data are consistent with being drawn from a multivariate Gaussian distribution, characterized by a zero vector of mean values and a covariance matrix **V**. Under these circumstances, the likelihood function for a our data can be written as:

$$\mathcal{L} \propto \frac{1}{|\mathbf{V}|^{1/2}} \exp(-\frac{1}{2}\,\vec{x}^T\,\mathbf{V}^{-1}\,\vec{x}) \tag{33}$$

where $\vec{x}$ is the data vector and $|\mathbf{V}|$ denotes the determinant of **V**. There are two independent contributions to the covariance matrix so that $\mathbf{V} = \mathbf{V}_T + \mathbf{V}_D$, where $\mathbf{V}_T$ corresponds to the correlations between bins according to the model we are testing and shows dependence on the parameters to be estimated, and $\mathbf{V}_D$ is the data covariance matrix computed directly from the data. We compute the elements ij of $\mathbf{V}_T$ by assuming an intrinsic Gaussian autocorrelation function (GACF): $\mathbf{V}_{intr}(\theta_{ij}) = C_0 \exp(-\theta_{ij}^2/(2\theta_c^2))$ where θ_{ij} is the angular separation between bins i and j, θ_c is the coherence angle, the angle of maximum sensitivity for each experimental configuration: $\theta_c = 2.17^\circ$ and $\theta_c = 1.42^\circ$ for the 1F and 2F data respectively and $C_0^{1/2}$ is the parameter to be estimated. Then we also have to consider the effects introduced by the finite width of the beam and the observing strategy. After convolving with the combination of Gaussian beams reproducing our instrumental responses (see chapter 2, section 2.2), we obtain that the elements (i,j) of the matrices $\mathbf{V}_{T,1F}$ and $\mathbf{V}_{T,2F}$, for the 1F and 2F demodulation respectively, are given by:

$$\begin{aligned} \mathbf{V}_{T,1F}(i,j) \;=\; & \aleph_{1F}^2 \times [2 \cdot C_M(\theta_{ij};\sigma_\alpha,\sigma_\alpha,\sigma_\delta) \;-\; C_M(\theta_{ij}+\beta;\sigma_\alpha,\sigma_\alpha,\sigma_\delta) \;- \\ & C_M(\theta_{ij}-\beta;\sigma_\alpha,\sigma_\alpha,\sigma_\delta)] \end{aligned} \tag{34}$$

$$\begin{aligned} \mathbf{V}_{T,2F}(i,j) \;=\; & \aleph_{2F}^2 \times [C_M(\theta_{ij};\sigma_c,\sigma_c,\sigma_\delta) \;-\; C_M(\theta_{ij}+\beta;\sigma_c,\sigma_l,\sigma_\delta) \;+ \\ & \frac{1}{2}C_M(\theta_{ij};\sigma_l,\sigma_l,\sigma_\delta) - \; C_M(\theta_{ij}-\beta;\sigma_c,\sigma_l,\sigma_\delta) \;+ \\ & \frac{1}{4}(C_M(\theta_{ij}+2\beta;\sigma_c,\sigma_l,\sigma_\delta) \;+\; C_M(\theta_{ij}+2\beta;\sigma_c,\sigma_l,\sigma_\delta))] \end{aligned} \tag{35}$$

Table 18: Basic Statistic Figures Of The Final Data Sets.

	RA_1				RA_2			
Channel	Range (deg)	Number of Points	Mean σ (μK)	Mean rms (μK)	Range (deg)	Number of Points	Mean σ (μK)	Mean rms (μK)
				1F DEMODULATION				
1	[224,285]	7.9	130.6	134.3	[331,369]	10.8	103.1	123.7
2	[230,285]	8.3	118.9	157.9	[331,361]	7.4	113.2	110.6
3	[224,285]	8.8	312.6	340.5	[331,367]	8.7	310.6	443.6
				2F DEMODULATION				
1	[206,285]	12.6	74.7	62.5	[331,381]	13.2	74.1	74.4
2	[229,285]	9.1	68.5	71.0	[331,360]	9.5	53.3	58.5
3	[236,285]	8.3	236.4	197.9	[331,362]	9.5	187.7	204.7

Mean σ refers to the mean error bar associated to each in the final data set.
Mean rms is the weighted rms along the indicated RA range

where $C_M(\theta;\sigma_c,\sigma_l,\sigma_\delta) = C_0\theta_c^2/\sqrt{(\theta_c^2+\sigma_c^2+\sigma_l^2)(\theta_c^2+2\sigma_\delta^2)}\exp[-\theta^2/(2(\theta_c^2+\sigma_c^2+\sigma_l^2))]$ and, as obtained in chapter 2, $(\sigma_\alpha,\sigma_\delta,\beta,\aleph_{1F}) = (1.^\circ 03, 0.^\circ 86, 2.^\circ 38, 1.024)$ and $(\sigma_c,\sigma_l,\sigma_\delta,\beta,\aleph_{2F}) = (1.^\circ 56, 0.^\circ 89, 0.^\circ 86, 2.^\circ 40, 1.677)$ for the 1F and 2F demodulation respectively.

In a Bayesian interpretation with uniform prior, the likelihood ($\mathcal{L}$) as a function of the positive definite parameter ϕ is directly proportional to the probability distribution function of ϕ. Then the best estimation of ϕ is that value for which $\mathcal{L}$ is maximum while confidence levels $[\phi_1, \phi_2]$ to a C% level have been computing by requiring $\mathcal{L}(\phi_1) = \mathcal{L}(\phi_2)$ and

$$\frac{\int_{\phi_1}^{\phi_2} \mathcal{L}(\phi)\, d\phi}{\int_0^{\infty} \mathcal{L}(\phi)\, d\phi} = \frac{C}{100} \tag{36}$$

7.2 Likelihood Analysis on Single Channels

In table 19 we give the results of the likelihood analysis when applied individually to each channel and demodulation on each range (RA_1 or RA_2) and on the total data set (RA_1 + RA_2), each of these ranges given in table 19. In this and following tables detections are given to a 68% CL, and upper limits to a 95% CL. A claim of detection is made whenever the lower limit of the confidence interval at 68% CL is not zero, otherwise we quote the upper limit at 95% CL. In all cases the values obtained in all these RA ranges are consistent with the presence of a common signal.

For channel 2 at 1F demodulation the results between RA_1 and RA_2 are still marginally consistent, but the result in the RA_1 section shows a strong dependence on the choice of individual nights to generate the final data set. Accordingly in what follows we will only consider the RA_2 section for channel 2 at 1F.

For channels 1 and 2, in all valid ranges and in both demodulations, the signals detected are consistent between them and with values of $\sim 100\mu$K. These values are consistent with our previous results reported in [100], where we concluded that the slight excess of signal seen in channel 2 with respect to that obtained in channel 1 may indicate the presence of some residual levels of atmospheric noise at the same level as the expected CMB signal.

The results obtained for channel 3 at both demodulations clearly indicate that it is still affected by important atmospheric residuals: CMB signal does not scale with frequency and our estimated signals due to diffuse Galactic contamination at channel 3 amount to $C_{0,Gal}^{1/2} < 35\mu K$, a too huge difference to be caused by the uncertainties in the Galactic estimation procedure. Another conflicting result is that obtained for Ch 2 1F in RA_1, marginally consistent with the obtained value in RA_2, but showing a too big dependence in the choice of individual scans to generate the final data set. Therefore we will not take this value as representative of the signal detected. It is clear that the most stringent limits on the detected signal come from the combined analysis of the two sections of data at the same time (RA_1 + RA_2).

Table 19: Likelihood Results On Individual Data Sets. Values In μK CMB.

	1F DEMODULATION			1F DEMODULATION		
Channel	$(C_0)^{1/2}$ RA_1	$(C_0)^{1/2}$ RA_2	$(C_0)^{1/2}$ RA_1+RA_2	$(C_0)^{1/2}$ RA_1	$(C_0)^{1/2}$ RA_2	$(C_0)^{1/2}$ RA_1+RA_2
1	130^{+63}_{-52}	124^{+71}_{-58}	127^{+44}_{-37}	< 123	99^{+53}_{-45}	71^{+34}_{-37}
2	283^{+83}_{-62}	155^{+83}_{-58}	239^{+58}_{-45}	91^{+47}_{-43}	132^{+77}_{-56}	106^{+37}_{-33}
3	764^{+219}_{-169}	626^{+260}_{-176}	711^{+168}_{-135}	235^{+158}_{-181}	591^{+284}_{-240}	373^{+169}_{-163}

Note.- The stated confidence intervals do not include calibration uncertainties.

7.3 Joint Multi-Channel Likelihood Analysis

The joint analysis of all three channels allows us to estimate the most likely signal which is common to all of our frequencies, such as CMB anisotropy. To estimate the correlation between channels we have computed the cross-correlation function between sections of data at 10 s which overlap in the same nights in channels i and j. We make use of the generalized Wiener-Khinchin relations for stationary processes to obtain one cross-correlation curve per night. The average of these curves are plotted in figure 30. We observe that the cross-correlation becomes negligible at scales smaller than our binning in the final data sets, being only significantly different from zero at zero-lags as indicated in table 21 where we give the cross-correlation values between all possible combinations of channels and demodulations for lags in the range ±4 bins in the final data sets (i.e. ±16 minutes in RA). This cross-correlation at zero-lag enhances the diagonal terms in the sub-matrices which take into account the correlation between different channels in the covariance matrix $\mathbf{V}_D$. This effect has been analyzed and discussed in detail by [51], concluding that the net effect is an increase of the error bars as compared with the case where not such correlations are present. In table 20 we present the results from the joint analysis of any two channels and all three channels for each demodulation. These results have been obtained by using the whole data set except for those involving channel 2 at 1F for which only the RA_2 section of the data set was used.

Table 20: Joint Likelihood Results. Values in μK.

	1F DEMODULATION	2F DEMODULATION
Channel	$(C_0)^{1/2}$ (μK)	$(C_0)^{1/2}$ (μK)
1×2	129^{+41}_{-35}	69^{+27}_{-25}
1×3	151^{+44}_{-37}	72^{+35}_{-37}
2×3	164^{+89}_{-60}	107^{+37}_{-34}
$1 \times 2 \times 3$	150^{+40}_{-34}	72^{+26}_{-24}

Note.- The stated confidence intervals do not include calibration uncertainties.

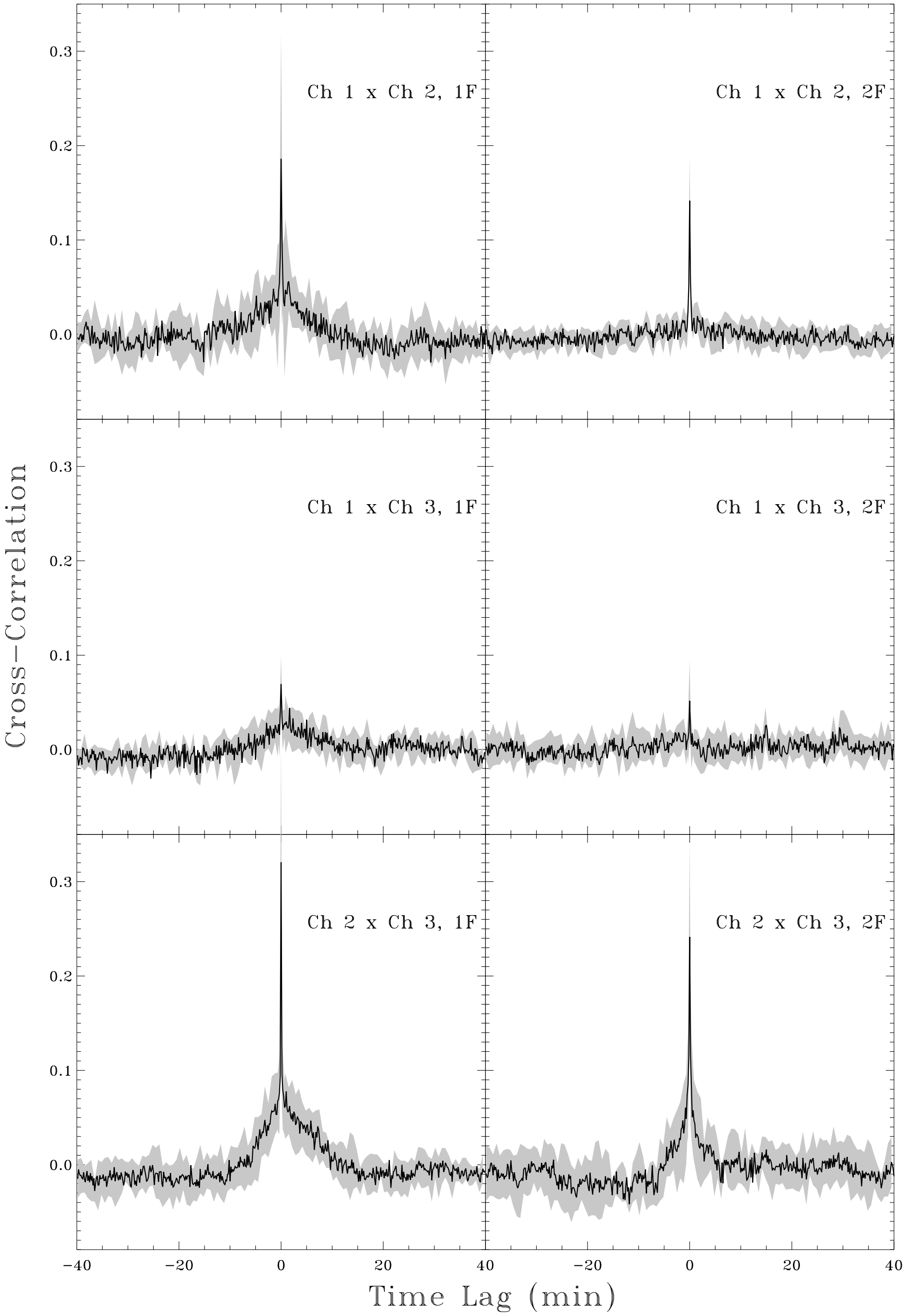

Figure 30: Average cross-correlation curves between overlapping sections of individual nights at any two channels within the same demodulation. These curves have been obtained using only the overlapping section between those scans used to generate the final data sets. The shaded regions represent the $\pm 2\sigma$ levels.

The analysis on any combination of 2 channels indicates the presence of common signal, which for the 1F demodulation is $C_0^{1/2} \sim 150\mu$K and $\sim 75\mu$K for the 2F demodulation. Although being completely consistent, these figures must be viewed with caution: the signal monotonically increases as we increase the frequencies of the channels being combined. This behavior again indicates the higher level of contamination in channel 3 for both demodulations.

Table 21: Cross-Correlations Between Channels And Demodulations.

Lag (min)	$Ch1_{1F} \times Ch1_{1F}$	$Ch2_{1F} \times Ch2_{1F}$	$Ch3_{1F} \times Ch3_{1F}$	$Ch1_{2F} \times Ch1_{2F}$	$Ch2_{2F} \times Ch2_{2F}$	$Ch3_{2F} \times Ch3_{2F}$
0	100.0±0.0	100.0±0.0	100.0±0.0	100.0±0.0	100.0±0.0	100.0±0.0
4	2.0±0.6	10.4±2.0	5.4±1.4	1.2±0.6	3.9±1.5	2.5±0.7
8	-0.9±0.7	4.6±1.6	3.7±1.0	0.3±0.5	3.1±1.1	-0.9±1.0
12	-0.1±0.8	2.7±1.0	1.9±0.6	0.5±0.5	1.4±0.9	0.8±0.8
16	-0.9±0.7	1.6±1.3	0.2±0.9	-0.3±0.5	-0.2±1.0	1.5±0.8
Lag (min)	$Ch1_{1F} \times Ch2_{1F}$	$Ch1_{1F} \times Ch3_{1F}$	$Ch2_{1F} \times Ch3_{1F}$	$Ch1_{2F} \times Ch2_{2F}$	$Ch1_{2F} \times Ch3_{2F}$	$Ch2_{2F} \times Ch3_{2F}$
-16	-1.5± 0.9	-0.3±1.1	-2.4±0.6	-0.8±0.5	-0.4±0.9	-1.4±1.4
-12	1.5± 1.3	-1.5±0.9	-1.8±0.6	0.9±1.1	0.1±0.9	-2.4±0.1
-8	1.1± 1.4	0.6±0.5	0.8±1.1	0.2±0.7	0.1±0.7	-1.7±1.1
-4	3.4± 1.4	1.5±0.9	2.8±1.4	-0.0±0.6	0.6±0.7	1.7±1.1
0	19 ± 7	8.5±1.3	31.3±6	14.9±2.6	4.9±1.0	26 ±5.0
4	1.6± 1.1	2.8±1.6	4.0±1.0	0.1±0.9	0.3±1.1	2.0±1.3
8	0.0± 1.7	-0.1±1.1	1.3±0.9	1.1±0.7	1.5±0.6	-0.9±1.3
12	-0.6± 1.7	-0.2±1.0	-0.9±1.3	0.6±0.7	1.7±0.8	-1.3±1.4
16	-2.0± 1.0	-0.1±0.8	-1.2±1.2	0.6±0.6	0.0±0.7	0.2±0.7
Lag (min)	$Ch1_{1F} \times Ch1_{2F}$	$Ch2_{1F} \times Ch2_{2F}$	$Ch3_{1F} \times Ch3_{2F}$			
-16	0.1± 0.8	-2.0±0.9	-2.0±0.7			
-12	0.2± 0.7	-0.6±0.8	-0.7±0.7			
-8	-0.9± 0.9	-1.0±1.5	-1.3±0.8			
-4	-0.6± 0.7	-1.8±1.5	-0.4±0.9			
0	-1.2± 1.2	-12 ±4	-2 ±3.0			
4	0.3± 0.8	-1.1±1.0	0.8±1.3			
8	0.6± 0.6	-0.1±1.5	1.1±1.0			
12	-1.4± 0.4	-0.7±1.2	0.2±1.1			
16	-0.3± 0.8	-0.1±1.1	0.6±1.2			
Lag (min)	$Ch1_{1F} \times Ch2_{2F}$	$Ch1_{1F} \times Ch3_{2F}$	$Ch1_{2F} \times Ch2_{1F}$	$Ch1_{2F} \times Ch3_{1F}$	$Ch2_{1F} \times Ch3_{2F}$	$Ch2_{2F} \times Ch3_{1F}$
-16	-2.0± 0.9	-0.9±0.9	0.2±0.7	0.9±0.6	-2.2±1.6	0.1±0.6
-12	-0.8± 1.1	0.8±1.3	1.6±0.6	1.0±1.1	-1.9±2.3	1.4±1.2
-8	-1.2± 0.8	-1.7±1.1	1.4±0.6	0.1±0.8	-2.2±1.5	0.9±0.8
-4	-1.2± 1.8	-2.2±0.9	2.9±0.6	-0.3±0.6	-1.3±1.2	1.4±0.0
0	-4.0± 1.5	-0.8±1.0	-1.7±1.1	-2 ±6	-3.3±1.7	-9 ±4
4	1.2± 1.7	-0.1±0.8	-0.5±0.9	-1.4±0.7	-1.9±1.3	-0.7±1.3
8	0.4± 1.9	1.2±1.5	1.0±0.5	-1.3±0.6	-1.7±1.0	-0.3±0.7
12	-0.1± 1.2	0.0±1.6	-1.5±0.7	-0.8±0.6	0.2±1.2	0.1±1.3
16	-0.2± 1.5	-0.2±1.1	-0.4±0.8	-0.2±0.8	0.6±1.0	-1.7±2.0

Finally, we have also considered the case of having a superposition of CMB signal plus a signal with a spectral behavior different from a black-body. In this way we obtain the contamination due to a foreground component which is consistent with the data. We also assume a GACF with the same coherence angle as the CMB signal for the foreground signal in addition to a scaling of the signal with frequency. Thus the foreground signal in channel 1 exhibits an intrinsic ACF $C^{Fgd}_{Ch\ 1}(\theta) = C_{0,Fgd}\exp[-\theta^2/(2\theta_c^2)]$ while channel j ($j = 2, 3$) shows $C^{Fgd}_{Ch\ j}(\theta) = C^{Fgd}_{Ch\ 1}(\theta) \times (\nu_j/\nu_1)^{2n} \times (c_j/c_1)^2$. As in equation (29) c_i ($i = 1, 2, 3$) is the Rayleigh-Jeans to thermodynamic conversion factor; $\nu_1 = 95.1$ GHz, $\nu_2 = 169.0$ GHz and $\nu_3 = 243.5$ GHz the frequencies for channels 1, 2 and 3 respectively. By setting the value of n to the appropriate values we obtain the signal due to any of the foreground contaminants. The likelihood function now becomes a function of two parameters to be estimated: $\mathcal{L} = \mathcal{L}(C^{1/2}_{0,cmb}, C^{1/2}_{0,Fgd})$. Since, *a priori*, we do not have any information about either of them we obtain the probability distribution function of $C^{1/2}_{0,cmb}$ by marginalizing with respect to $C^{1/2}_{0,Fgd}$ and vice-versa. In table 22 we present the results of this analysis for different values of the spectral index n covering the ranges expected for dust, atmospheric, synchrotron and free-free emission. In figure 31 we show the contour plots for the spectral indexes n = 2.0, 0.0, -2.1 and -3.0, corresponding to dust, a simple atmospheric model, free-free and synchrotron emission in Rayleigh-Jeans approximation. The data are then converted into thermodynamic units in the plots. Small departures from these nominal values yield essentially the same results as seen in table 22.

Table 22: Likelihood Results Allowing A Foreground Component. Values In μK CMB.

		1F DEMODULATION		2F DEMODULATION	
n	Foreground	$C^{1/2}_{0,cmb}$	$C^{1/2}_{0,Fgd}$	$C^{1/2}_{0,cmb}$	$C^{1/2}_{0,Fgd}$ (μK)
+2.0	DUST	128^{+42}_{-32}	38^{+8}_{-6}	72^{+26}_{-22}	< 6
+1.5	DUST	128^{+42}_{-34}	60^{+14}_{-10}	72^{+26}_{-22}	< 8
+0.4	ATMOSPHERE	147^{+54}_{-38}	150^{+39}_{-27}	72^{+26}_{-22}	< 16
+0.2	ATMOSPHERE	154^{+62}_{-54}	171^{+45}_{-33}	72^{+26}_{-24}	< 18
+0.0	ATMOSPHERE	159^{+69}_{-63}	189^{+54}_{-39}	72^{+26}_{-24}	< 20
-1.8	FREE-FREE	147^{+45}_{-39}	< 177	72^{+26}_{-26}	< 62
-2.1	FREE-FREE	150^{+45}_{-39}	< 189	72^{+26}_{-26}	< 74
-2.4	FREE-FREE	153^{+51}_{-39}	< 201	72^{+26}_{-26}	< 86
-2.7	SYNCHROTRON	153^{+51}_{-39}	< 210	72^{+26}_{-26}	< 96
-3.0	SYNCHROTRON	156^{+51}_{-39}	< 216	72^{+26}_{-28}	< 106
-3.3	SYNCHROTRON	156^{+51}_{-39}	< 222	72^{+26}_{-28}	< 116

The stated confidence intervals do not include calibration uncertainties.

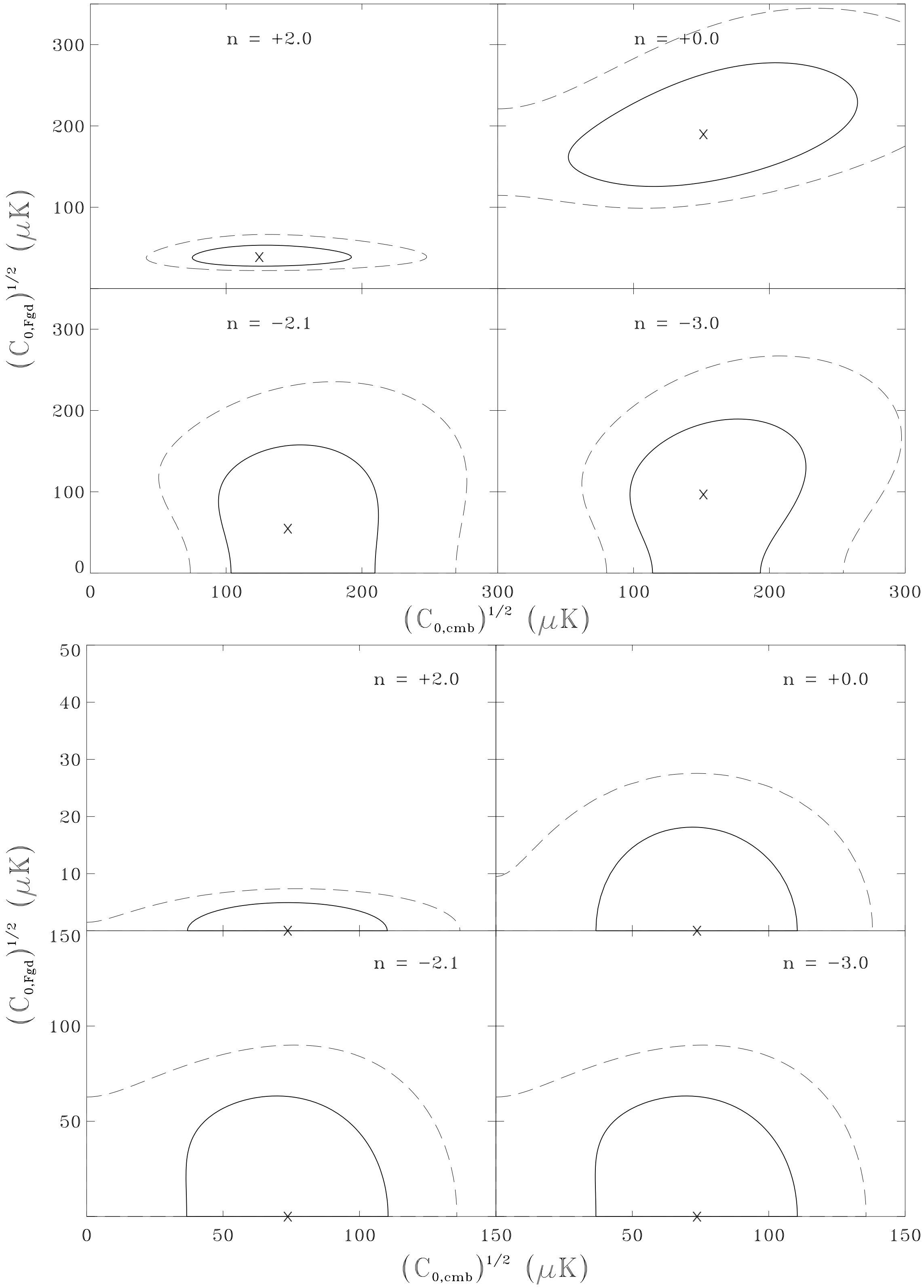

Figure 31: Contour plots of likelihood surface of joint analysis on channels 1, 2 and 3 at 1F demodulation (top) and 2F demodulation (bottom) with a second component other than CMB allowed. The four indices n represent the four relevant foregrounds: dust, atmosphere, free-free and synchrotron emission. Contour levels represent the confidence levels at 68% (solid line) and 95% (dashed line). The X symbol indicates the position of the likelihood surface peak. Temperatures on the axis are in thermodynamic units.

7.4 Discussion of the Likelihood Results

The joint analysis of channels 1, 2 and 3 at the 2F demodulation reveals the presence of a common signal with $C_0^{1/2} = 72^{+26}_{-24}\,\mu$K. The conversion to band power estimates (see Appendix A) yields $\sqrt{\bar{\ell}(\bar{\ell}+1)C_{\bar{\ell}}/(2\pi)} = 55 \pm 17\ \mu K$ at $\bar{\ell} = 53^{+22}_{-15}$ in good agreement with our previous results in [100] ($C_0^{1/2} = 76^{+23}_{-21}\ \mu$K for a GACF or $\sqrt{\bar{\ell}(\bar{\ell}+1)C_{\bar{\ell}}/(2\pi)} = 55 \pm 17\ \mu K$ in the band power estimate notation). At similar angular scales, $\bar{\ell} = 56^{+21}_{-18}$, [90] quote a value of $\sqrt{\bar{\ell}(\bar{\ell}+1)C_{\bar{\ell}}/(2\pi)} = 49^{+19}_{-8}\ \mu K$. In figure 32 the 2F result is shown in conjuction with other anisotropy measurements and the predictions of the Standard CDM model are shown in solid line.

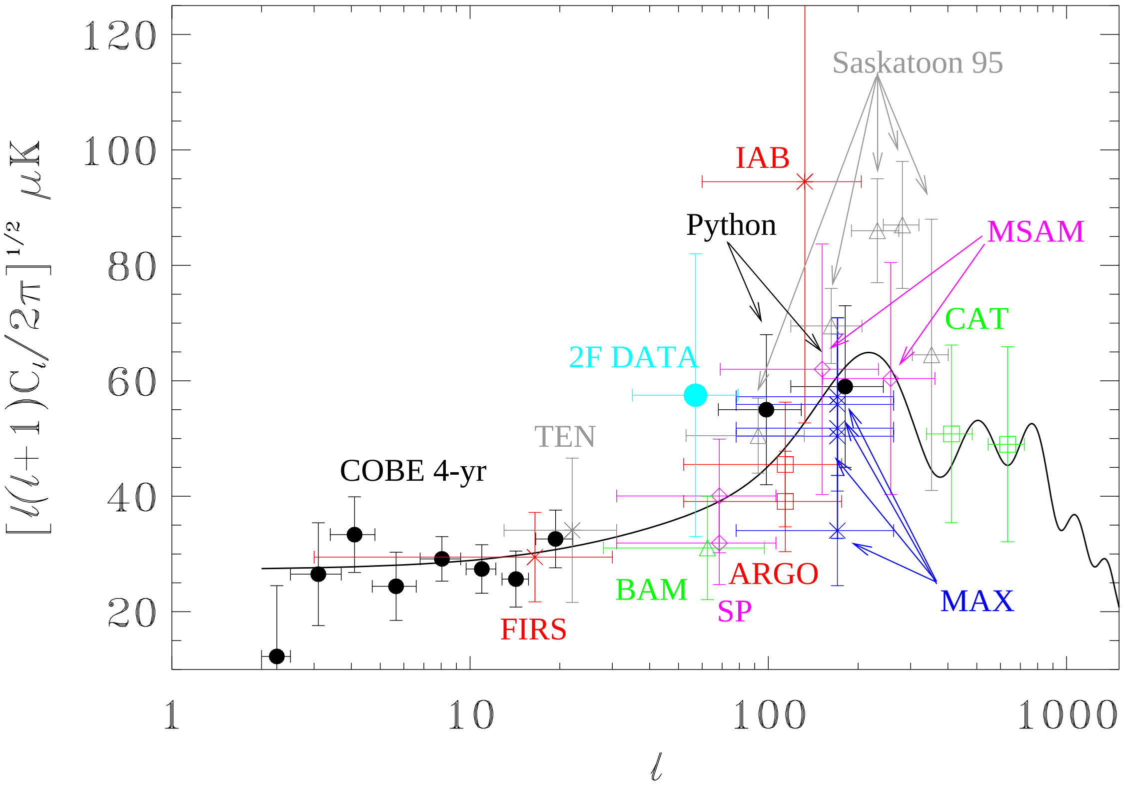

Figure 32: Current Observational Status comparing our measurement of CMB anisotropy at 2F (cyan dot) with those from other experiments. The solid line shows the standard CDM model with the parameters described in main text in chapter 1.

We have also tested the possibility that part of the detected common signal is due to contamination by Galactic foregrounds or residual atmospheric contamination. The analysis confirms that dust can not be responsible of the detected signal ($C_{0,Dust}^{1/2} < 25\ \mu$K), leaving a CMB signal of $C_0^{1/2} = 72^{+26}_{-22}\ \mu$K which corresponds to $\sqrt{\bar{\ell}(\bar{\ell}+1)C_{\bar{\ell}}/(2\pi)} = 55^{+19}_{-16}\ \mu K$. After considering calibration uncertainty as a systematic effect the figures above become $C_0^{1/2} = 72^{+34}_{-28}\ \mu$K and

$\sqrt{\bar{\ell}(\bar{\ell}+1)C_{\bar{\ell}}/(2\pi)} = 55^{+27}_{-22}\ \mu K$. Less conclusive is our analysis when a free-free or synchrotron spectrum is assumed for the contaminant signal. Then we only have vague upper limits for the contaminants which were known in advance from both our estimations and results from the Tenerife experiment when observing at $\delta = 40°$. As indicated in chapter 5, the free-free contamination seen by the Tenerife experiment at 33 GHz is about 4 μK. The extrapolation in frequency renders this source of contamination to values $< 1\mu$K at both demodulations and in all channels. These upper limits are further reduced by the fact that our experiment probes higher values of ℓ's than those probed by the Tenerife experiment, and at high $|b|$ the Galactic power spectrum scales as $C_\ell \propto \ell^{-3}$([135, 70, 46]).

The presence of atmospheric residuals is also tested by allowing for the presence of a signal with a spectral index in antenna temperature of $n = 0., 0.2$ and 0.4. The $n = 0$ case corresponds to the approximate case in which the effective atmospheric temperature is the same in all our channels. The $n = 0.2$ and 0.4 cases allow an increase with frequency of the effective atmospheric temperature. For all the considered n values, the likelihood assigns the bulk of the fluctuations to CMB signal: $C^{1/2}_{0,cmb} = 72^{+26}_{-24}\ \mu$K, $C^{1/2}_{0,atm} < 20\ \mu$K. As shown in table 9, these values are rather insensitive to the exact choice of the spectral index n.

The two-component joint likelihood analysis on the 1F data places the bulk of the signal on the atmospheric component: $C^{1/2}_{0,atm} = 189^{+54}_{-39}\,\mu$K and $C^{1/2}_{0,cmb} = 159^{+69}_{-63}\,\mu$K, which in flat band power estimate becomes $\sqrt{\bar{\ell}(\bar{\ell}+1)C_{\bar{\ell}}/(2\pi)} = 112^{+49}_{-44}\ \mu K$. Treating the calibration uncertainty as a systematic effect, the above results for the CMB component become : $C^{1/2}_{0,cmb} = 159^{+93}_{-87}\,\mu$K and $\sqrt{\bar{\ell}(\bar{\ell}+1)C_{\bar{\ell}}/(2\pi)} = 112^{+65}_{-57}\ \mu K$. Having a large atmospheric signal in our 1F data is expected because the 1F demodulation is known to be less efficient in removing linear gradients in the atmospheric signal. However, a significant fraction of the signal is projected to the CMB component which is marginally consistent with the 2F result. When testing for the presence of Galactic contamination the two-component likelihood analyses yield low significance detection for a dust component, and only upper limits to contamination by free-free or synchrotron emission.

7.5 What Can Be Extracted From the CMB Power Spectrum?

Without entering into too many details, some basic conclusions on some cosmological parameters can be drawn. A proper analysis as the one suggested in references [62, 63, 65] will be needed when good quality data are available. Even so, some authors (see references [78, 109, 56]), have already attempted fits to the data points in order to draw estimates on the most relevant cosmological parameters. The purpose of this section is not to reproduce the analysis of those works, but rather investigate in a very simplistic way how the change in different parameters affects the computed CMB anisotropy power spectrum. This has been using the CMBFAST code [118] to compute angular spectra for different combinations of the cosmological parameters under study.

7.5.1 Varying the value of Ω

Astronomical observations suggest that $\Omega \geq 0.3$, while the most accepted theoretical model predicts a value of 1 for Ω. In this section the value of Ω is changed between these two extremes while the other cosmological parameters are fixed to the following values (see chapter 1 section 3.2 for a brief description): $H_0 = 60\ Km\, s^{-1}\, Mpc^{-1}$, $Y_P = 0.24$, $N_\nu = 3$, $N_{\nu,mass} = 0$, $\Omega_b = 0.07$, $\Omega_\Lambda = \Omega_\nu = 0$, $r = 0$ and $n_S = 1$. Since $\Omega = \Omega_b + \Omega_{CDM} + \Omega_\Lambda + \Omega_\nu$, what we are doing in this section is to change Ω_{CDM}. In all cases primordial adiabatic fluctuations were assumed since isocurvature fluctuations are being progressively discarded as they would involve fluctuations much larger than those observed by current experiments. In figure 33 several power spectra corresponding to different values of Ω are shown in addition to the observational data. When all parameters are held fixed, lowering Ω has the effect of shifting the first Doppler Peak towards higher ℓ-values. As noticed by [63], this behavior is rather insensitive to the values of all other cosmological parameters so that this is a robust method to obtain an estimate of Ω.

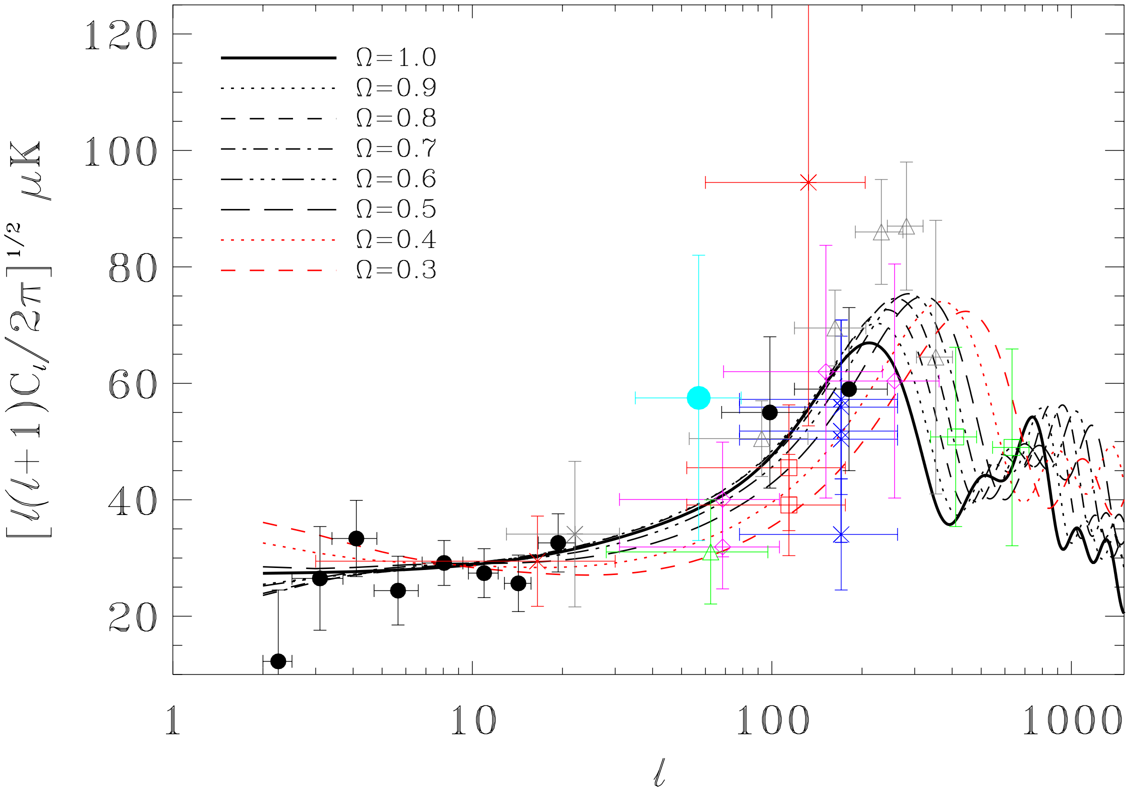

Figure 33: Comparing current observational data with power spectra obtained by fixing all parameters except Ω. The thick dark line shows the prediction from the Standard CDM model.

7.5.2 Varying the value of Λ

An upper bound on the contribution from the cosmological constant Λ is obtained from gravitational-lensing statistics [62] so that $\Lambda \leq 0.5$. Accordingly, the parameter Λ has been allowed to vary in between 0 and 0.5. The net effect of increasing Λ while holding fixed the other parameters is to enhance the height of the first Doppler peak. Such effect is easily seen in figure 34 where all power spectra correspond to flat Universes (i.e $\Omega = 1$) but where Λ takes different values. All other parameters are held fixed to the following values: $H_0 = 60\ Km\, s^{-1}\, Mpc^{-1}$, $Y_P = 0.24$, $N_\nu = 3$, $N_{\nu,mass} = 0$, $\Omega_b = 0.07$, $\Omega_\Lambda = \Omega_\nu = 0$, $r = 0$ and $n_S = 1$ and Ω_{CDM} is varied to always have $\Omega = 1$. As in the previous case, initial perturbations are assumed to be adiabatic with no Gravitational Waves contribution and normalized to COBE 4-year data.

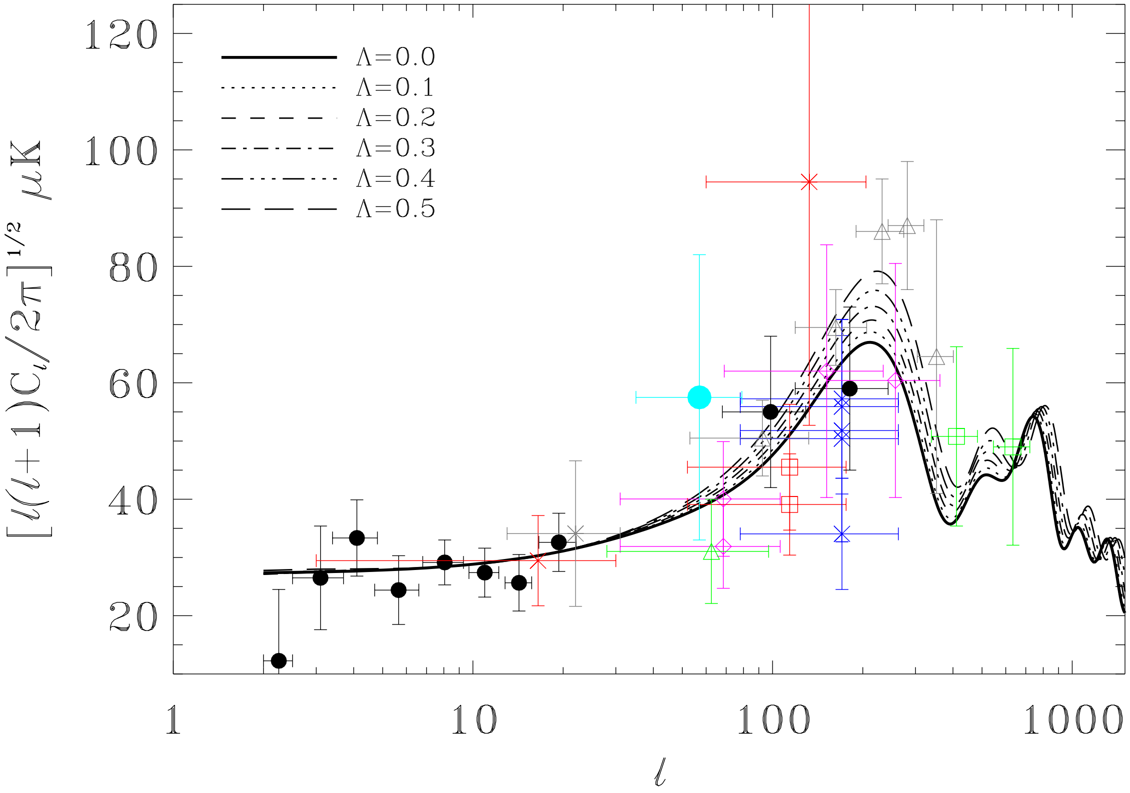

Figure 34: Comparing current observational data with power spectra obtained by fixing all parameters except Λ. The thick dark line shows the prediction from the Standard CDM model.

7.5.3 Varying the value of Ω_b

The combination of the Hubble constant and Ω_b are tightly bounded by the predictions of Standard Big Bang Nucleosynthesis (SBBN) so that: $0.007 \leq \Omega_b h^2 \leq 0.0024$ at 95% CL [23]. SBBN also puts an upper bound on the effective number of family of relativistic neutrinos at the time of nucleosynthesis: $N_\nu < 3.9$. Assuming a value of $h = 0.6$ as the most likely value for the Hubble constant from gravitational lensing studies (e.g see [47] for a recent review on this), we obtain that according to SBBN Ω_b is constrained to vary in the range $0.01 \leq \Omega_b \leq 0.07$. In figure 35 different CMB angular power spectra are shown corresponding to values of Ω_b within the range prescribed by SBBN as well as other values of Ω_b outside that range. The trend in to increase the height of the Doppler peak, so that with the current observational data we see that values $\Omega_b > 0.2$ start having trouble in the frame of the flat universes with adiabatic primordial fluctuations. All curves shown correspond to $\Lambda = 0$ while the rest of the parameters are fixed to the same values as in the previous sections.

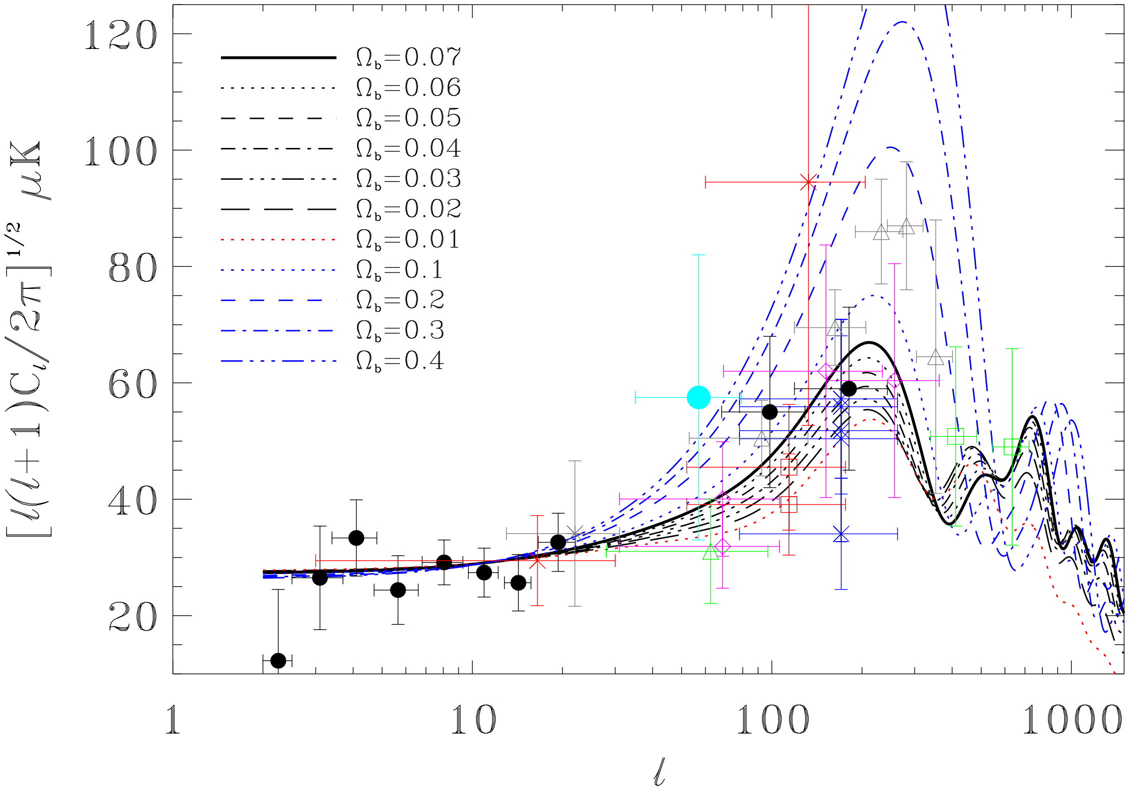

Figure 35: Comparing current observational data with power spectra obtained by fixing all parameters except Ω_b. The thick dark line shows the prediction from the Standard CDM model.

7.5.4 Varying the value of H_0

As seen in figure 36, as h ($h = H_0/(100\ Km\, s^{-1}\, Mpc^{-1})$) increases, the first Doppler peak is slightly shifted towards higher ℓ-values and its amplitude is enhanced. Given the high dispersion of the current data and their associated error bars, at present is not possible to draw any conclusion on h.

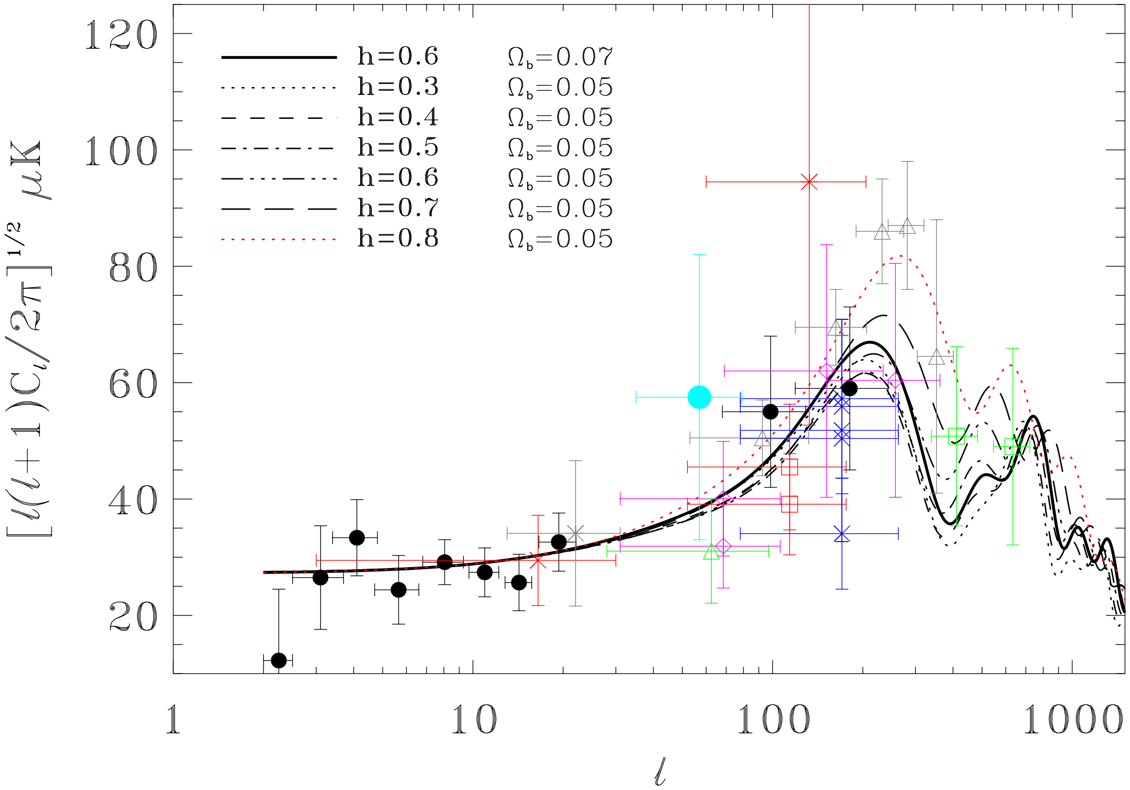

Figure 36: Comparing current observational data with power spectra obtained by fixing all parameters except h. The thick dark line shows the prediction from the Standard CDM model.

7.5.5 CMB anisotropies in BDM models

In general, Baryonic Dark Matter models (BDM) do not fix the value of Ω to be 1 and assume that most of the mass in the Universe is in form of baryonic matter. Tight restrictions are being put on these models as they postulate isocurvature rather than adiabatic fluctuations [145]. As seen in figure 37 for a wide range of conditions for BDM models with isocurvature fluctuations, there is no way to fit the observed CMB anisotropy with these models. Allowing adiabatic fluctuations generates a unique first Doppler peak at higher ℓ-value than that suggested by current observations. Yet, the data exhibit too large error boxes and ruling out BDM models with adiabatic fluctuations is still too premature.

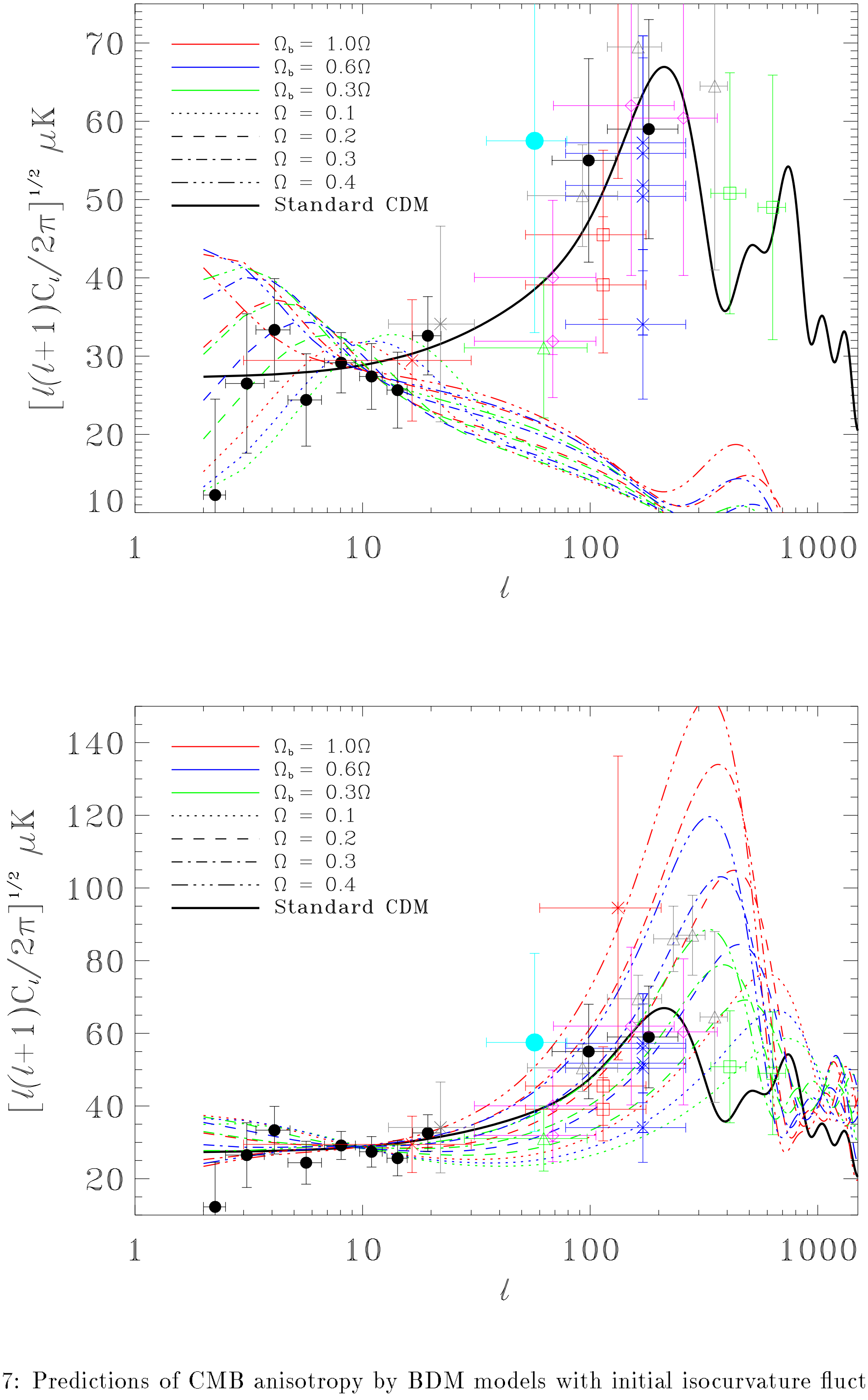

Figure 37: Predictions of CMB anisotropy by BDM models with initial isocurvature fluctuations (top) and initial adiabatic fluctuations (bottom). In both panels the Standard CDM predictions is displayed with a thick dark line.

7.5.6 Conclusions

As seen in the previous sections, different parameters have competing effects on the shape of the angular power spectrum of CMB anisotropies. A proper study needs to consider the joint effect of modifying all parameters and given the large error bars, this seem an extremely difficult task with high chances to yield very poor results. Such statement is supported by the fact that analysis of this kind have already been undertaken by a series of authors [78, 109, 56, 79] either by exploring a given region of the parameter space of a restricted subset of the model parameters or by using analytic approximations to the CDM spectrum with a small number of free parameters. The resulting error bars on the estimates are still very large with [56] yielding a best estimate of $\Omega = 0.7^{+1.0}_{-0.4}$ and $h = 0.3 - 0.5$ for the range of Ω_b values allowed by SBBN. On the other side, [78, 79] estimate $h = 0.30^{+0.18}_{-0.07}$, a very low value inconsistent with the estimates obtained by gravitational lensing. All these works agree in assigning very low confidence levels to models with $\Omega \leq 0.3$ as also indicated in figure 33.

Chapter 8

Conclusions & Future Work

8.1 Conclusions

The most relevant conclusion from this work are summarized in figure 32 in chapter 7 where only our 2F measurement has been added because of our suspicions of the 1F result being still affected by significant atmospheric residuals. In view of this we conclude:

- The sensitivity achieved in the 2F demodulation allows us to identify a common signal between our channels with a value of $C_0^{1/2} = 72^{+26}_{-24}\mu$K corresponding to a band power estimate of $\sqrt{\bar{\ell}(\bar{\ell}+1)C_{\bar{\ell}}/(2\pi)} = 55^{+27}_{-22}\mu K$ at $\bar{\ell} = 53^{+22}_{-15}$ at 68% CL including the systematic effect due to calibration uncertainty. The value for the signal detected in this ℓ-band is in close agreement with the values reported for CMB anisotropy by the experiments Saskatoon and Python and statistically consistent with the detections reported by BAM, SP and ARGO. Despite of the large associated error bar, this measurement indicates the rising of the angular power spectrum of CMB anisotropy as expected if there is a Doppler peak. The presence of such Doppler peak seems to be indicated by the results of the Saskatoon experiment working at higher angular resolution.
- Two alternative arguments (one based on extrapolations from Galactic templates, the other on results from other experiments) allow us to discard a Galactic origin of the detected signal. An extension of the likelihood analysis allowing the presence of a signal with the assumed spectrum for the atmospheric emission also discards the possibility of the signal being caused by correlated atmospheric residuals.
- In all channels the 1F data show an excess of signal with respect to the 2F data. This excess is suspected to be of atmospheric origin: the two-component joint likelihood analysis assigns a portion of the detected signal to CMB fluctuations at a level of $C_0^{1/2} = 159^{+93}_{-87}\mu$K at 68% CL including calibration uncertainty as a systematic effect (or in band power estimate

$\sqrt{\bar{\ell}(\bar{\ell}+1)C_{\bar{\ell}}/(2\pi)} = 112^{+65}_{-57}\,\mu K)$, while the part associated to residual atmospheric noise is $C_0^{1/2} = 189^{+93}_{-87}\,\mu$K. In any case, it should be remarked that our 1F demodulation corresponds to an ℓ-range never before observed.

Another very important conclusion to be drawn from the work done during this thesis concerns the possibility of performing millimetric observations from ground observatories. This work has demonstrated the viability of such observations as long as:

1. These observations are conducted from observing sites with a dry and very stable atmosphere in order to have atmospheric noise as low as possible. Both requirements are satisfied at Observatorio del Teide as demonstrated by the final results from our data.
2. The quality of our data has been influenced by the moderately short period of time over which observations spanned. In view of the high percentage of rejected data, it is clear that longer observing periods are needed. In addition, these observations should be conducted at those months at which the water vapor in the atmosphere is minimum while the conditions are good enough to have the experiment working, we conclude that the best months woudl correspond to those of Spring and eraly Summer.
3. Millimetric ground-based observations of CMB anisotropy must be performed in several bands in adequate atmospheric windows ensuring a high degree of correlation due to atmospheric noise. This correlation caused by atmospheric emission will eventually help to perform atmospheric subtraction. The choice of frequencies at which to observe is a critical point and has been studied in some detail by [87]. In this work we have provided with a simple and efficient atmospheric subtraction technique.

8.2 Future Work

The work presented in this thesis will be continued and improved in the following directions:

1. An urgent work to undertake concerns the analysis of the data collected with an improved version of the experiment during the Spring of 1996. The data have already undergone most stages of data analysis. In this campaign the beam of the instrument was reduced and a new observing strategy was applied. This new strategy aims to construct maps rather than 1D scans by observing towards the zenith and chopping in elevation. Aditionally, during this campaign we also observed the same region of the sky as during 1994 (data in this thesis). An important goal is to combine the data collected in 1994 with the new data in 1996 in an attempt to improve the situation discussed in conclusion (2) in previous section.
2. At present the interferometer at 33 GHz observing from Observatorio del Teide has completed scans at declinations 41° and adjacent with a beam size comparable to ours. In the next

future a comparison between our data adn the interferometer data will be done to search for common structures. A combined analysis of the data from all CMB experiments working from Tenerife would also be very interesting given the broad frequency range tested: 10 to 240 GHz and the wide ℓ-range sampled (from 10 to 200) on the angular power spectrum of CMB fluctuations.

3. Another goal for the next future is the improvement of the statistical analysis done on the data. We feel it is time to move from the GACF likelihood analysis to analysis based on Legendre decomposition of the auto-correlation function. An important argument in favor of this move is that [110] has found a way to characterize atmospheric noise and expand in a Legendre series. This will allow for a likelihood analysis where the presence of atmospheric remnants is treated more realistically than assuming a GACF for it. Then, an analysis to compare the observational situation with the theoretical predictions will be carried out including our measurements at $\ell = 53$.

4. Very recently our group has started collecting data with a first version of a new instrument operating from Tenerife. This is the so-called "Cosmosomas" project which attempts to map the microwave sky at 10, 15 and 30 GHz using a technique derived from the zenith observations of 1996 campaign. The beam size at present is chosen to be $\sim 1^\circ$ FWHM, and given the measurement technique a wide variety of window functions are attainable allowing a mapping of the CMB angular power spectrum up to $\ell \sim 200$.

5. All these projects will be superseded by the the "Very Small Array" project. This experiment is expected to start collecting data from Tenerife in a couple of years time. The high rejection to atmospheric noise already proved with the 33 GHz interferometric experiment and the much bigger ℓ-range sampled by the VSA give good reasons to expect this project will be one of the leading CMB experiments in the next future.

Appendix A

Gaussian Auto-Correlation Function

Until the introduction of the Flat Band Power Estimate, the Gaussian Auto-Correlation Function (GAFC) model was probably the most popular among experimentalists to analyze their data. This model is described in detail in [73, 104] and consists in assuming that the intrinsic correlation function of the fluctuations on the sky depends only on anglular distances on the sky according to:

$$C(\theta) \equiv \left\langle \frac{\Delta T}{T}(\alpha,\delta)\frac{\Delta T}{T}(\alpha',\delta')\right\rangle = C_0 \ \exp\left(-\frac{\theta^2}{2\,\theta_c^2}\right) \tag{37}$$

where the parameters describing the auto-correlation function are:

- the *coherence angle* θ_c, identified with the angular scale fluctuations on the sky.
- the intrinsic variance on the sky C_0

Equation (37) must be modified according to the beam size and measurement technique. The former involves convolving the intrinsic auto-correlation fuction with the function describing the beam, usually a beam of width σ as described by: $B(\theta,\sigma) \propto \exp[-\theta/(2\sigma^2)]$. In our case the situation is more complicated as our experiment requires of elliptical Gaussians in order to fit the actual response function (see chapter 2, 2.2.1):

$$\begin{aligned} M_{1F}(\alpha',\delta';\alpha_0,\delta_0) &= B_{\sigma_\alpha\sigma_\delta}\left((\alpha,\delta),(\alpha_0+\frac{\beta}{\cos\delta_0},\delta_0)\right) - B_{\sigma_\alpha\sigma_\delta}\left((\alpha,\delta),(\alpha_0-\frac{\beta}{\cos\delta_0},\delta_0)\right) \\ M_{2F}(\alpha',\delta';\alpha_0,\delta_0) &= B_{\sigma_c\sigma_\delta}\left((\alpha,\delta),(\alpha_0,\delta_0)\right) - \\ &\quad \frac{1}{2}\left[B_{\sigma_l\sigma_\delta}\left((\alpha,\delta),(\alpha_0+\frac{\beta}{\cos\delta_0},\delta_0)\right) + B_{\sigma_l\sigma_\delta}\left((\alpha,\delta),(\alpha_0-\frac{\beta}{\cos\delta_0},\delta_0)\right)\right] \end{aligned}$$

where the definitions of all above quantities are given in chapter 2 and we have assumed the flat approximation (i.e working over small angles) so it is possible to write:

- $B_{\sigma_\alpha\sigma_\delta}\,((\alpha,\delta),(\alpha_0,\delta_0)) = \frac{\aleph}{2\,\pi\,\sigma_\alpha\,\sigma_\delta}\exp\left[-\frac{1}{2}\left(\frac{\Delta_\alpha^2}{\sigma_\alpha^2}+\frac{\Delta_\delta^2}{\sigma_\delta^2}\right)\right]$ represents a Gaussian beam modified by the factor $\aleph$ to obtain the proper normalization.
- $\cos\Delta_\alpha = \cos^2\delta\,\cos(\alpha-\alpha_0) + \sin^2\delta$
- $\Delta_\delta = |\delta' - \delta_0|$

and the best fit values for the widths, chopping angles and normalization factors to reproduce the actual mapping functions are given in chapter 2, section 2.2.1.

The utility of fitting the mapping functions in terms of linear combinations of Gaussians is that it is straightforward to obtain the auto-correlation function of the data in terms of the intrinsic GACF of the CMB fluctuations on the sky. To do so we make use of the correlation theorem and the symmetry of the beams along each of the RA- and Dec-axis:

$$FAC_{1F}(\theta) = 2C_M(\theta;\sigma_\alpha,\sigma_\delta) - C_M(\theta - 2\frac{\beta}{\cos\delta_0};\sigma_\alpha,\sigma_\delta) + C_M(\theta - 2\frac{\beta}{\cos\delta_0};\sigma_\alpha,\sigma_\delta) \quad (38)$$

$$\begin{aligned} FAC_{2F}(\theta) &= C_M(\theta;\sigma_c,\sigma_\delta) + \frac{1}{2}C_M(\theta;\sigma_l,\sigma_\delta) - C_M(\theta + \frac{\beta}{\cos\delta_0};\sigma_c,\sigma_l,\sigma_\delta) - \\ &\quad C_M(\theta - \frac{\beta}{\cos\delta_0};\sigma_c,\sigma_l,\sigma_\delta) + \\ &\quad \frac{1}{4}[C_M(\theta + 2\frac{\beta}{\cos\delta_0};\sigma_l,\sigma_\delta) + C_M(\theta - 2\frac{\beta}{\cos\delta_0};\sigma_l,\sigma_\delta)] \quad (39) \end{aligned}$$

where: $C_M(\theta;\sigma_i,\sigma_j,\sigma_\delta) = \aleph^2\,C_0\,\theta_c^2/\sqrt{(\theta_c^2+\sigma_i^2+\sigma_j^2)\,(\theta_c^2+2\sigma_\delta^2)}\,\exp[-\theta^2/(2\,(\theta_c^2+\sigma_i^2+\sigma_j^2))]$ is the result of convolving the intrinsic GACF with an elliptical Gaussian.

The analysis in terms of GACF was developed previous to the use of the window functions to characterize experiments. The assumption of GACF has no theoretical justification and is a poor approximation to the theoretically prefered CDM angular power spectrum. Even so, as noticed in the literature (see e.g. [128, 90, 146]) there is a straightforward conversion from GACF results to those obtained assuming a flat angular spectrum (i.e $\ell(\ell+1)C_\ell$ = constant) to determine its amplitude. This is not surprising for when we vary the value of θ_c what we are actually doing is matching the power spectrum to the window function of the experiment [146].

In summary, there is a straightforward conversion from GACF results into the more portable flat band power spectrum notation which we skecth below:

1. Compute the value of ℓ corresponding to the angle θ_c of maximum sensitivity in a GACF analysis:
$$\ell_c = \frac{1}{2\sin(\theta_c/2)}$$

2. Using the values for the window function W_ℓ compute the quantities n and D defined as:
$$\begin{aligned} N &\equiv \sum_\ell \frac{\ell+1/2}{\ell(\ell+1)} \left(\frac{\ell+1/2}{\ell_c+1/2}\right)^2 \exp\left[-\frac{1}{2}\left(\frac{\ell+1/2}{\ell_c+1/2}\right)\right] W_\ell \\ D &\equiv \sum_\ell \frac{\ell+1/2}{\ell(\ell+1)} W_\ell \end{aligned}$$

3. Then the GACF result $C_0^{1/2}$ is related to the flat band power result $\sqrt{\bar{\ell}(\bar{\ell}+1)C_{\bar{\ell}}/(2\pi)}$ according to:
$$\sqrt{\frac{\bar{\ell}(\bar{\ell}+1)C_{\bar{\ell}}}{2\pi}} = C_0^{1/2}\sqrt{\frac{N}{D}} \tag{40}$$

   where $\bar{\ell}$ is the mean value of ℓ's probed by the experiment as given by:
$$\bar{\ell} = \frac{\sum_\ell \frac{\ell+1/2}{\ell+1} W_\ell}{\sum_\ell \frac{\ell+1/2}{\ell(\ell+1)} W_\ell}$$

Appendix B

Fits to the Obseved Moon Transit

The Moon is modeled as uniform disk with brightness temperature T_M and radius r. Making use of the flat approximation and placing the center of coordinates at the Moon center, our simulation assigns a response T_i to the Moon transit at demodulation nF and at time t_i given by:

$$
\begin{aligned}
T_i &= \frac{T_M N_n}{\sqrt{2}\pi\sigma^2 T} \int_{-T/2}^{T/2}\int_{-r}^{r}\int_{-\sqrt{r^2-x^2}}^{\sqrt{r^2-x^2}} dt\,dx\,dy\,\cos(n\omega t)\,\exp\left[-\frac{(x-x_i-o_{az}-\alpha\sin(\omega t))^2}{2\sigma^2}\right]\times \\
&\quad \exp\left[-\frac{(y-y_i-o_{el}-\beta\sin(\omega t))^2}{2\sigma^2}\right] \\
&= A\int_{-T/2}^{T/2}\int_{-r}^{r} dt\,dx\,\cos(n\omega t)\,\exp\left[-\frac{(x-x_i-o_{az}-\alpha\sin(\omega t))^2}{2\sigma^2}\right]\{\mathrm{erf}(b_+)+\mathrm{erf}(b_-)\}
\end{aligned}
$$

where:

- x_i and y_i are the azimuth and elevation of the antenna at time t_i in a horizontal system of coordinates where the Moon center is at the origin.
- T and ω are the wobbling period and wobbling angular frequency respectively (i.e. $\omega = 2\pi/T$)
- erf stands for the error function: $\mathrm{erf}(x) = 2/\sqrt{\pi}\int_0^x dt\,\exp(-t^2)$
- $b_\pm = [\sqrt{r^2-x^2} \pm (y_i + \beta\sin(\omega t))]$
- N_n is the normalization constant for the window function of harmonic n as discussed in chapter 2 and $A = T_M N_n/\{2\sqrt{\pi}\sigma T\}$

- And the parameters of the fit are the Moon brightness temperature (T_M), the beam width (σ), the offset in elevation and azimuth (o_{el} and o_{az}), the amplitude of the wobbling movement in azimuth (α) and the amplitude of a possible wobbling movement in elevation (β) as discussed in chapter 3 (Section 3).

The function to be fitted to the data is clearly nonlinear. To overcome this problem we have used a Levenberg-Marquardt nonlinear least squares method ([13],[102]). In order to do this, we also need to evaluate the expressions for the partial derivatives with respect to each of the parameters to be fitted:

$$
\begin{aligned}
\frac{\partial T_i}{\partial o_{az}} &= A \int\!\!\int dt dx \, \cos(n\omega t) \, \exp\left[-\frac{(x - x_i - o_{az} - \alpha \sin(\omega t))^2}{2\sigma^2}\right] \frac{(x - x_i - o_{az} - \alpha \sin(\omega t))}{\sigma^2} \times \\
&\quad \{\mathrm{erf}(b_+) + \mathrm{erf}(b_-)\} \\
\frac{\partial T_i}{\partial \sigma} &= -\frac{2A}{\sqrt{\pi}\sigma} \int\!\!\int dt dx \, \cos(n\omega t) \, \exp\left[-\frac{(x - x_i - o_{az} - \alpha \sin(\omega t))^2}{2\sigma^2}\right] \{b_+ \exp(-b_+^2) + b_- \exp(-b_-^2)\} \\
&\quad -\frac{T_i}{\sigma} + A \int\!\!\int dt dx \, \cos(n\omega t) \, exp\left[-\frac{(x - x_i - o_{az} - \alpha \sin(\omega t))^2}{2\sigma^2}\right] \{\mathrm{erf}(b_+) + \mathrm{erf}(b_-)\} \times \\
&\quad \frac{(x - x_i - o_{az} - \alpha \sin(\omega t))^2}{\sigma^3} \\
\frac{\partial T_i}{\partial \alpha} &= A \int\!\!\int dt \, dx \, \cos(n\omega t) \, \exp\left[-\frac{(x - x_i - o_{az} - \alpha \sin(\omega t))^2}{2\sigma^2}\right] \{\mathrm{erf}(b_+) + \mathrm{erf}(b_-)\} \times \\
&\quad \frac{(x - x_i - o_{az} - \alpha \sin(\omega t)) \sin(\omega t)}{\sigma^2} \\
\frac{\partial T_i}{\partial T_M} &= \frac{T_i}{T_M} \\
\frac{\partial T_i}{\partial \beta} &= \sqrt{\frac{2}{\pi}} \frac{A}{\sigma} \int\!\!\int dt dx \, \cos(n\omega t) \sin(\omega t) \, \exp\left[-\frac{(x - x_i - o_{az} - \alpha \sin(\omega t))^2}{2\sigma^2}\right] \{\exp(-b_+^2) - \exp(-b_-^2)\}
\end{aligned}
$$

Bibliography

[1] Abbott, L.F., Schaefer, R.K., 1986, ApJ, 308, 546

[2] Andreani P., *et al.* , 1991, A. & A., 249, 299

[3] Anile, A.M., Motta, S., 1976, ApJ, 207, 685

[4] Banday, A.,J. & Wolfendale,A.,W., 1990, MNRAS , 245, 182

[5] Banday, A.,J. & Wolfendale,A.,W., 1991, MNRAS, 248, 705

[6] Banday, A.,J. & Wolfendale,A.,W., 1991, ApJ, 375, 432

[7] Barkat, M., 1991, Signal: Detection & Estimation (London: Artech House)

[8] Bennett, C. L., *et al.* 1992, ApJ, 391, 466

[9] Bennett, C. L., *et al.* 1992, ApJ, 396, L7

[10] Bennett, C.L. *et al.* , 1996, ApJ, 464, L1

[11] Bensadoun *et al.* 1993, ApJ, 409, 1

[12] Bernaselli *et al.* , 1993, Enviado a ApJ

[13] Bevington, P. D., 1992, Data Reduction and Error Analysis for the Physicial Sciences, 2nd Edition, (New York: McGraw-Hill)

[14] Bond, J.R. & Efstathiou, G., 1987, MNRAS, 226, 655

[15] Birkinshaw, M.,in Proceedings of the Present and Future of the Cosmic Microwave Background, eds. J.L. Sanz, E. Martínez-González, L. Cayón; Springer-Verlag.

[16] Boulanger, F., Abergel, A., Bernard, J.-P., Burton, W.B., Désert, F.-X., Hartmann, D., Lagache, G., & Puget, J.-L., 1996, A&A, 312, 256

[17] Brandt, W. N., et al, 1994, ApJ, 424, 1

[18] Bunn, E.F. 1995, Ph.D. Dissertation, U.C Berkeley Physics Department.

[19] Cayón Trueba, L., 1993, PhD thesis, Univ. de Cantabria

[20] Cayón, L., MArtínez-González, E., Sanz, J.L., 1993, ApJ, 403, 471

[21] Church, S.E., *et al.* 1997, ApJ, 484, 523

[22] Condon,J.J, Broderick,J.J & Seielstad,G.A. 1989, AJ, 97, 1064

[23] Copi, C.J., Schramm, D.N. & Turner, M.S., 1995, ApJL, 455, L95

[24] Corey, B. & Wilkinson, D., 1976, Bull. Am. Astron. Soc., 8, 351

[25] Crane, P., Hegyi, D.J., MAndolesi, N. & Danks, A.C., 1986, ApJ, 309, 822

[26] Crane, P., Hegyi, D.J., Kutner M.L. & Mandolesi, N., 1989, ApJ, 346, 136

[27] Cernicharo, J., 1985, IRAM Internal Report,52

[28] Davies, R.D., Watson, R.A. & Gutiérrez, C.M., 1996, MNRAS, 278, 925

[29] Davies, R.D., Gutiérrez, C.M., Hopkins, J., Melhuish, S.J., Watson, R.A., Hoyland, R.J., Rebolo, R., Lasenby & Hancock, S.,1996, MNRAS, 278, 883

[30] de Amici et al, 1991, ApJ, 381, 341

[31] de Bernardis,P., Masi, S. & Vittorio, N. , 1991, ApJ, 382, 515

[32] de Bernardis,P. *et al.* , 1994, ApJL, L33

[33] de Oliveira-Costa, A., *et al.* , 1997, ApJ, 465: 288

[34] Draine, B.T. & Lazarian, A., 1997, astro-ph/9710152, ApJ in press.

[35] Eadie, W.T., Drijard, D., James, F.E., Roos, M. & Sadoulet, B., 1971, Statistical Methods in Experimental Physics (Amsterdam: North-Holland Publishing Company)

[36] Efstathiou, G., Bond, J.R., 1986, MNRAS, 218,103

[37] Femenía,B., Rebolo, R., Gutiérrez, C.M., Limon, M. & Piccirillo, L., 1998, to appear in issue 498 of ApJ.

[38] Fischer, M. L., Clapp, A., Devlin, M., Gundersen, J.O., Lange, A.E., Lubin, P.M., Meinhold, P.R., Richards, P.L. & Smoot, G.F., 1995, ApJ, 226

[39] Fixsen et al, 1994, ApJ, 420, 445

[40] Fixsen et al, 1996, ApJ, 473, 576

[41] Fixsen et al, 1997, ApJ, 486, 623

[42] Franceschini, A., Toffolatti, L., Danese, L., & De Zotti, G. 1989, ApJ, 344, 35

[43] Ganga, K., Cheng, E., Meyer, S., & Page, L., 1993, ApJ, 410, L57

[44] Ganga, K., Page, L., Cheng, E. & Meyer, S., 1994, ApJL, 423, L15

[45] Ganaga, K. *et al.* , 1997, ApJ, 484, 517

[46] Gautier, T. N., Boulanger, F., Perault, M. & Puget, J. L., 1992, AJ, 102, 1313

[47] Goicoechea, L.J., Mediavilla, E., Oscoz, A., Serra-Ricart, M. & Buitrago, J., 1998, astro-ph/9801315

[48] Gundersen, J. O., *et al.* 1995, ApJL, 443, L57

[49] Gush *et al.* , 1990, Phys. Rev. Lett., 65, 537

[50] Gutiérrez, C. M., Hancock, S., Davies, R. D., Rebolo, R., Watson, R. A., Hoyland, R. J., Lasenby, A. N., & Jones, A. W., 1997, ApJL, 480, 83

[51] Gutiérrez, C. M., 1997, ApJ, 483, 51

[52] Gutiérrez, C. M., 1997, private communication.

[53] Hagfors, T., 1970, Radio Science, 5, 189

[54] Hancock, S., *et al.* , 1994, Nature, 367, 333

[55] Hancock, S., *et al.* , 1997, MNRAS, 289, 505

[56] Hancock, S., *et al.* , 1998, MNRAS, in press.

[57] Haslam, C. G. T., *et al.* 1982, A&AS,47,1

[58] Hogan, C.J., 1984, ApJL, 284, L1

[59] Horizons On-line Ephemeris System v2.50, http://ssd.jpl.nasa.gov

[60] Hu, W. 1995, Ph.D. Dissertation, U.C Berkeley Physics Department.

[61] Jones, J.T.B. & Wyse, R.F.G., 1985, Astr. Astrophys., 149, 144

[62] Jungman, G. *et al.* , 1996, Phys. Rev. Lett, D54, 1332

[63] Jungman, G. *et al.* , 1996, Phys. Rev. Lett, D76, 1007

[64] Kaiser, M.E. & Wright, E.L., 1990, ApJL, 356, L1

[65] Kamionkowski, M., 1998, astro-ph/9803168

[66] Kirshner, R.P., Oemler, A., Schechter, P.L., Shectman, S.A., 1981, ApJL, 248, L57

[67] Klypin *et al.* , 1992, MNRAS, 258, 71

[68] Kogut et al, 1990, ApJ, 355, 102

[69] Kogut *et al.* , 1993, ApJ, 419, 1

[70] Kogut, A., *et al.* 1996, ApJ, 460, 1

[71] Kogut, A., *et al.* 1996, ApJ, 464, L5

[72] Kühr, H., Witzel, A., Pauliny-Toth, I.I.K. & Nauber, U., 1981, A&AS, 45, 367

[73] Lasenby, A.N., Davies, R.D., 1989 in Proceeding of Large-Scale Motions in the Universe, eds. Rubin & Cayne

[74] Lawson, K. D., *et al.* , 1987, MNRAS, 225, 307

[75] Leitch, E.M., Readhead, A.C.S., Pearson, T.J., & Myers, S.T., 1997, ApJ, 486, L23

[76] Levin *et al.* , 1992, ApJ, 396, 3

[77] Lim, M.A. *et al.* , 1996, ApJL, L69

[78] Lineweaver,C. H., Barbosa, D., Blanchard, A., Bartlett, J. G., 1997, A&A, 322, 365

[79] Lineweaver,C. H. & Barbosa, D., 1998, A&A, 329, 799

[80] Lynden-Bell, D., Faber, S. M., Bursteni, D., Davies, R.L., Dressler, A., Terlevich, R., Wegner, G., 1988, ApJ, 326, 19

[81] Martínez-González, E., Sanz, J.L., 1990, MNRAS, 247, 473

[82] Martínez-González, E., Sanz, J.L., 1994, in Proceedings of the Present and Future of the Cosmic Microwave Background, eds. J.L. Sanz, E. Martínez-González, L. Cayón (Berlin: Springer-Verlag)

[83] Masi, S. *et al.* , 1996, 463, L47

[84] Mather *et al.* , 1990, ApJL, 354, L37

[85] Mather *et al.* , 1994, ApJ, 420,439

[86] Melchiorri, B. & Melchiorri, F., 1982, Acta Cosmologica, 11:27

[87] Melchiorri, B. *et al.* , 1996, ApJ, 471, 52

[88] Meyer, D.M. & Jura, M., 1985, ApJ, 297, 119

[89] Netterfield, C. B., Jarosik, N., Page, L., Wilkinson, D. & Wollack, E. J., 1995, ApJL, 445, L69

[90] Netterfield, C. B., Devlin, M. J., Jarosik, N., Page, L. & Wollack, E. J., 1997, ApJ,474, 47

[91] Nicholas, J. M., 1996, PhD Dissertation, University of Delaware

[92] Oppenheim, A.V. & Schafer, R.W., 1975, Digital Signal Processing (Englewood Cliffs, New Jersey: Prentice Hall)

[93] Ostriker, J.P. & Vishniac, E.T., 1986, ApJL, 306, L51

[94] Padmanabhan, T., 1993, Structure Formation in the Universe, (Cambridge: Cambridge University Press)

[95] Page, L.,A., Cheng, S. & Meyer, S., S., ApJL, 355,L1

[96] Page, L. *et al.* , 1994, Appl. Opt, 33, 11

[97] Partridge, R.B., 1988, Rep. Prog. Phys., 51:647

[98] Piccirillo L., 1991, Rev. Sci. Instr., 62, 1293

[99] Piccirillo L. & Calisse P., 1993, ApJ, 411, 529

[100] Piccirillo, L., Femenía, B., Kachwala, N., Rebolo, R., Limon, M., Gutiérrez, C. M., Nicholas, J., Schaefer, R. K. & Watson, R. A., 1997, ApJ, 475, L77

[101] Platt, S. R., Kovac, J., Peterson, J.B., & Ruhl, J. E., 1997, ApJL, 475, L1

[102] Press, W. H., Teukolsky, S.A., Vetterling, W.T. & Flannery, B.A. 1992, Numerical Recipes: The Art of Scientific Computing, 2nd Edition,(Cambridge: Cambridge University Press)

[103] Reach, W. T. *et al.* , 1995, ApJ, 451, 188

[104] Readhead, A.C.S., Lawrence, C.R., Myers, S.T., Sargent, W.L.W., Hardebeck, H.E., Moffet, A.T., 1989, ApJ, 346, 566

[105] Reich, P. & Reich, W., 1986, A&AS, 63,205

[106] Reich, P. & Reich, W., 1988, A&AS, 74,7

[107] Reynolds, R. J., 1992, ApJ, 392, L35

[108] Richards, P.L., 1994, J. Appl. Phys., 76, 1

[109] Rocha,G. & Hancock, S., 1997, in Proceedings of the XXXIst Rencontre de Moriond, "Microwave Background Anisotropies", eds Bouchet, F.R., Gispert, R., Guiderdoni, B. & Tran Thanh Van, J., Editions Frontieres

[110] Romeo, G., Femenía, B., Ali, S. & Piccirillo, L., 1998, in preparation

[111] Roth, K.C., Meyer, D.M. & Hawkins, I., 1993, ApJL, 413, L67

[112] Rybicki, G. B. & Lightman, A. P., 1979, Radiative Processes in Astrophysics, (New York: Wiley)

[113] Sanz, J.L.,1992, in Observational and Physical Cosmology, II Canary Islands Winter School of Astrophysics, eds. F. Sánchez, M. Collados & R. Rebolo (Cambridge: Cambridge University Press)

[114] Scaramella, R. & Vittorio, N., 1988, ApJL, 331, L53

[115] Scaramella, R. & Vittorio, N., 1990, ApJL, 353, 372

[116] Scaramella, R. & Vittorio, N., 1991, ApJL, 375, 439

[117] Scaramella, R. & Vittorio, N., 1993, ApJL, 411, 1

[118] Seljak, U. & Zaldarriaga, M., 1996, ApJ, 469, 437

[119] Scott, D. & White, M., 1994in Proceedings of the 1994 CRWU Workshop on "CMB Anisotropies Two Years After COBE: Observations, Theory, and the Future", ed. L. Krauss (Singapore: World Scientific)

[120] Scott, P.F., Saunders, R., Pooley, G., O'Sullivan, C., Lasenby, A.N., Jones, M., Hobson, M.P., Duffett-Smith, P.J. & Baker, J., 1996, ApJL, 461, L1

[121] Silk, J., 1994, in Proceedings of the Present and Future of the Cosmic Microwave Background, eds. J.L. Sanz, E. Martínez-González, L. Cayón (Berlin: Springer-Verlag)

[122] Sironi *et al.* , 1990, ApJ, 357, 301

[123] Sironi *et al.* , 1991, ApJ, 378, 550

[124] Smoot *et al.* , 1991, ApJL, 371, L1

[125] Smoot *et al.* , 1992, ApJL, 396, L1

[126] Smoot, G.F. & Scott, D., 1996, astro-ph/9603157

[127] Smoot, G.F., 1998, astro-ph/9801121

[128] Steinhardt, P.J.,in Proceedings of the 1994 CRWU Workshop on "CMB AnisotropiesTwo Years After COBE: Observations, Theory, and the Future", ed. L. Krauss (Singapore: World Scientific)

[129] Sugiyama, N., 1994, in Proceedings of "the Present and Future of the Cosmic Microwave Background", eds. J.L. Sanz, E. Martínez-González, L. Cayón (Berlin: Springer-Verlag)

[130] Sunyaev, R.A., Zel'dovich,Ya. B., 1969 , Ap&SS, 4, 301

[131] Sunyaev, R.A., Zel'dovich,Ya. B., 1980a, ARA&A, 18, 357

[132] Sunyaev, R.A., Zel'dovich,Ya. B., 1980b, MNRAS, 190, 413

[133] Tanaka, S.T. *et al.* 1996, ApJL, 468, L81

[134] Tegmark, M., Silk, J., Blanchard, A., 1994, ApJ, 420, 484

[135] Tegmark, M. & Efstathiou, G., 1996, MNRAS, 281, 1297

[136] Tegmark, M, 1997a, http://www.sns.ias.edu/~max/cmb/experiments.html

[137] Tegmark, M, 1997b, astro-ph/9712038

[138] Tegmark, M. & Hamilton, A., 1997,astro-ph/9702019

[139] Traschen,J., Eardley, D.M., 1986, Phys. Rev., 34, 1665

[140] Tucker, G.S., Gush, H.P., Halpern, M., Shinkoda, I. & Towlson, W., 1997, ApJL, 475, L73

[141] U.S Standard Atmosphere 1976, National OCeanic and Atmospheric Administration, National Aeronautics and Space Administration, United States Air Force

[142] Vanmarcke, E., 1988, Random Fields: Analysis and Synthesis, (Cambridge, MA: The Mit Press)

[143] Vishniac, E.T., 1987, ApJ, 322, 597

[144] Wilson, M.L., 1983, ApJ, 273, 2

[145] White, M., Scott, D., Silk, J., 1994, ARA&A, 32, 319

[146] White, M. & Scott, D., 1994, in Proceedings of the 1994 CRWU Workshop on "CMB AnisotropiesTwo Years After COBE: Observations, Theory, and the Future", ed. L. Krauss (Singapore: World Scientific)

[147] White, M. & Srednicki, M., 1995, ApJ, 443, 6

[148] Wright *et al.* , 1991, ApJ, 381, 200

[149] Wright *et al.* , 1994, ApJ, 420, 450